Exploring Fast Neutron Computed Tomography for Non-Destructive Evaluation of Additive Manufactured parts

Dissertation

Presented in Partial Fulfillment of the Requirements for the Degree Doctor of Philosophy in the Graduate School of The Ohio State University

By

Ibrahim Oksuz, M.S.

Graduate Program in Nuclear Engineering

The Ohio State University

2022

Dissertation Committee:

Dr. Lei R. Cao, Advisor

Dr. Vaibhav Sinha

Dr. Richard Vasques

Dr. Nerine Cherepy

Abstract

Neutron imaging is one of the most powerful non-invasive investigation modalities that finds many applications in various fields such as nuclear industry, homeland security, battery research, and archeology. It provides information about the internal structures of an object as neutrons are absorbed and transmitted at different levels in the object in question. It is complementary to X-ray imaging due to the different interaction mechanisms of X-ray and neutrons with materials.

Neutron imaging applications can employ neutrons with different energies. Fast (MeV) neutrons have some advantages such as causing less radioactive transmutation in samples and providing deeper penetration which allows for exploring thicker and denser samples. It also provides good contrast images of objects made of a mix of hydrogenous and metallic elements.

With the advent of the CCD technology, new opportunities have become available to perform neutron radiography, which provides 2D images of objects, and tomography, which yields information about objects in 3D, more efficiently. Digital neutron radiography allows the collection and storage the information in a digital environment, which enables a better and quicker data analysis. However, performing neutron imaging requires a well-

characterized neutron source and a proper neutron imager, especially if fast neutrons are utilized as their interaction cross sections with materials are relatively smaller.

This work explores the advancement of the fast neutron radiograph and tomography. The work includes studies comprising characterizing neutron detectors for fast imaging application, characterizing a fast neutron beam facility, performing fast neutron tomography using various imaging phantoms, and investigating spatial resolution in a fast neutron imaging system.

In one study, Polyvinyl Toluene (PVT) (C_9H_{10}) based plastic scintillators with different dimensions and flours were investigated in terms of their relative light outputs and spatial resolutions. Due to high hydrogen concentration, PVT scintillators would be a suitable candidate since fast neutrons deposit higher energy as they interact mainly via elastic scattering reactions. This study resulted that thicker scintillators yield higher light output due to a higher amount of scintillation materials whereas they performed worse in spatial resolution because of more neutrons and light scattering.

Another study was related to characterizing the Ohio State University Research Reactor (OSURR)' recently built fast neutron beam facility. Models of the beamline and beam stop were created, and Monte-Carlo simulations were performed to determine the neutron energy spectrum, neutron, and gamma-ray flux, and dose rate distributions. Various thermal neutron filters were investigated, and Cadmium ratios that they provide were

experimentally determined. Gamma-ray content in the beam was obtained using Optically Stimulated Luminescence (OSL) dosimeters.

Another study investigates fast neutron computed tomography (nCT) using custom-made multi-material complex objects. Total nCT data collection time was as low as 2 hours for some objects. Various materials were resolved in 3D reconstructed images of the objects. Low-Z materials comprising the objects were revealed while being shielded behind high-Z materials.

The last study in this work is about the investigation of the possible effects on the system's spatial resolution in a fast neutron imaging system. Results showed that the thicker imaging objects deteriorate the spatial resolution due to the neutron scattering. Simulations provided that the neutron interaction kinematics in PVTs would also degrade the spatial resolution.

Dedication

This work is dedicated to my family. Although I am far, far away from them, they never stopped supporting and encouraging me in this journey.

"We live on an island surrounded by a sea of ignorance. As our island of knowledge grows, so does the shore of our ignorance."

-John Archibald Wheeler

Acknowledgments

This work would not be possible without the guidance and immense help of my advisor, Dr. Lei Cao. Throughout my Ph.D. study, he has always provided crucial and critical feedback whenever I needed.

I would like to extend my sincere thanks to The Ohio State University Research Reactor staff, Andrew Kauffman, Kevin Herminghuysen, Susan White, Matthew Van Zile, Joel Hatch, and Maria McGraw for their assistance in the experiments.

I would also thank my group mates who have always been ready to help. Special thanks to Matt Bisbee for being an excellent project mate, and to Praneeth Kandlakunta who has always been ready for answering my questions.

A special thanks to Bill Chuirazzi who helped me a lot when we were working on the same project in the first two years of my PhD.

I would like to thank Dr. Vaibhav Sinha and Dr. Richard Vasques for being on my committee. Dr. Sinha, I really enjoyed the discussions we had about the different aspects of my research.

I would also like to thank Dr. Nerine Cherepy for her unending willingness to help. Thanks to Phill Kerr, Kyle M. Champley, and Andrew Paul Townsend for their involvement and

contribution to my research projects. A special thanks to James Hall for his valuable contributions to my research.

I would like to acknowledge The Scientific and Technological Research Council of Turkey (TÜBİTAK) that supported me for the first two years of my study with the 2213-A international PhD fellowship program.

Vita

March 1985 ……..……..Born in Rize, Turkey

2001 ….……Tevfik Ileri E. M. High School

2008 …….…… B.S. Electrical Teacher, Marmara University, Istanbul, Turkey

2013 ……...…….…….…….……...B.S. Physics, Kocaeli University, Kocaeli, Turkey

2016 ……...…M.S. Nuclear Physics, Kocaeli University, Kocaeli, Turkey

2017 to present …...…….Graduate Research Assistant, The Ohio State University

Peer Reviewed Publications

1. Ibrahim Oksuz, Matt Bisbee, James Hall, Nerine Cherepy, Lei Cao, "Quantifying spatial resolution in a fast neutron radiography system", *Nuclear Instruments and Methods in Physics Research Section A: Accelerators, Spectrometers, Detectors and Associated Equipment*, Vol. 1027, pp. 166331, 2022.

2. S. Xue, C. Tan, P. Kandlakunta, I. Oksuz, V. Hlinka, L. Cao, "Methods for improving the power conversion efficiency of nuclear-voltaic batteries", *Nuclear Instruments and Methods in Physics Research Section A: Accelerators, Spectrometers, Detectors and Associated Equipment,* Vol. 927, pp. 133-139, 2019.

3. W.C. Chuirazzi, I. Oksuz, P. Kandlakunta, T.N. Massey, C.R. Brune, N.J. Cherepy, H.P. Martinez, L.R. Cao, "Evaluation of polyvinyl toluene scintillators for fast neutron imaging," *J. Radioanal. Nucl. Chem.*, Vol. 305, no. 1, pp. 543-551, 2018.

Conference Presentations

1- Demonstration of fast neutron tomography for complex objects at sub-mm resolution. The International Conference on Methods and Applications of Radioanalytical Chemistry (MARC), Session D: Neutron Imaging Technologies and Applications, April 3-8, 2022.

2- Automated Fast Neutron Computed Tomography at The Ohio State University Research Reactor. 2021 ANS Winter Meeting. Isotopes and Radiation: General-I, Nov. 30 – Dec, 3, 2021.

3- Fast Neutron Computed Tomography of Multi-Material Complex Objects. SPIE Optics + Photonics 2021. Hard X-Ray, Gamma-Ray, and Neutron Detector Physics XXIII, August 1-5, 2021.

4- Investigation of a Test Target Standard for Fast Neutron Imaging. Virtual 2020 IEEE Nuclear Science Symposium and Medical Imaging Conference. 27th Int. Symposium on Room-Temperature Semiconductor X-Ray & Gamma-Ray Detectors, October 31 – November 2020.

5- Investigation of PVT Scintillators for Fast Neutron Imaging. Experts Meeting on Fast Neutron Imaging. Munich, Germany, October 21st, 2019.

6- Evaluation of PVT Scintillators for Fast Neutron Imaging. Symposium on Radiation Measurements and Applications (SORMA XVII), The University of Michigan, Ann Arbor, Michigan, USA, 11-14 June 2017.

Fields of Study

Major Field: Nuclear Engineering

Table of Contents

List of Tables

List of Figures

Chapter 1. Introduction

Overview and Background

Neutron imaging is a non-destructive evaluation method with many applications, including: examining irradiated nuclear fuel specimens [1], stroboscopic imaging of an engine's interior while running [2], investigation of water agglomeration inside fuel cells [3], and water migration in living plants [4]. Unlike X-rays, which are electromagnetic radiation and interact with the atomic electron cloud, neutrons interact with the atomic nucleus as their net electrical charge is zero. Therefore, x-rays and neutron imaging together generally provide complementary information of an object being investigated [5].

The earliest studies of neutron imaging were performed employing a small neutron generator, a radiographic converter-film system, and a vacuum cassette by Kallmann and Khun between 1935-1944 [6] [7]. The first neutron imaging study carried out using a reactor beamline was in the early 1950s, and the high neutron flux that the reactor supplied opened a new chapter in neutron imaging, leading the way for it to become an effective non-destructive evaluation technique (NDT) [8]. Technology in all areas has rapidly advanced for the last seven decades, and the neutron imaging community has wisely benefited from these advancements and incorporated new technologies into their neutron imaging research. With the advent of the Charge Coupled Device (CCD) camera technology, digital neutron imaging was born, and performing neutron imaging has become

more efficient as well as facilitated the data analysis. The first neutron imaging study using a scintillator screen coupled to a (CCD) camera was accomplished in 1991 by McFarland et al [9].

Depending on the energy of neutrons, neutron imaging can generally be classified into four groups: cold [10], thermal [11], epithermal [12] [13], and fast [14]. Each energy range has pros and cons, and choosing one over another is dependent on the application. While cold and thermal neutrons provide images with better contrast, they cause radioactive transmutation in the object being investigated. This is due to the cross sections of neutron capture reactions in these energy regions, relatively higher at lower energies, and neutron capture reactions produce new isotopes which are generally radioactive and unstable. Fast neutrons, on the other hand, do not create as much radioactive nuclides since the elastic scattering reactions are the main energy transfer mechanism. Since neutrons are not captured in the object, isotopic composition in the object stays unchanged. Additionally, fast neutrons can penetrate deeper into thicker and dense materials since cross sections of elastic scattering reactions are comparatively smaller. However, this advantage turns into a challenge as the fast neutrons leaving the sample require a detector with sufficient interaction with the neutrons to provide good signal-to-noise with a reasonably short acquisition time.

Motivation

One of the fundamental challenges using fast neutrons in imaging applications is lack of efficient detectors for fast neutrons. In this work, polyvinyl toluene (PVT) based plastic scintillators doped with different Iridium-complex fluors and fabricated in different thicknesses were characterized in terms of light output and spatial resolution as a suitable neutron detector candidate for fast neutron imaging applications.

To be able to perform efficient fast neutron radiography and tomography, the strength of the neutron source utilized is very crucial. One of the main motivations to build a fast neutron beamline was to meet the growing demand of high flux and well-collimated fast neutron sources for fast neutron radiography and tomography applications, where higher neutron flux and a better beam collimation reduces image acquisition time and prevents image blur. However, the beamline characterization in terms of the gamma-ray and thermal neutron content, neutron energy spectrum, and beam divergence all contribute to obtaining good quality images that can be quantitatively compared with models that include the full physics of the beam interactions in the objects being imaged.

The main goal of this work is to demonstrate the capability of fast neutron computed tomography (nCT) for resolving small features in low-Z plastic (HDPE) objects shielded by dense, high-Z materials. Considering the interaction mechanism of fast neutrons with materials and the interaction strength that depends on the material, fast neutrons can provide information not readily visualized by thermal neutron or X-ray CT. For this purpose, various custom-made multi-material complex objects were utilized.

Chapter 2. Fundamentals of Neutron Radiography

2.1 Neutron

James Chadwick discovered the neutron in 1932 by studying the nuclear reaction given in equation (2.1) and investigating the resulting, at the time, unknown particle from this reaction [15]. The neutron has zero electrical charge and is one of the building blocks that, together with the proton, make up the atomic nucleus. It contains three quarks, one up and two down, and is classified as a baryonic particle [16]. Its mass is 1.0086 in atomic mass units (AMU) and ~1.6749 X 10^{-27} kg in SI units (or ~939.565 in MeV·c^2) [17]. Free neutrons have a half-life of ~10.3 minutes and decays to proton with a reaction given in equation (2.2).

$$ {}^{9}_{4}Be + {}^{4}_{2}He \rightarrow {}^{12}_{6}C + {}^{1}_{0}n \tag{2.1} $$

$$ {}^{1}_{0}n \rightarrow {}^{1}_{1}p + e^{-1} + \bar{\nu_e} \tag{2.2} $$

Since the neutron is a chargeless particle, it does not interact with matter via electromagnetic interaction. Therefore, it can easily penetrate through the electron cloud of the atom and interact directly with the nucleus without being affected by the Coulomb field created by the protons in the nucleus. Some of the possible interactions between the neutron and the atomic nucleus are summarized below,

1- Elastic scattering: Depending on the interaction angle and the mass of the nucleus, the incoming neutron transfers some or all of its energy to the nucleus, and both

move in certain directions and energies in accordance with the conservation of energy and momentum. Equation (2.3) is the elastic scattering of the neutron from the proton, which is called the recoiled particle.

$$ {}_{1}^{1}p + {}_{0}^{1}n \rightarrow {}_{0}^{1}n + {}_{1}^{1}p \tag{2.3} $$

2- Inelastic scattering: In this interaction, the incoming neutron imparts some of its energy to the nucleus, and the nucleus undergoes a transition to a high-energy excited state, and later decays to the ground state by emitting a gamma-ray. Equation (2.4) is an inelastic scattering reaction in which Carbon is left with its excited state after the interaction.

$$ {}_{6}^{12}C + {}_{0}^{1}n \rightarrow {}_{6}^{12}C^{*} + {}_{0}^{1}n \tag{2.4} $$

3- Radiative capture reaction: In this reaction, the incoming neutron is absorbed by the nucleus and the nucleus is transmuted to another isotope of the same atom. The resulting isotope can be unstable and decays into stable isotopes via gamma (γ), beta (β^- or β^+), or alpha (α) decays. As an example, Equation (2.5) is the neutron capture reaction that converts stable ^{197}Au to unstable ^{198}Au ($t_{1/2}$ = ~2.69 d).

$$ {}_{79}^{197}Au + {}_{0}^{1}n \rightarrow {}_{79}^{198}Au \tag{2.5} $$

4- Fission reaction: In this reaction, the nucleus is split into two similar-mass fragments after absorbing a neutron. These fragments (a.k.a. fission fragments) are radioactive, unstable atoms whose half-lives range from seconds to hundreds of thousands of years [18]. Equation (2.6) is the reaction in which ^{235}U undergoes fission after absorbing a neutron. X and Y are the fission fragments.

$$^{235}_{92}U + {}^{1}_{0}n \rightarrow X + Y + \sim 2.4n \ (\sim 205\ MeV) \tag{2.6}$$

5- Neutron multiplier reaction: In this reaction, a neutron is absorbed by a nucleus and more than one neutron is emitted by the compound nucleus. The resulting atom is one of the isotopes of the original atom and can be unstable. Equation (2.7) is a neutron multiplier reaction in which the incoming neutron is doubled in amount after interacting with the Beryllium-9 isotope.

$$^{9}_{4}Be + {}^{1}_{0}n \rightarrow {}^{8}_{4}Be + 2{}^{1}_{0}n \tag{2.7}$$

Amongst the aforementioned reactions, radiative capture reaction, fission reaction, and neutron multiplier reaction are classified as absorption reactions, while elastic and inelastic scattering reactions are classified as scattering reactions. All of these reactions have a probability of occurrence, and it is called microscopic cross section. The standard unit of the cross section is the barn, which is equal to 10^{-24} cm^2 and is represented by the Greek symbol sigma (σ). The microscopic cross section represents the area of the target nucleus seen by the incoming particle. The bigger the area the greater the probability of a reaction

occurring. The microscopic cross section is dependent on the energy of the incoming particle, the proton and neutron content of the interacting target nucleus, as well as the reaction type (elastic scattering, capture, etc.).

The microscopic cross section becomes the macroscopic cross section, which is shown with the capital sigma (Σ) and whose unit is cm^{-1}, when multiplied by the number density (N) of the material, and the number density depends on the material's mass density (ρ) and molar mass (M_A). Overall, the macroscopic cross section is given as equation (2.8). Here, N_A is the Avogadro's number (6.02214 X 10^{23} #·mol^{-1}).

$$\Sigma = \frac{\rho N_A}{M_A}\sigma \tag{2.8}$$

Each reaction has its own macroscopic cross section, and the total macroscopic cross section (Σ_{Total}) is calculated by summing absorption ($\Sigma_{Absorption}$) and scattering ($\Sigma_{Scattering}$) macroscopic cross sections.

Neutrons in motion possess kinetic energy based on their velocities, and this energy is typically given in units of electron-volt (eV). 1 eV is the energy that an electron gains when it is accelerated in the electrical potential of 1 volt. Neutrons are classified according to the kinetic energy they carry, from cold neutrons, neutrons with the lowest possible energy, to relativistic neutrons, neutrons with the highest possible energy. In between these energies, there are types of neutrons named thermal, epithermal, and fast. Table 1 provides the type of neutrons in terms of energy and the energy range of each type.

Table 1: Classification of the neutron in terms of energy [19]

Neutron type	Energy range
Cold	<0.005 eV
Thermal	0.005 eV to 0.5 eV
Epithermal	0.5 eV to 10 KeV
Fast	1 KeV to 20 MeV
Relativistic	>20 MeV

Relativistic neutrons can be created via spallation reactions using charged particle accelerators. In spallation reactions, charged particles, such as protons, are accelerated to the higher energies and hit onto nuclei of a high atomic number element, such as lead or tungsten [20]. The charged particles cause disintegration through inelastic reactions in the target nuclei, and various particles such as neutrons, protons, and alpha particles are emitted from the target nuclei with relatively high kinetic energy [21].

Fast neutrons can be produced via nuclear reactions, such as the fission of ^{235}U isotope. Fast neutrons emitted during fission reactions follow the Watt distribution. [22]. For fast neutrons, the scattering reaction is the main energy transfer and energy deposition mechanism. Figure 1 is a depiction of the elastic scattering reaction, showing the state before and after the collision, and the energy of recoiled nucleus in this reaction can be calculated utilizing equation (1.9).

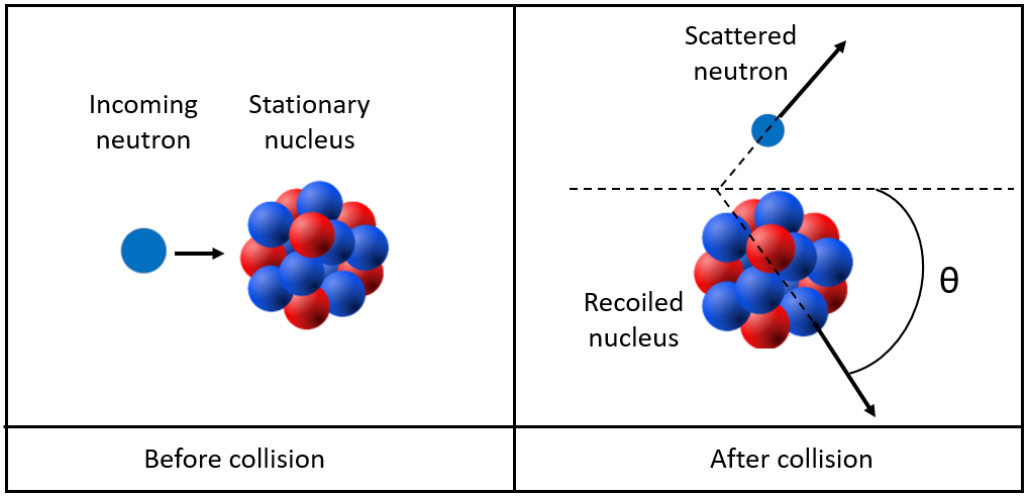

Figure 1: Elastic scattering reaction between a neutron and nucleus. Angle θ represents the recoil angle which is the angle between the directions of the motion of the incoming neutron and the recoiled nucleus.

During elastic scattering interactions, neutrons transfer their kinetic energy to the interacting nucleus depending on the mass number of the nucleus and the recoil angle. Due to the energy and momentum conservation, the amount of energy transferred from the neutron to the nucleus decreases as the number of nucleons (proton + neutron) increases. The amount of energy transferred from the neutron to the recoiled nucleus is calculated by equation 2.9.

$$E_{RN} = \frac{4A}{(1+A)^2}(Cos^2\,\theta)E_n \qquad 2.9$$

Where:

E_{RN}=Kinetic energy of recoiled nucleus

A= Mass number of target nucleus

E_n=Kinetic energy of incoming neutron

θ= Recoil angle

Hydrogenous materials, which are rich in hydrogen, such as plastics, are more effective in stopping fast neutrons via elastic scattering reactions since the masses of the neutron and proton are alike. Therefore, materials with high hydrogen concentrations are preferred for building beam dumps of fast neutron beamlines or fabricating detectors to detect fast neutrons.

Epithermal neutrons that range from 0.5 eV to 10 KeV are created by slowing down fast neutrons (down scattering) or from thermal neutrons gaining energy via elastic scattering (up scattering). Some isotopes have resonances in the epithermal energy region in which the neutron capture probability changes abruptly with energy.

Thermal neutrons are neutrons that have reached thermal equilibrium with the particles in the environment. Thermal neutrons when thought of classical particles, obey the Maxwell-Boltzmann statistics, and at room temperature, it provides the most probable energy of the thermal neutrons as 25 meV, equaling ~2200 $m \cdot s^{-1}$. [23]. The absorption cross sections of thermal neutrons are generally higher than those of fast neutrons in almost all isotopes and considerably higher for some elements such as Gadolinium (Gd) (σ_a = ~48,700 barns at 25 meV / σ_a = ~0.13 barn at 1.18 MeV). This high cross section of Gd is employed in

fabrication of Gd-based efficient thermal neutron scintillators for neutron imaging applications.

Cold neutrons can be obtained with further cooling of thermal neutrons using liquid hydrogen [24]. Since their energies are low, the penetration power into the material is also small, therefore, they cannot be used to investigate thick samples in neutron imaging. However, they yield better contrast in thin objects because their capture cross-sections with materials are relatively higher; for instance, the reaction cross section of a 0.00005 eV neutron being captured by Gd is ~94,000 barns.

2.2 Neutron radiography theory

Neutron radiography is a non-destructive investigation modality that is accomplished by collecting neutron information attenuated through a sample to generate a two-dimensional image representation of the sample being examined. It is complementary to the other imaging techniques, such as X-ray imaging, due to the differences between neutrons and X-rays in interactions with the matter. To perform neutron radiography, a neutron source that provides a beam of neutrons, an imaging object, and a neutron imager to collect the attenuated neutron signal are the necessary components.

In neutron radiography, images are generated based on the information on the neutron attenuation strength in the object being investigated. Neutron attenuation in an object takes place via the scattering or capture reactions. The atomic number (Z) and the isotope content in the object determine which reaction is dominant in neutron attenuation. Whether it is

through scattering or capture, the neutron attenuation in a material is characterized by the Beer-Lambert law, which is given in equation 2.10, and it allows for calculating the drop in the neutron beam intensity after passing through the material.

$$I(x) = I_0 e^{-\Sigma_{Total} * x} \quad 2.10$$

Where:

$I(x)$= Neutron beam intensity after passing through the material

I_0= Initial neutron beam intensity

Σ_{Total}= Total macroscopic cross section (cm^{-1}) ($\Sigma_{Scattering} + \Sigma_{Capture}$)

x=Material thickness (cm)

Neutrons that pass through the object without being scattered and absorbed are called the uncollided neutrons, and they create signals at the neutron detector. Neutrons that are captured by the object do not reach the detector; however, they do provide information about the object by not creating signals at the detector. Neutrons that are scattered may or may not reach the detector depending on the scattering angle and the distance between the object and the detector. Scattered neutrons that reach the detector, however, create false information about the object and degrade the image quality. Therefore, it is important to implement shielding and acquisition geometries that minimize the number of scattered neutrons reaching the scintillator in neutron imaging applications. Neutrons can also be scattered from the objects in the environment and find their way to the detector, creating

additional noise on the radiograph as they do not carry information about the object being investigated.

When an object, populated with voids within, is investigated using neutrons, neutrons will be absorbed only in the material that makes up the object, and not in the voids. Therefore, voids and features in an object can be revealed when neutron beam that has passed through the object impinges on a position-sensitive 2D detector. This is depicted in figure 2.

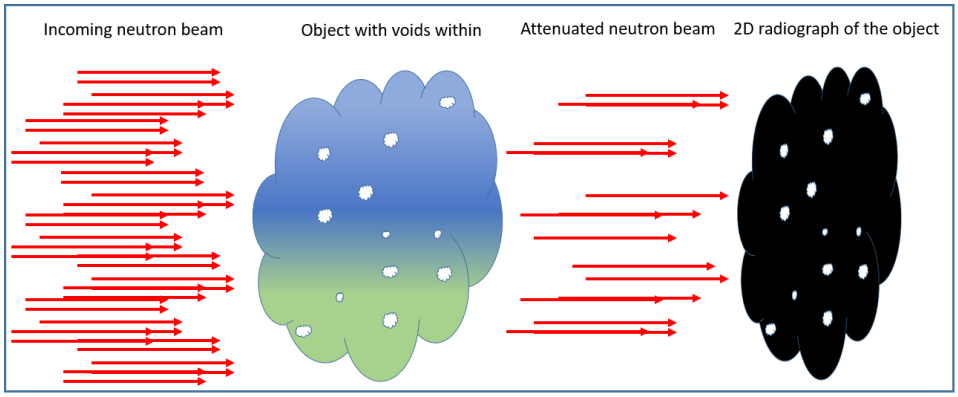

Figure 2: Depiction of neutron radiography. A neutron beam interacts with an object with internal voids (air gaps), the neutrons passing through the positions where the voids are located will not be attenuated as much as the ones passing through the locations where there are no voids. The resulting neutron beam after interacting with the object is recorded by a detector in which a 2D image of the object is constructed. The image then provides information about the internal voids.

Since the neutrons carry zero net electrical charges, they do not interact with the atomic electron cloud, unlike X-rays, but interact with the nucleus itself. Although X-rays' electrical charge is zero, they are electromagnetic waves and therefore interact with electrons via various interactions, such as the photoelectric effect and Compton scattering [25]. Because neutrons interact only with the nucleus, the interaction cross-section is dependent on the energy of the neutron, as well as the elemental atomic mass, whereas the interaction strength of X-rays with elements increases steadily with atomic number. Figure 3 provides Mass Attenuation Coefficients (MACs), the macroscopic cross section divided by the mass density of an element ($cm^2 \cdot g$), for thermal neutrons, 2 MeV neutrons, 14 MeV neutrons, 100 KeV X-rays, and 9 MeV bremsstrahlung X-rays across the periodic table. For thermal neutrons, the MAC does not follow a regular pattern. By contrast, for fast neutrons, the MAC decreases rapidly for elements with low Z numbers while decreasing slowly for elements with high Z numbers since the interaction mechanism is mainly elastic scattering. Utilizing fast neutrons facilitates imaging of hydrogenous materials, even when obscured by dense, high-Z materials. This is due to the high MAC of hydrogen, compared to elements with $Z > 20$. For X-rays, the MAC decreases with increasing energy since the photoelectric absorption is inversely proportional to the energy. For low X-ray energies (100 KeV), the MAC increases rapidly with Z number due to increased electron density.

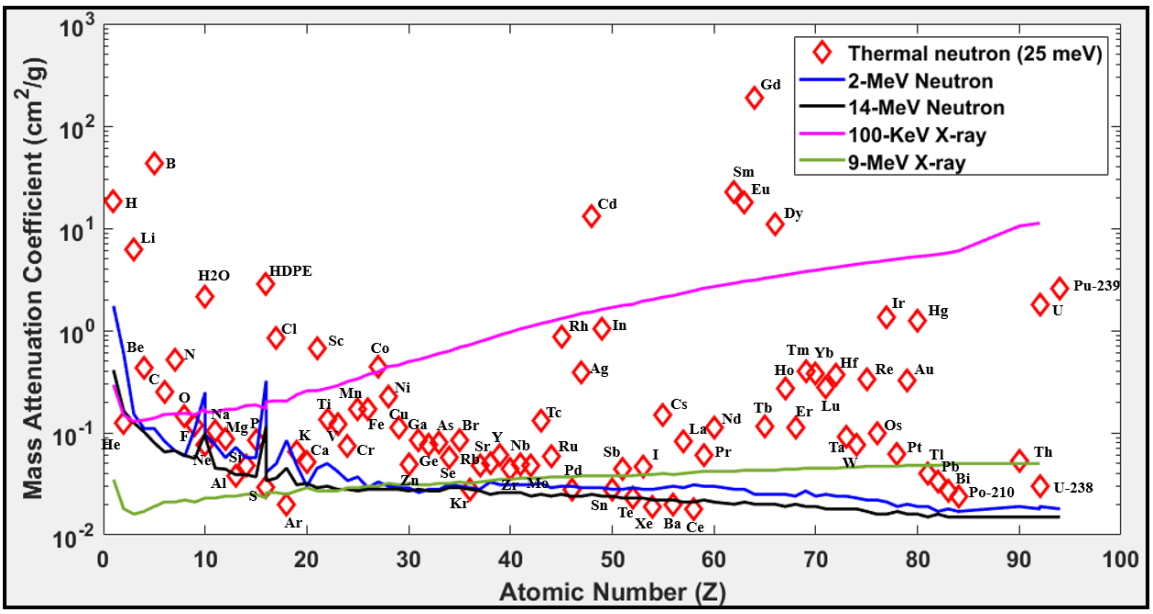

Figure 3: Mass attenuation coefficients for neutrons and bremsstrahlung X-rays across the periodic table. Two distinct peaks seen on the 2- and 14-MeV neutron curves belong to water (H_2O) and high density polyethylene (HDPE).

2.3 Neutron sources

As mentioned earlier, neutrons can be produced via nuclear reactions. A neutron source for imaging can be engineered to supply neutrons generated via one of these reactions. There are various types of neutron sources, differing in terms of levels of neutron flux and neutron energy spectrum. Flux, or fluence rate, is defined as the number of neutrons passing an area of a square centimeter per unit time, and its unit is neutron (#)·cm^2·s in the SI unit system. Performing practical direct neutron radiography requires a neutron source that supplies a fluence rate of on the order of 10^9 n·cm^{-2}·s^{-1}. [26] [27]. Neutron sources can be categorized into different groups such as nuclear reactors, charged-particle accelerators, neutron

generators, and spontaneous fission (radioisotope) sources. Selecting one source over another is generally dependent upon the application as each source has pros and cons.

2.3.1 Nuclear reactor beamlines

Research reactor beamlines supply a beam of neutrons created within the reactor core via the fission reactions. In thermal reactors which use ^{235}U as fuel, the number of neutrons on average produced per fission reaction is 2.4355 ± 0.0023, and the energy of the neutrons obeys the Watt distribution, with an average energy of ~2 MeV [28] [29]. In these reactors, water is used as both moderator and coolant, and fast fission neutrons get thermalized to lower energies. Neutrons (thermal, epithermal, and fast) in this source–water system are taken outside of the reactor to be employed for neutron imaging applications, employing a collimator system. Reactor beamlines can provide high neutron fluxes with relatively uniform and collimated beams.

2.3.2 Charged particle accelerators

Charged particles can undergo capture reactions with nuclei, and in some of these reactions, neutrons can be emitted. However, these charged particles need to be accelerated to high energies to overcome the Coulomb barrier of the nucleus. These reactions are also called threshold reactions since the reaction cross sections are zero up to certain energies of charged particles. In the accelerators such as the Tandem accelerators, charged particles are accelerated under an electric field and sent onto nuclei. The energy spectrum of the neutrons emitted as a result of the reaction is dependent on the energy of the incoming

charged particle as well as the target nucleus [30]. Be(p, n) and Be(d, n) are two of the charged particle reactions in which accelerated protons and deuterons hit beryllium nuclei and create neutrons. [31]. With a proton beam of 5 MeV, Be(p, n) produces a beam of neutrons with an average energy of 1.74 MeV and maximum energy of 3.2 MeV. [32].

Another way of producing neutrons via charged particle reactions is the spallation reaction. In the spallation process, highly energetic charged particles accelerated employing accelerators are crushed onto nuclei with high Z numbers, such as lead, tungsten, and bismuth. Neutron yield from the spallation reactions is dependent on the incoming charged particle energy, target, and where the beam of the charged particle hit on the target. [33]. With a pulsed proton beam with an energy of 800 MeV and a tungsten target, a beam of neutrons with energy ranges from ~1 MeV to 600 MeV can be created. [34].

2.3.3 Spontaneous fission sources and fusion sources

In some neutron radiography applications, such as cargo scanning, a portable neutron source is required for quick and efficient data acquisition. This necessity can be addressed by employing radioactive isotopes that emit neutrons for building a neutron source. For this purpose, Californium (Cf) can be utilized. Cf is one of the transuranic elements, and none of its isotopes is stable and they decay via various decay schemes. ^{252}Cf decays through alpha emission (97%) and spontaneous fission (3%) with a half-life of 2.645 y [35]. The spontaneous neutrons yield per fission 3.8 on average and a mean neutron energy of 2.105±0.014 MeV [36] [37].

Like spontaneous fission, fusion reactions, such as deuterium-deuterium (D-D) and deuterium-tritium (D-T), are also able to produce neutrons, and they are used to build compact neutron generators. Equations of the D-D and D-T reactions are given in equations 2.11 and 2.12, respectively.

$$ {}_{1}^{2}H + {}_{1}^{2}H \rightarrow {}_{0}^{1}n + {}_{2}^{3}He \quad Q = 3.270\ MeV \tag{2.11} $$

$$ {}_{1}^{2}H + {}_{1}^{3}H \rightarrow {}_{0}^{1}n + {}_{2}^{4}He \quad Q = 17.590\ MeV \tag{2.12} $$

Both D-D and D-T reactions provide monoenergetic neutrons of 2.45 MeV and 14.1 MeV, respectively [38]. Having a monoenergetic fast neutron beam is crucial for fast neutron beam applications.

Both spontaneous fission and fusion sources provide lower neutron fluxes compared to reactors and accelerators, therefore, data acquisition is slower than with as reactors and accelerators. Additionally, the safety of all fast neutron sources is a key consideration, since shielding fast neutrons is challenging, especially when considering spontaneous fission sources cannot be turned off.

2.4 Neutron beam geometry and beamline characteristics

Amongst the aforementioned neutron sources, reactors generate fission neutrons throughout their cores, while the spot size in which neutrons are produced in particle accelerators, neutron generators, and radioactive isotope sources are comparatively smaller

[39] [40]. Therefore, in imaging applications, accelerators and neutron generators tend to operate in “cone beam” geometry, while reactors provide parallel (or near-parallel) beam imaging.

For the case of research reactors, to be able to use neutrons for various applications including neutron imaging, the neutron beam needs to be taken outside of the core using collimator tubes which pass through the reactor biological shielding. Collimator tubes host various materials that help shape and filter the beam. Those materials include graphite, lead, borated aluminum, bismuth, and etc. While most of the materials used in collimators have an aperture, bismuth is used as a solid crystal as it is used for gamma-ray filtering. After taking the neutrons out from the reactor core, the beam needs to be characterized in terms of various aspects as the quality of neutron radiographs is highly dependent on the beam characteristics. Those characteristics include the effective collimation ratio, Cadmium ratio, neutron energy spectrum, and gamma-ray content.

2.4.1 Effective Collimation Ratio

The effective collimation ratio is also known the Length-to-Diameter (L/D) ratio. L here is the distance between the source and the detector plane, and D is the size of the source. There is a well-established no umbra (NU) technique to determine the L/D ratio of neutron radiography beams, and an ASTM standard details the procedure of using NU device to determine it [41]. The effective collimation ratio defined in the standard is not related to the physical dimension of the beamline, and it is applied to only thermal neutron beams. It is an important characteristic since it affects the quality of the neutron radiographs- the

higher the L/D ratio, the sharper the radiographs become. Lower L/D ratios provide higher neutron fluxes, however, cause higher geometric unsharpness [42]. Beam divergence, which is related to the L/D ratio, is another important factor that affects the image quality. Beam divergence arises from the neutrons entering the collimator with an angle other than 90°. Of these neutrons, some of them exit the collimator without interacting with internal surface of the collimator, while some bounce around as they are traveling through the collimator. Figure 4 is a depiction of neutrons traveling inside a collimator.

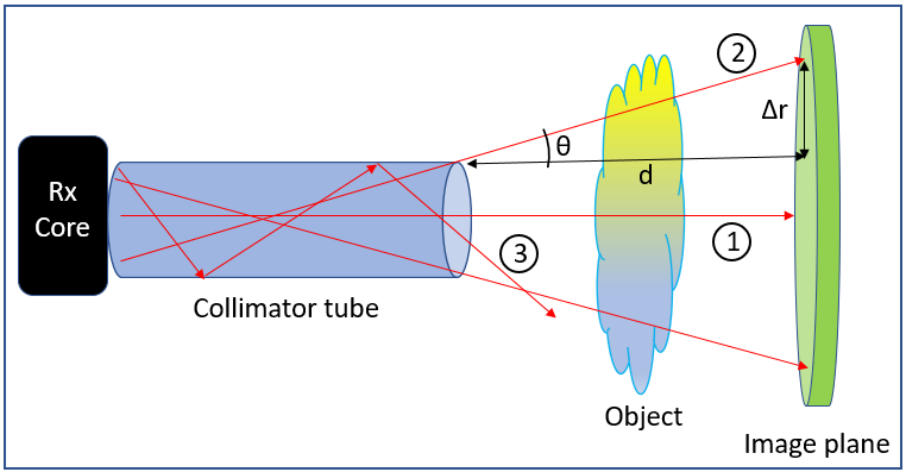

Figure 4: Neutrons traveling inside a collimator. 1- direct neutron (no interaction inside the collimator), 2- neutrons that do not interact with the collimator, but cause divergence, 3- neutrons that bounce inside the collimator and leave the collimator with even higher angle. θ is the angle of divergence. Δr is the difference in beam radius.

The beam divergence can easily be calculated using equation 2.13 when the difference in the beam radius (Δr) and the distance between the beam exit and the image plane are known.

$$\theta = \tan^{-1}\left(\frac{\Delta r}{d}\right) \quad 2.13$$

Placing an object closer to the beam exit may cause neutrons shown as #3 in figure 4 to interact with the object, which may yield lower quality images as those neutrons can hit the object with high divergence angle. On the other hand, the object should not be located too far from the beam aperture as the neutron flux decreases with distance, following $1/R^2$. Optimum distance should be determined based on the object and the system.

2.4.2 Cadmium Ratio

Cadmium (Cd) ratio provides the information about the thermal neutron content of a neutron beam. It is determined using the gold foil activation method, and an ASTM standard provides the guideline of the whole procedure [43]. The higher Cd-ratio represents a higher thermal neutron content in a neutron beam. It is very important for a neutron beam to have lower Cd-ratio if fast neutron radiography is intended to be performed- especially if the neutron detector utilized is sensitive to thermal neutrons. Therefore, thermal neutron filters are necessary components in reactor beamlines for fast neutron radiography applications. Thermal neutron filters are made of materials that have high thermal neutron absorption cross sections. Reactions provided in table 2 have relatively high thermal neutron capture cross sections and can be utilized to fabricate thermal neutron filters.

However, ^{10}B, ^{113}Cd, and ^{157}Gd emit prompt gamma-rays upon capturing thermal neutrons, which is not preferable. The filter that contains ^{6}Li needs to be thick enough to provide sufficient neutron absorption, however, this is not also desirable as it compromises the beam uniformity. Utilizing ^{3}He may also be problematic as it requires a leakage-free container. Therefore, an optimum thermal filter should be the one that provides the minimum gamma and thermal neutron contents.

Table 2: Neutron capture reactions with high cross sections.

$n + {}^{3}_{2}He \rightarrow {}^{3}_{1}H + {}^{1}_{1}H$
$n + {}^{6}_{3}Li \rightarrow {}^{4}_{2}He + {}^{3}_{1}H$
$n + {}^{10}_{5}B \rightarrow {}^{4}_{2}He + {}^{7}_{3}Li + \gamma$ (93%) $\rightarrow {}^{4}_{2}He + {}^{7}_{3}Li$ (7%)
$n + {}^{113}_{48}Cd \rightarrow {}^{114}_{48}Cd + \gamma$
$n + {}^{157}_{64}Gd \rightarrow {}^{158}_{64}Gd + \gamma$

2.4.3 Neutron Energy Spectrum

Neutron energy spectra of reactor beamlines are resembling each other regarding of having two prominent peaks in thermal and fast region, along with the flat epi-thermal region. However, slight changes may arise due to the reasons, such as materials utilized to collimate and shape the beam, the water column thickness between the reactor core and the collimator entrance, and to which point on the surface of the reactor core the collimator

faces. Determining the neutron energy spectrum requires various foils that have different absorption cross sections to different neutron energies.

2.4.4 Gamma-ray content

Reactor beamlines employ fission reactions that produce, besides neutrons, prompt and delayed gamma-rays. For most applications, especially neutron radiography, gamma-ray is the unwanted component of the beam, and thus, gamma-ray filters are utilized to minimize the gamma content. Since gamma-rays are electromagnetic radiation, high-Z materials are preferred for the filter material, such as bismuth. However, using a thicker filter may distort the neutron beam, causing it to diverge from the parallel. For neutron radiography applications, determining the gamma content in the beam is of great importance as the neutron detectors employed may be sensitive to both neutrons and gamma-rays. Gamma content in the beam can be measured quantitatively using gamma-only sensitive dosimeters.

2.5 Imaging Phantom

In neutron radiography, for a given energy range of neutrons, acquiring images with sufficient contrast is dependent on the elemental and isotopic composition of the object, as well as its geometry and size. Since the thermal neutron cross sections vary dramatically across the periodic table, images with good contrast can be obtained easily with thermal neutrons, especially for certain elements such as Li. Fast neutrons, on the other hand, are useful to investigate objects made of a mixture of high- and low-Z materials since their

main energy deposition mechanism is elastic scattering, which varies little across the periodic table. Imaging phantoms can be fabricated using conventional machining methods, such as milling. However, the adoption of additive manufacturing technology for fabrication of industrial components has introduced uncertainties in quality control (due to internal voids not visible from the exterior) that may be addressed by techniques such as X-ray and neutron computed tomography. Additive manufacturing may be used to produce phantoms with various layers and intricate features, including deliberately introduced defects. These phantoms can be tested to determine the capability of the neutron imaging system.

2.6 Components of the digital neutron radiography system

A digital neutron radiography system generally consists of a camera, a neutron detector, and a light-tight apparatus. Besides these components, if tomography, which provides volumetric images of the object investigated, is pursued, rotation and linear stages are necessary since they facilitate efficient data acquisition.

Since neutrons' net electrical charge is zero, unlike charged particles, such as electrons and protons, they cannot be detected directly. Therefore, in neutron radiograph, a converter screen, such as a scintillator, is utilized. A scintillator is a material in which scintillation light is emitted from atoms as they decay to ground states, after being excited by moving charged particles or electromagnetic radiation. Light output, scintillation decay time, and spatial resolution are among the characteristics of scintillators. There are two types of scintillators commonly used: organic and inorganic, while the former can be in crystal,

liquid, and plastic forms, and the latter is in crystal form. [44]. Amongst the many scintillators, $Gd_{0.3}Lu_{1.6}Eu_{0.1}O_3$ (GLO) [45], ^{6}LiF:ZnS(Ag) [46] , and Gd_2SiO_5 (GSO) [47] are commonly employed for thermal neutron imaging, while BC400 and PP/ZnS:Cu, [48] are preferred for fast neutron imaging. Plastic scintillators offer a high light output in fast neutron imaging applications because their high hydrogen concentrations enable maximum energy transfer from fast neutrons.

After scintillations light is produced, it is collected employing a digital camera. Nowadays, depending on the application, various digital cameras, such as CCD, EMCCD, and CMOS, are being effectively employed. Scintillation light is focused on the pixelated camera sensor using a lens, creating electrons that then fill the pixel. The readout process of the pixels converts the electrons into the gray value on the image. During the light collection, the scintillator and the camera aperture are kept in a light-tight box that allows optical isolation from the environment, to record the light coming only from the scintillator. Figure 5 is a depiction showing the general steps of creating a radiograph in a digital neutron imaging system.

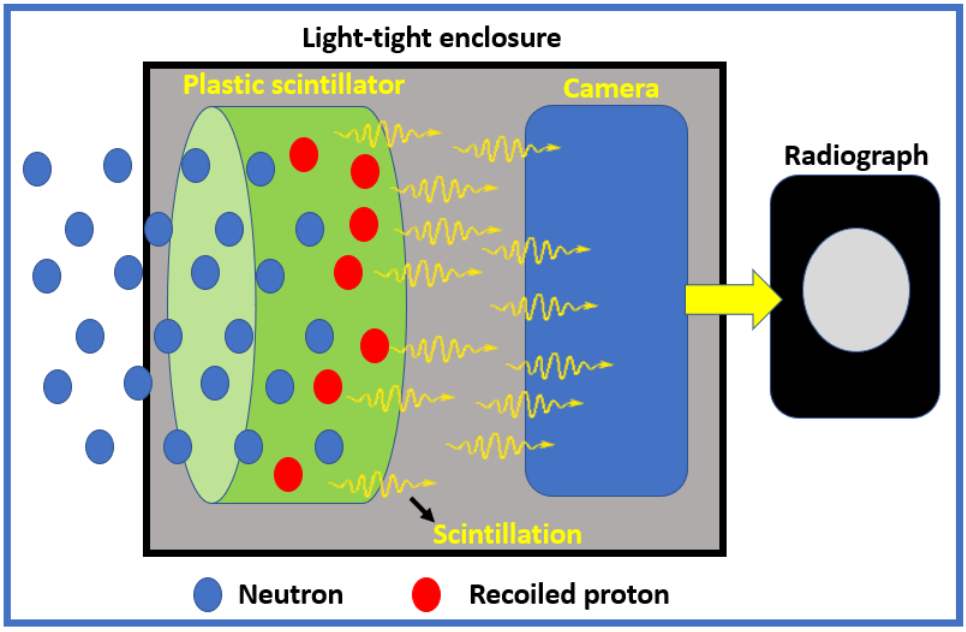

Figure 5: Depiction of the digital neutron radiography system. Fast neutrons create recoiled protons, which cause scintillation light to be emitted. The camera collects the light information and converts it to a radiograph.

2.7 Neutron computed tomography (nCT)

Neutron radiography provides two-dimensional information about an object. Neutron computed tomography (nCT) allows reconstructing of a three-dimensional image of an object by combining radiographs taken at different angles. nCT is a very powerful technique for acquiring internal information. Although CT it is mainly used in X-ray imaging in medical applications, neutrons can also be used to carry out CT using a similar procedure. Johann Radon first introduced an iterative reconstruction method, called Radon transform, in 1917 [49].

Neutron CT is accomplished by collecting projections of an object at different angles and creating reconstructed images using a reconstruction algorithm, such as Filtered Back Projection (FBP). The resulting reconstructed images later can be used to create a volume rendering of the object in question. Since a 3D rendered image contains all the information in all the projections acquired, intricate internal structures that are not seen on a single 2D radiograph can be revealed. Figure 6 depicts the general steps of nCT.

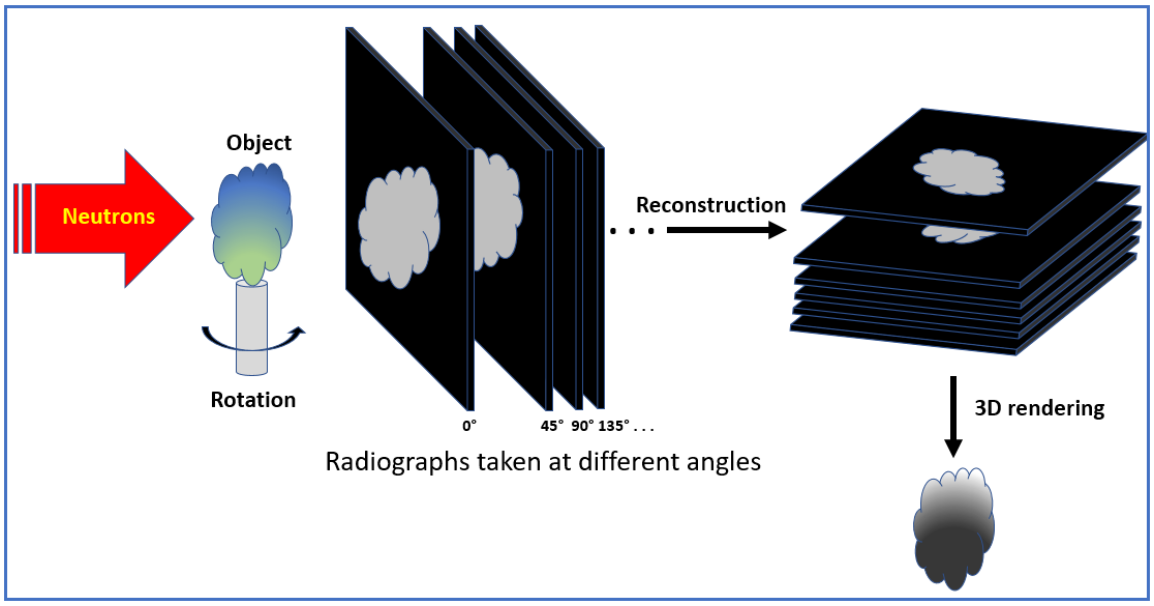

Figure 6: General steps of nCT.

Advancements in digital neutron imaging systems paved the way for neutron CT to become a more efficient and common tool for NDT applications. Today, different fields make use of neutron CT in various applications, such as examining cultural heritage artifacts [50] [51], identifying corrosion of steel in concrete [52], and water distribution in soil [53].

2.8 Image Processing and Image Quality

A radiographic image does not just contain information about the object, but also includes various types of unwanted noise, such as dark (thermal), readout, Poisson (a.k.a. shot) noise, and impulse (salt and pepper) noise, as well as the noise that is generated by neutrons and gamma-rays hitting and depositing their energies directly to the camera chip (direct hits). In order to obtain true information about the object, these noise sources need to be minimized, if not completely eliminated. While some of these types of noise are easy to deal with, some others are very difficult to remove. The readout and dark noises are inherent to the camera, and with proper cooling, dark noise can be lowered to a negligible level. The Poisson noise is related to statistical variation in the arrival rate of photons to the CCD chip, and can be reduced with longer signal averaging. The impulse noise originating from the sharp change in the image signal may be reduced by image processing with a median filter.

The quality of an image can be assessed by determining the Signal-to-Noise Ratio (SNR). SNR of an image can be calculated using equation 2.14.

$$SNR = \frac{\sqrt{MGy}}{\sigma_{MG_y}} \tag{2.14}$$

Where:

MGy : Mean gray value

σ_{MG_y} : Sample standard deviation of the mean gray value, which is given in equation 2.15

$$\sigma_{MG_y} = \sqrt{\frac{\sum(x_i - MG_y)^2}{n-1}} \quad (2.15)$$

Chapter 3. Fast Neutron Beam Facility

3.1 Facility Outline

The fast neutron beam facility at the Ohio State University Research Reactor (OSURR) consists of three main components: two beam collimators, a beam shutter, and a beam-stop. The 107 cm long first collimator, positioned closer to the reactor core, includes a 15.24 cm thick graphite cylinder with a 3.2 cm diameter aperture, followed by a 10.16 cm thick solid cylinder of polycrystalline bismuth for filtering out gamma-rays. A ~1.6 mm thick water-filled gap and a ~1.6 mm thick aluminum (Al) cap separate the reactor core structure and the collimator entrance, which minimize fast neutron thermalization before the collimator entrance. Both the first and the second collimators include disks of aluminum (Al), lead (Pb), borated aluminum, and a castable shielding material, SWX-277z-5, of different thicknesses to further increase the beam collimation. The beam shutter, stationed between the two collimators inside the reactor biological shielding wall, is a 38 cm diameter cylindrical drum with an aperture and is made from High-Density Polyethylene (HDPE) and lead (Pb) to attenuate and block neutrons and gamma-rays, respectively. The beam-shutter drum resides inside a shutter box that also contains the 40 cm long second collimator. The beam-shutter drum is controlled by a motorized mechanism for operation of opening and closing the neutron beam by rotating the drum clockwise and counterclockwise, respectively.

The neutron beam's diameter at the collimator exit is 32 mm, and the collimator ratio, L/D -where L is the distance between the collimator entrance near the core and the image plane at the beam exit, and D is the diameter of the beam- was calculated as ~62.

The beam-stop, weighing ~1.37 metric tons with dimensions of ~80 cm x ~80 cm x ~80 cm, is composed of SWX-201HD borated polyethylene sheets with a boron concentration of 5 % by weight and lead (Pb) for absorbing neutrons and gamma-rays, respectively. Additionally, borated aluminum (Metamic) and aluminum plates were included in the beam-stop assembly to further enhance the neutron absorption. Due to the limited space in the reactor bay, it is desirable to move the beam-stop against the reactor wall when the beamline is not operated. For maintenance needs and certain applications, the beam collimators need to be extracted, but the lack of adequate space prevents the beam-stop moving sufficiently away from the beam exit. In order to meet these requirements, a motorized system was designed and integrated into the beam-stop to drive the beam-stop from vertically in an up and down motion, while a rail system on which the beam-stop rests and slides enables horizontal back and forth motion. Figure 7 is a photograph of the beam-stop including the motorized drive and the rail systems.

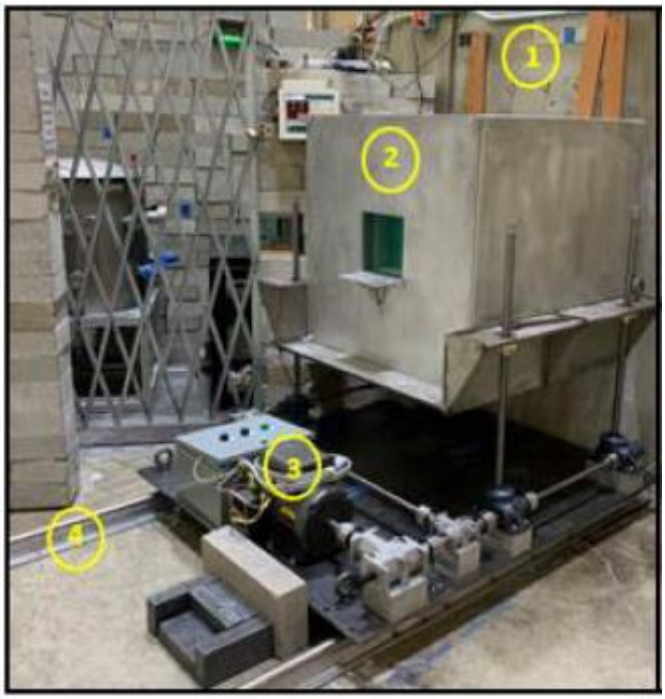

Figure 7: 1. Reactor biological shielding, 2. Beam stop, 3. Motorized system for up and down motion, 4. Rail system for back-and-forth motion.

3.2 Beamline Model

A Monte Carlo N-Particle (MCNP) model of the beamline containing the collimators, the beam shutter, and the beam-stop were developed to investigate the neutron and gamma-ray fluxes and dose rates and determine the thickness of the materials necessary to keep radiation dose rates at acceptable levels. Figure 8 shows the model of the collimators and the beam shutter. In this version of the model, the aperture in the beam-shutter drum is aligned vertically, which puts the beam in OFF condition. The MCNP input deck of this model is provided in Appendix A. Figure 9 shows the model of the beam-stop, and the MCNP input deck of this model is given in Appendix A.

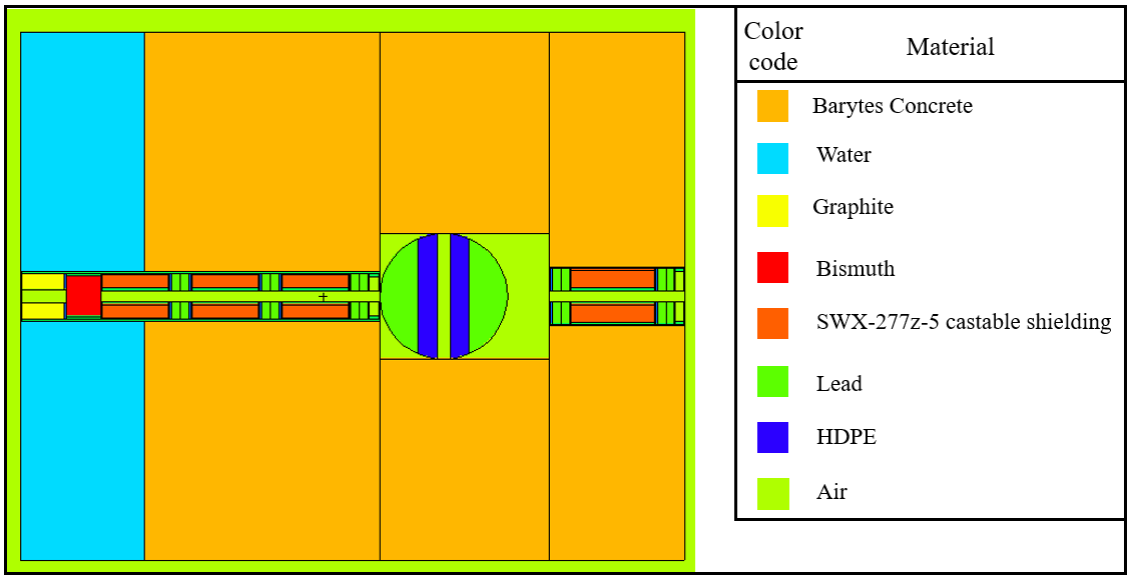

Figure 8: MCNP model of the fast neutron beamline with the beam in OFF condition. The beam coming from the reactor core travels from left to right.

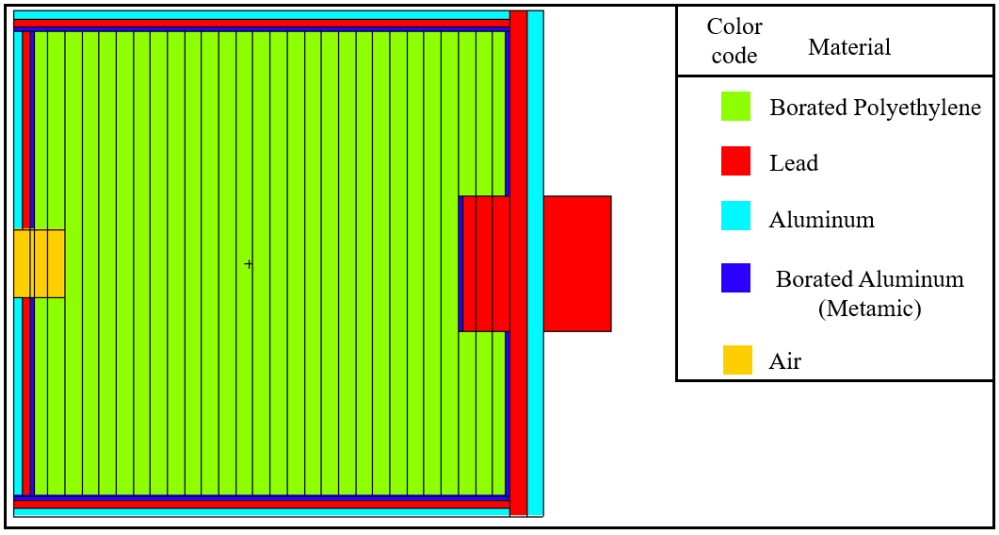

Figure 9: MCNP model of the beam stop. The beam coming from the beam exit travels from left to right.

3.3 Neutron Energy Spectrum

The neutron energy spectrum defines one of the most important performance characteristics of a neutron beam facility. The neutron energy spectra both at the beam entrance (near core) and exit (experiment area) locations were simulated using MCNP code with a combined OSURR full-core and neutron collimator model. Figure 10 shows simulated neutron energy spectra of near-core and near imaging locations.

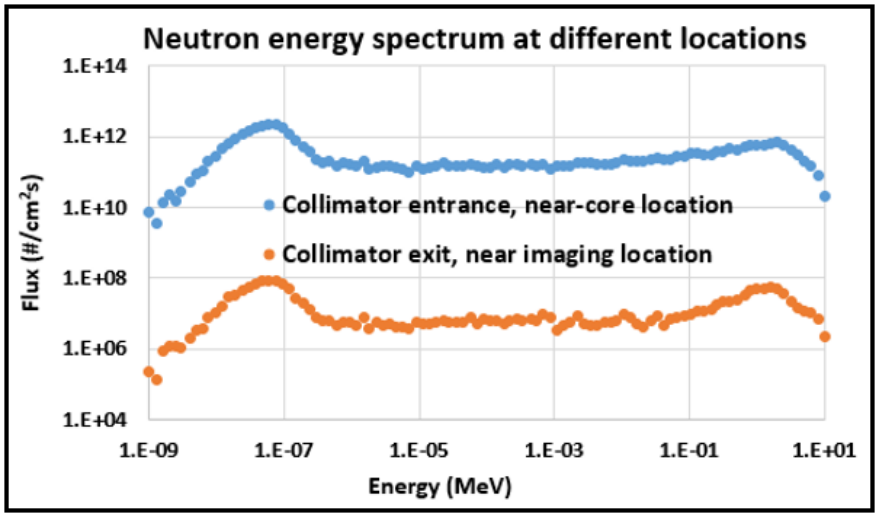

Figure 10: Neutron energy spectra at the collimator entrance and exit locations of the beamline simulated using MCNP

Simulations results indicate a four orders of magnitude reduction in the neutron flux at the collimator exit in comparison with that at the collimator entrance. For example, the neutron flux at the collimator exit is ~ 5.4 x 10^7 n·cm^{-2}·s^{-1} at the 1.6 MeV median neutron energy. Results also show that, in comparison with the flux at the collimator entrance, the reduction

in the thermal neutron (25 meV) flux is higher than that in the fast neutron (1.6 MeV) flux at the collimator exit. The reason for this outcome can be attributed to polycrystalline bismuth that has a higher absorption cross-section for thermal neutrons (9.36 barns at 25 meV) compared to fast neutrons (5.33 barns at 1.6 MeV).

3.4 Thermal Neutron Content in the Beam

To perform the experiments requiring mainly fast neutrons, such as fast neutron imaging, thermal neutrons need to be filtered out in the beam. Therefore, three thermal neutron filters were investigated in terms of thermal neutron removal capability: 3 mm and 2.54 cm thick lithiated (Li) glasses, and 2 mm thick cadmium (Cd) foil. Photos of the 2.54 cm Li glass and 2 mm Cd foil are given in figure 11. The 3 mm Li glass was provided by National Institute of Standard and Technology (NIST), and its composition was $^{6}Li_2O$ (37 mol %) (Enriched with 6Li between 90-95%) SiO_2 (59 mol %) Al_2O_3 (4 mol %) [54]. Notwithstanding, the composition of the 2.54 cm Li glass was unknown, and it contained natural lithium.

Natural lithium has two stable isotopes: ^{6}Li and ^{7}Li having natural abundances of 7.59 % and 92.41 %, respectively. ^{6}Li has a relatively high thermal neutron capture cross-section of ~940 barns, and upon capturing a thermal neutron, it disintegrates into ^{4}He and ^{3}H. The cross-section of the same reaction for natural lithium is ~70.5 barns, and natural lithium produces prompt gamma-rays with negligibly small emission probabilities upon capturing thermal neutrons. This is an important feature of a thermal neutron filter considering scintillators, employed in neutron imaging applications, may be sensitive to gamma-rays.

Cadmium has eight stable isotopes with differing natural abundances. Amongst the isotopes, ^{113}Cd, whose abundance is 12.22 %, has the highest radiative thermal neutron capture cross-section of ~20,000 barns, and as the result of the capture reaction, it is transmuted into ^{114}Cd and releases prompt gamma-rays ranging from ~0.1 MeV to ~9 MeV [55] [56]. The Cd foil tested in this study is natural cadmium with a purity of 99.998%. The radiative thermal neutron capture cross-section of natural cadmium is ~2460 barns, and calculations showed that 2 mm thick natural cadmium absorbs ~99.998 % of thermal neutrons.

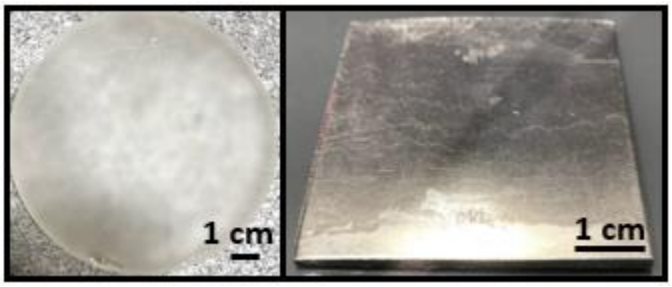

Figure 11: Thermal neutron filters. 2.54 cm thick Li glass (Left) and 2 mm thick Cd foil (Right).

To explore the effectiveness of these filters in terms of removing thermal neutrons in the beam, Gold (Au) foil activation method was utilized, and Cadmium (Cd) ratio was calculated.

The importance of the Cd-ratio comes from the drastic decrease in cross-section at around 0.4 eV in ^{113}Cd (n, g) ^{114}Cd capture reaction. With this feature of ^{113}Cd isotope, thermal neutrons are removed in the beam, while the rest of the spectrum remains relatively

unaffected. Figure 12 gives the neutron capture cross-section of ^{113}Cd, along with the neutron energy spectrum at the beam exit, while the neutron energy at the horizontal axis is being the same for both. The shaded rectangular region highlights the Cadmium cut-off as well as the thermal neutron peak that would be removed due to the high neutron capture cross-section of ^{113}Cd.

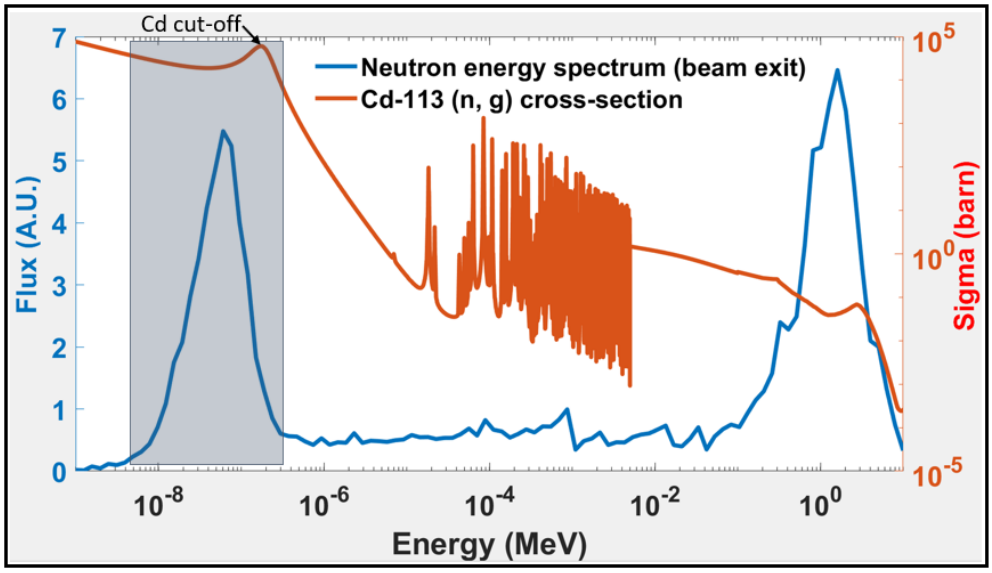

Figure 12: The cross-section of ^{113}Cd neutron capture reaction and the neutron energy spectrum at the beam exit. The shaded area shows the energy interval that would be affected the most in the spectrum due to the high cross-section in ^{113}Cd.

In the gold foil activation measurement, two gold foils with known masses, one is bare while the other was placed inside a ~1 mm thick button-shaped cadmium cover, were irradiated in the beam for a certain time. During irradiation, unstable ^{198}Au isotopes, whose

half-life is ~2.7 days, were created via the neutron capture reaction ^{197}Au (n, γ) ^{198}Au (σ_c=~98 barns at 25 meV). A depiction of the experimental setup of the gold foil activation measurement is given in figure 13, and figure 14 shows photographs of the bare and Cd-covered gold foil irradiation setups as well as Au foil placed in the counting position in the High Purity Germanium (HPGe) detector.

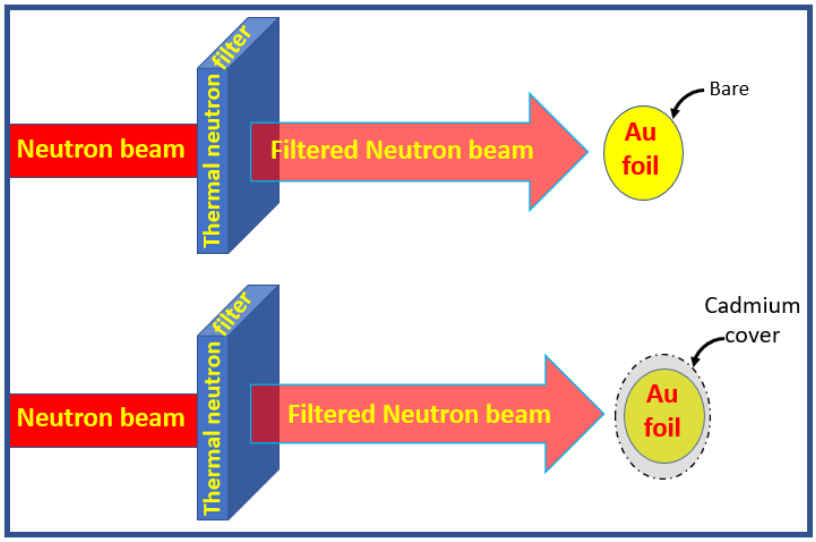

Figure 13: Depiction of gold foil activation measurement setup, with bare (top) and Cd-covered (bottom) Au foils.

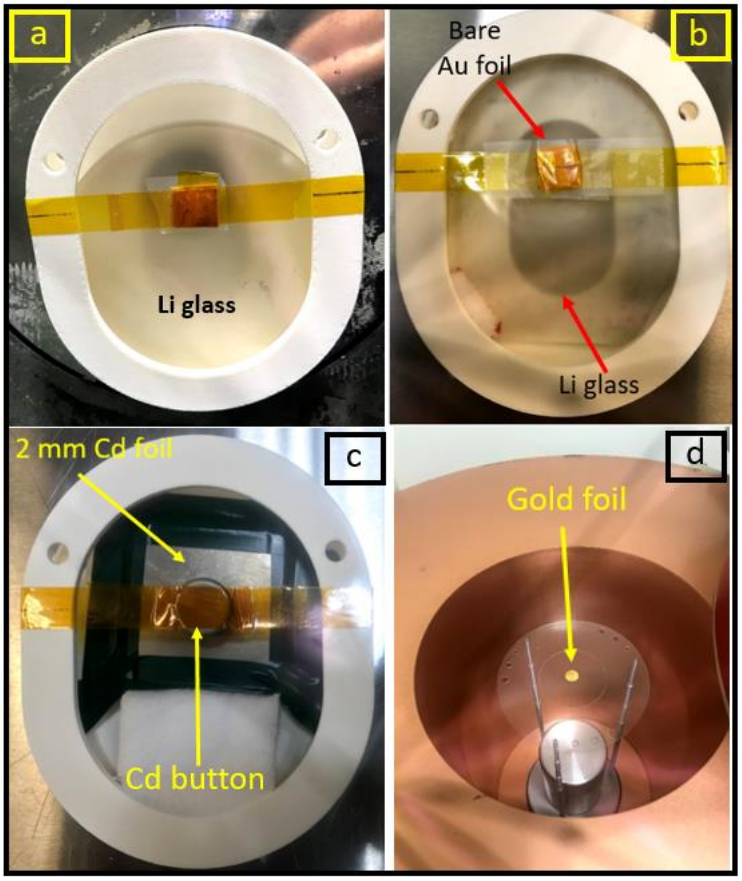

Figure 14: Gold foil activation measurement. Bare gold foils at the irradiation position on the 2.54 cm (a) and 3 mm (b) thick Li glasses, Cd-covered gold foil on the 2 mm thick Cd foil (c), and gold foil placed at the counting position in the HPGe detector (d).

The activated gold foils, then, were counted in a gamma spectroscopy system using an HPGe detector, and saturated activities in disintegration per second per atom (dps/atom) were calculated. The Cd ratio was obtained by dividing the saturated activity calculated from the bare gold foil data by the one calculated from the Cd-covered gold foil data. It can also be defined as the ratio of the total neutron flux, including the thermal flux (ϕ_{Th}) to the sum of epithermal (ϕ_{Epth}) and fast neutron fluxes (ϕ_F), as given in equation 3.1.

$$Cd\ ratio = \frac{Specific\ activity\ (Bare\ Au\ foil)}{Specific\ activity\ (Cd{-}Covered\ Au\ foil)} = \frac{\Phi_{Th}+\Phi_{Epth}+\Phi_F}{\Phi_{Epth}+\Phi_F} \quad (3.1)$$

As a result, the 2.54 cm Li glass and 2 mm Cd foil filters provided Cd ratios of 1.07 and 1.06, respectively, while 3 mm Li glass yielded a Cd ratio of 1.18. Table 1 summarizes the experimental parameters and results of the gold foil activation measurements.

Table 3: Experimental parameters and results of the gold foil activation measurements

Filter	**Gold Foil**						**Cd Ratio**
	Mass (mg)		Irradiation time (hour)		Saturated activity (dps/atom)		
	Bare	Cd-covered	Bare	Cd-covered	Bare	Cd-covered	
3 mm Li glass	261.8	255.9	7.5	7	1.06E-16	9.00E-17	1.18
2.54 cm Li glass	264.1	266.8	3	3	1.52E-17	1.42E-17	1.07
Cd foil	264.6	264.3	3	3	1.26E-16	1.19E-16	1.06

Results showed that 2.54 cm Li glass and 2 mm Cd foil filters provide similar Cd ratio, hence similar thermal neutron removal in the beam. The fact that 3 mm Li glass is not as effective at absorbing thermal neutrons as 2.54 cm Li glass can be attributed to the former's having a smaller amount of Li due to its thickness. In each measurement, the Cd ratio was found to be higher than unity. This implies that after passing the filters, the beam still contains thermal neutrons. Fast neutron thermalization within the filters and the background thermal neutron field in the experimental area may contribute to this outcome.

3.5 Neutron Flux Measurement

The total, thermal, and Epi-Cd neutron fluxes of the beam, while there was not a thermal neutron filter in the beam, were determined employing the multi-foil activation method. This study was performed by the OSURR staff. A total of six foils, of which three of them were bare and the rest were Cd-covered, were used. The table 4 provides the information about the foils used, their mass, and the irradiation time of each.

Table 4: Foils employed in multi-foil activation measurements and their irradiation parameters.

Foil	Mass (mg)	Irradiation time (h*)
Cu-bare	1830.96	4
Au-bare	261.76	1
Ni-bare	1891.98	8
Cu-Cd covered	1701.70	8
Au- Cd covered	264.03	2
Ni- Cd covered	1530.74	8

* For the reactor power of 450 kW

After the foils were irradiated, they were counted using the HPGe detector in a gamma spectroscopy system. Saturated activities in dps per atom of each foil were calculated utilizing the activities (μCi) measured via the gamma spectroscopy system. Table 5 summarizes each foil's measured end of irradiation activity and calculated saturated activity along with the neutron capture reaction in each foil.

Table 5: Measured activities and calculated saturated activities of the foils, as well as the neutron capture reactions that take place during the irradiation.

Foil	Reaction	Measured end of irradiation activity (μCi)	Calculated saturated activity (dps/atom)
Cu-bare	^{63}Cu (n, g) ^{64}Cu	2.28E+00	3.58E-17
Au-bare	^{197}Au (n, g) ^{198}Au	1.98E-01	8.58E-16
Ni-bare	^{58}Ni (n, p) ^{58}Co	1.73E-03	1.49E-18
Cu-Cd covered	^{63}Cu (n, g) ^{64}Cu	1.85E-01	1.74E-18
Au- Cd covered	^{197}Au (n, g) ^{198}Au	6.35E-02	1.37E-16
Ni- Cd covered	^{58}Ni (n, p) ^{58}Co	1.37E-03	1.46E-18

Using calculated saturated activities along with SAND-II and STAYSL Monte Carlo codes, the total, thermal, and Epi-Cd neutron fluxes were calculated, and they are reported in table 6.

Table 6: Total, thermal, and Epi-Cd neutron fluxes of fast neutron beam facility when there is no thermal neutron filter in the beam.

Flux	Flux value (# · cm^{-2} · s^{-1})
Total	2.3E+07
Thermal	0.8E+07 (<0.5 eV)
Epi-Cd	1.5E+07 (0.5 eV>)

3.6 Gamma-ray Content in the Beam

The collimator near the core hosts a 10.16 cm thick polycrystalline bismuth for attenuating gamma-rays in the beam. The gamma-ray transmission in this material was calculated using the Beer-Lambert attenuation law, given in equation 3.2.

$$I = I_0 e^{-\mu\rho x} \tag{3.2}$$

Where:

I : Attenuated beam intensity

I_0 : Incoming beam intensity

μ : Mass attenuation coefficient of the shielding material in cm^2g^{-1}

ρ : Density of the shielding material in gcm^{-3}

x: Thickness of the shielding material in cm

Figure 15 provides the gamma-ray transmission in 10.16 cm thick polycrystalline bismuth for the energy range of 0.5 MeV to 10 MeV.

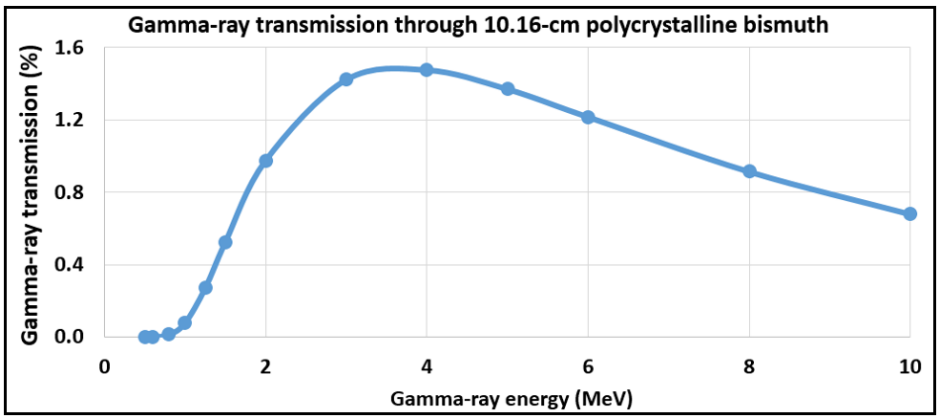

Figure 15: Transmission of gamma rays between 0.5 and 10 MeV in 10.16 cm thick bismuth.

The transmission of gamma-rays with energies up to around 0.8 MeV is negligible due to the high gamma interaction probability of bismuth at lower energies; however, it increases with energy after ~0.8 MeV and reaches the peak value of 1.5 % at around 4 MeV, and then slowly decreases with energy.

The gamma dose rate in the beam was quantitatively investigated using Optically Stimulated Luminescence (OSL) gamma dosimeters while the aforementioned 2.54 cm thick Li glass and 2 mm thick Cd foil filters aforementioned were in the beam. The dosimeter was attached to the surface of the PVT scintillator employed for fast neutron imaging, and the scintillator was placed at the position where it is during neutron imaging experiments. Figure 16 shows photos of the OSL dosimeter and measurement setup.

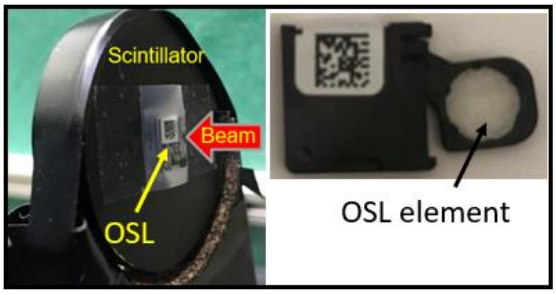

Figure 16: Photos of gamma dose rate measurement setup- OSL is secured on the back of the PVT scintillator (left) and the OSL dosimeter with its gamma-ray sensitive section (right).

Since Cd foil emits prompt gamma-rays upon capturing thermal neutrons, and the effect of these gamma-rays was investigated by measuring the gamma dose rates both when the Cd foil was at the beam exit and when placed behind the shorter collimator. Figure 17 shows a photo in which the Cd foil is placed on the collimator's aperture. In total, gamma dose rates were measured for four different beam/filter configurations. These configurations are depicted in Figure 18.

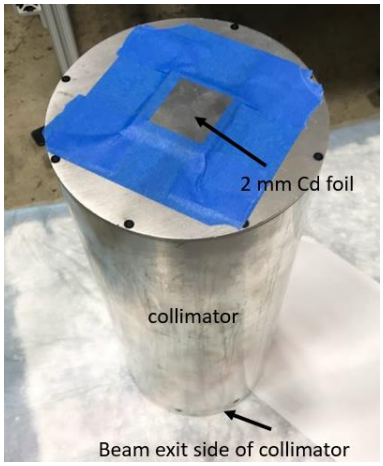

Figure 17: Cd foil attached to collimator.

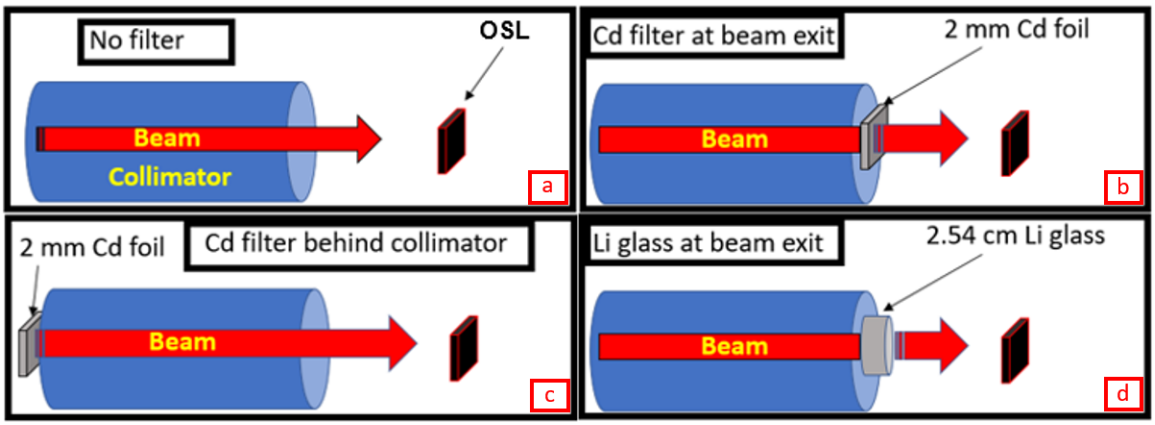

Figure 18: Gamma dose rate measurement configurations. Without filter (a), 2 mm Cd foil at beam exit (b), behind collimator (c), and 2.54 cm Li glass at beam exit (d).

For each configuration, three separate measurements with irradiation times of 5, 10, and 20 minutes were made. OSLs readout process was carried out based on a ^{60}Cocalibration, along with two control OSLs that were not irradiated in the beam (for the purpose of background correction). The reason for choosing ^{60}Co is that the two distinct gamma rays

(1173.23 and 1332.45 KeV) better represent the gamma content in the beam, considering the efficiency of bismuth crystal at attenuating gamma rays with an energy of up to 0.8 MeV. Obtained gamma dose rates in each configuration were averaged to decrease the measurement (random) error. Table 7 gives the gamma dose rates in rad/h of each configuration.

Table 7: Gamma-dose rate measurement results for each beam/filter configuration.

Filter location	Rads/h	Norm. to Li glass value
Cd filter behind collimator	14.12	1.21
Cd filter at beam exit	16.15	1.38
No filter	17.30	1.48
Li glass beam exit	11.66	1.00

The highest gamma dose rate was measured in the absence of a filter in the beam. In this case, the OSL was irradiated by gamma-rays originating only in the beam. When the Cd foil was placed in the beam, gamma dose rates were found to be dependent on where the foil was placed. The gamma dose rate was lower when the Cd foil was placed behind the collimator since the prompt gamma-rays are emitted in the radial direction resulting in fewer of them reaching to the OSL dosimeter. The lowest gamma dose rate was achieved when the Li glass was in the beam because, unlike Cd foil, Li glass produces negligible prompt gamma-rays, meanwhile absorbing some of the gamma-rays found in the beam. The Li glass reduces the gamma dose rate by ~32 % compared to when there is no filter in the beam.

A 2.2 mm thick GLO ($(Gd, Lu, Eu)_2O_3$) scintillator was also employed to explore the beam's gamma-ray and thermal neutron content. The scintillator is sensitive to gamma-rays due to its high-Z composition, and to thermal neutrons because of the presence of Gd.

Open beam radiographs were acquired, with an exposure time of 1 minute each, with and without the 2.54 cm thick Li glass in the beam. The radiographs were acquired using a CCD-based imaging system consisting of an Electron Multiplying (EM) Charged Coupled Device (CCD) camera, a light-tight apparatus and a flat front-surface mirror. The EMCCD employed was Andor iXon Ultra 897 that has active pixels (H x W) of 512 x 512, pixel size (W x H; μm) of 16 x 16, and image area (mm) of 8.2 x 8.2 [57]. The EM gain, which can be set from 3 to 1000, is a feature of the camera that allows charge amplification of recorded in each pixel of the CCD, however, it affects the dynamic range obtained, therefore, especially at high readout rates, it is a recommended practice to apply lower EM gains [58]. Therefore, the EM gain was kept as low as possible whenever possible throughout this study.

Figure 19 shows the main components of the beam and which component is absorbed by which material (here Li glass or the scintillator). Figure 20 shows the post-processed (2-pixel median filter applied) radiographs and provides the relative light outputs.

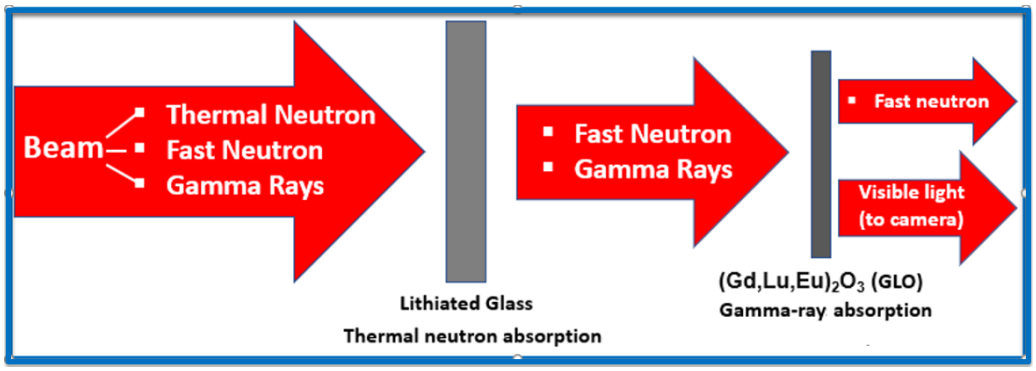

Figure 19: Depiction of the removal of the beam components by Li glass and the GLO scintillator.

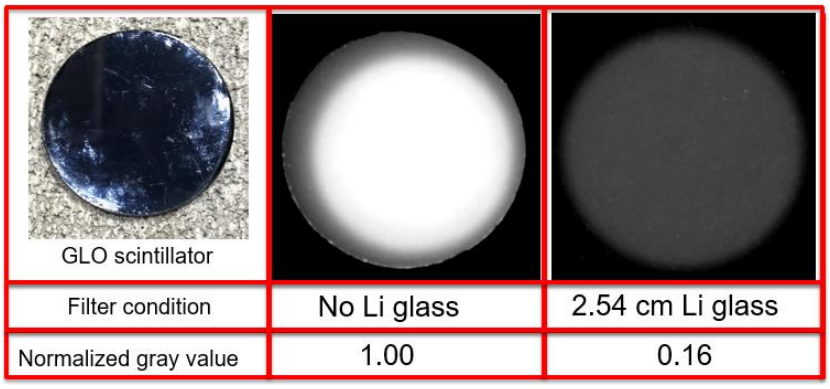

Figure 20: Photo of 2.2 mm thick GLO scintillator (left). Open beam radiographs without (middle) and with (right) Li glass.

Radiographs are in the same contrast level yet shown in log scale. Results showed that the presence of the Li glass in the beam causes an 84 % drop in the light output due to thermal neutron removal. However, the Li glass was not able to remove all the thermal neutrons in the beam as the Cd-ratio was not unity. Additionally, Li glass may act as a moderator and

slow neutrons down to thermal energies, which may cause an increase in thermal neutron content in the beam after being filtered.

3.7 Neutron and Gamm-ray Flux Distributions and Dose Rates

The neutron flux distributions were simulated employing MCNP for both the beam open and closed conditions by rotating the beam-shutter, as needed in the model. The neutron spectrum at the collimator entrance, given in figure 9, was utilized as the neutron source in these simulations. The simulation results are given in figure 21 and indicate that the beam-shutter provides sufficient neutron shielding when the beam is closed.

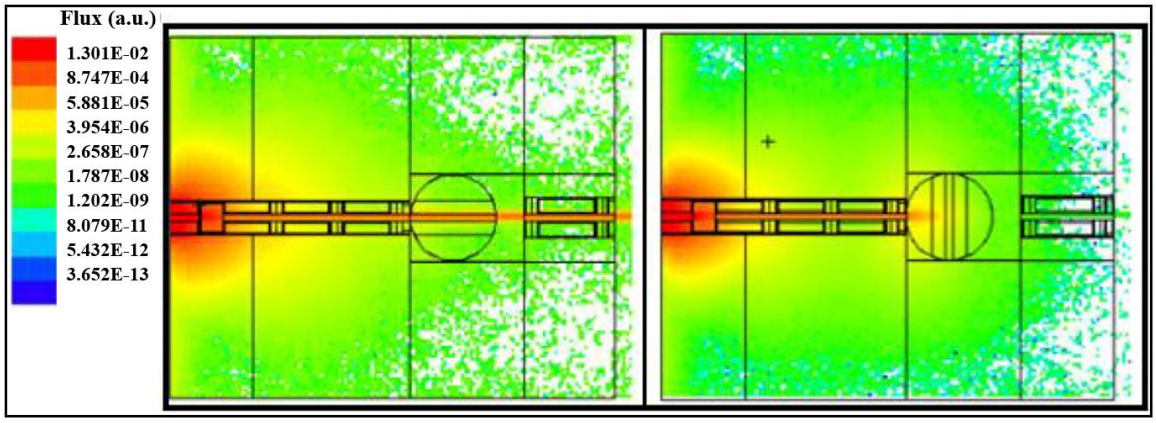

Figure 21: MCNP simulated neutron flux distributions of the beamline for the beam on (left) and off (right) conditions

Simulations were also performed using 2-MeV Gamma-rays, and the results, given in figure 22, show that the beam-shutter yields significant gamma-ray reduction when the beam is in the closed position.

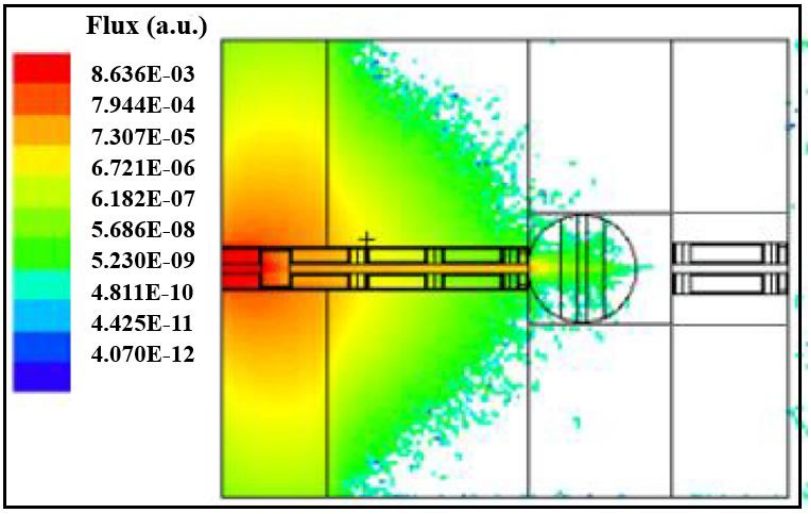

Figure 22: MCNP simulated gamma-ray flux distribution of the beamline for the beam off condition

Simulations were also carried out to acquire neutron and gamma-ray flux distributions, as well as dose rates around the beam stop. In these simulations, the neutron spectrum at the collimator exit, given in figure 9, was used to define the neutron source, and the gamma source was defined as a 2 MeV monoenergetic beam. Simulation results of neutron and gamma-ray flux distributions, along with the regions where the neutron and gamma dose rates were obtained, are given in Figures 23 and 24, respectively. Results showed that the beam stop reduces the incoming gamma-ray and neutron fluxes by ~7 and ~6 orders of

magnitude, respectively, both at the back and sides of the beam stop. Additionally, the simulations also indicated that gamma-rays and neutrons backscattering from the front surface of the beam stop, which may cause an increase in gamma-ray and neutron dose rates.

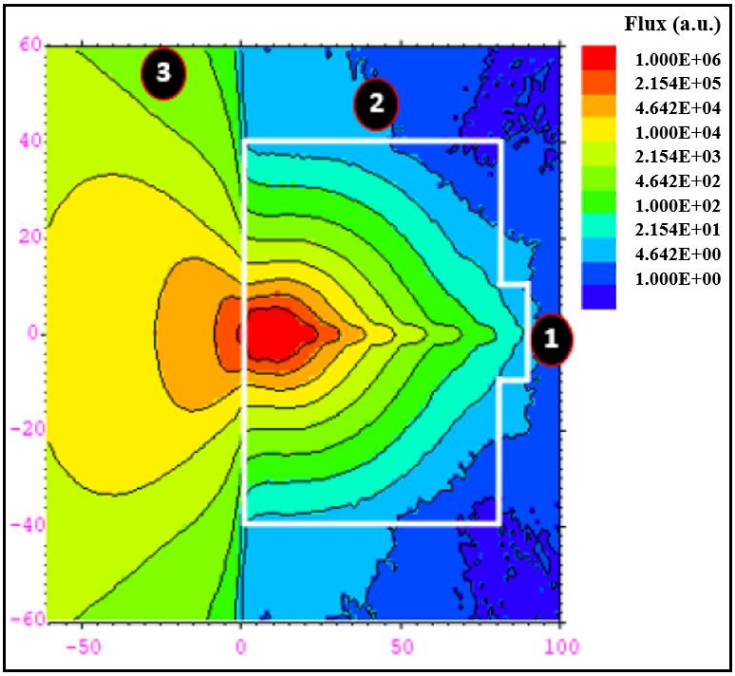

Figure 23: Neutron flux distribution inside and around the beam stop. White lines represent the boundaries of the beam stop.

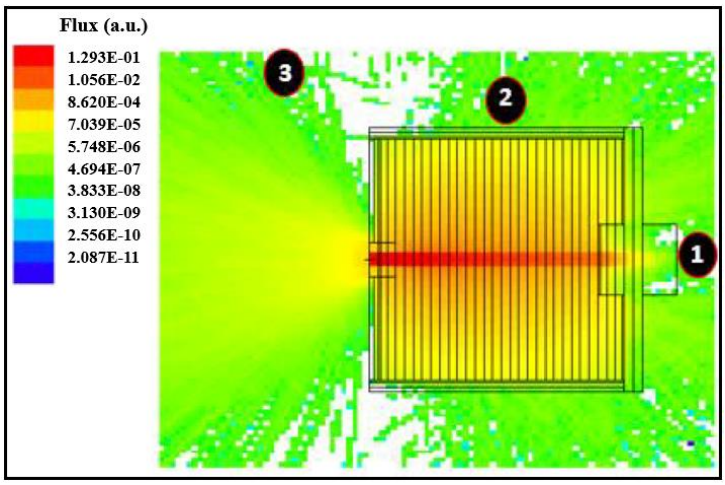

Figure 24: Gamma-ray flux distribution inside and around the beam stop.

Neutron and gamma-ray dose rates were calculated based on the simulation results, and they also were measured experimentally employing a Ludlum neutron dose survey meter and a Victoreen ion-chamber survey meter at 10 % reactor power (50 kWth). Simulated and measured neutron and gamma-ray dose rates are summarized, in mR/h, in table 8. Neutron dose rates obtained from the simulations show close agreement with those from the measurements.

Table 8: Simulated and measured neutron and gamma-ray dose rates at various points around the beam stop.

Region	Neutron dose rate (mR/h)		Gamma dose rate (mR/h)	
	Experiment	Simulation	Experiment	Simulation
1	5.5	4.5	0.4	0.7
2	n/a	4.3	n/a	1.5
3	28	26.4	1.4	1.1

3.8 Beam Profile and Divergence

Beam profile and beam divergence are two of the most important characteristics of a neutron beamline since they have an impact on the quality of neutron radiographs. Therefore, it is of utmost importance to quantitatively determine the beam divergence and investigate the beam profile in terms of uniformity.

A neutron radiograph of the open beam was acquired at a 10 cm distance from the beam exit while the reactor power was at 10% (50 kWth). MCNP radiography simulations were also performed using the beamline model to obtain the beam profile at the same distance. The MCNP input deck of these simulations is provided in appendix A. A volumetric neutron source, in these simulations, was defined to represent the reactor core. Simulations provided radiographs of neutrons passing through the collimators' aperture without any interaction (direct), neutrons that undergo only scattering interactions in the collimators' aperture, and the combination of direct and scattered neutrons (total). The radiographs of the beam profile obtained both from the experiment and simulations are given in figure 25. Although the near-core collimator hosts a gamma-ray filter, the bismuth crystal, it is unable to remove all the gamma-rays, produced in the reactor core, from the beam, which results in the beam having a residual gamma-ray component in the beam. Since the scintillator used in the experiment is sensitive to both neutrons and gamma-rays, the experimental radiograph may also include gamma-ray interactions, whereas the simulated radiographs were generated merely by neutrons. The combined effect of neutron scattering, geometric unsharpness, light scattering in the scintillator, and the electronic noise in the camera may the reason of the blurriness seen in the experimental radiograph.

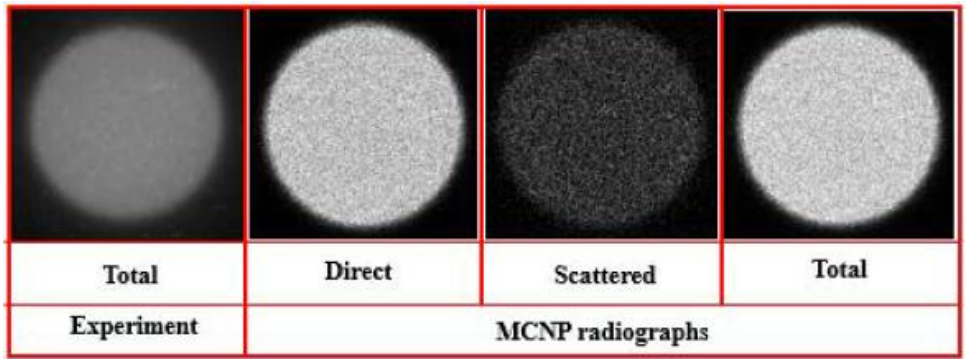

Figure 25: Radiographs obtained experimentally and simulated using MCNP

The neutron flux profiles constructed from the experimental and simulated radiographs along their horizontal centerline are shown in figure 26. The simulation results indicate that neutrons reaching the detector at the beam exit are almost entirely direct, with scattered neutron content around one order of magnitude smaller compared to the total neutron flux. However, the simulated beam profile is in good agreement with the one acquired experimentally. Unlike the experimental radiograph, the simulated radiographs do not include gamma-ray contribution, and this may cause an underestimation in flux in these radiographs. The simulated beam profiles indicate an increase in flux toward the center of the beam, followed by a faster decrease outside the beam boundary compared to the one constructed from the experimental radiograph. The line profile of the experimental radiograph shows a hump-like feature more prominent compared to the simulated radiograph, possibly due to scattered neutrons from the environment. Offset at the edges in the experimental profile may be due to the light scattering background in the scintillator.

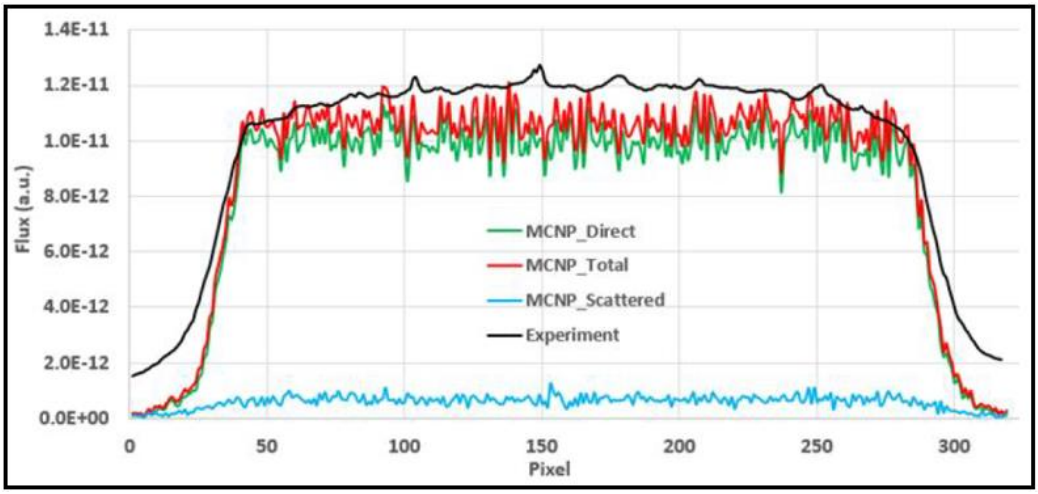

Figure 26: Line profiles of the experimental and simulated radiographs of the neutron beam.

To investigate the beam divergence from the parallel, twelve radiographs of the beam profile were acquired successively with the same image acquisition time of 60 seconds but increasing the distance between the beam exit and the scintillator from 2.74 cm to 12.74 cm. Obtained radiographs were post-processed by applying a 3-pixel median filter to remove salt and pepper noise, and the change in the radius of the beam on each radiograph was calculated. Amongst the post-processed radiographs, the ones taken at 12.74 cm and at 2.74 cm are shown in figures 27(a) and 27(b), respectively. The radiograph taken at 12.74 cm is dimmer compared to the one acquired at 2.74 cm because the number of neutrons reaching the scintillator decreases as a result of beam divergence and neutrons scattered to high angles. The change in radius of the beam on each radiograph with respect to the distance from the beam exit is represented as blue dots in figure 27(c).

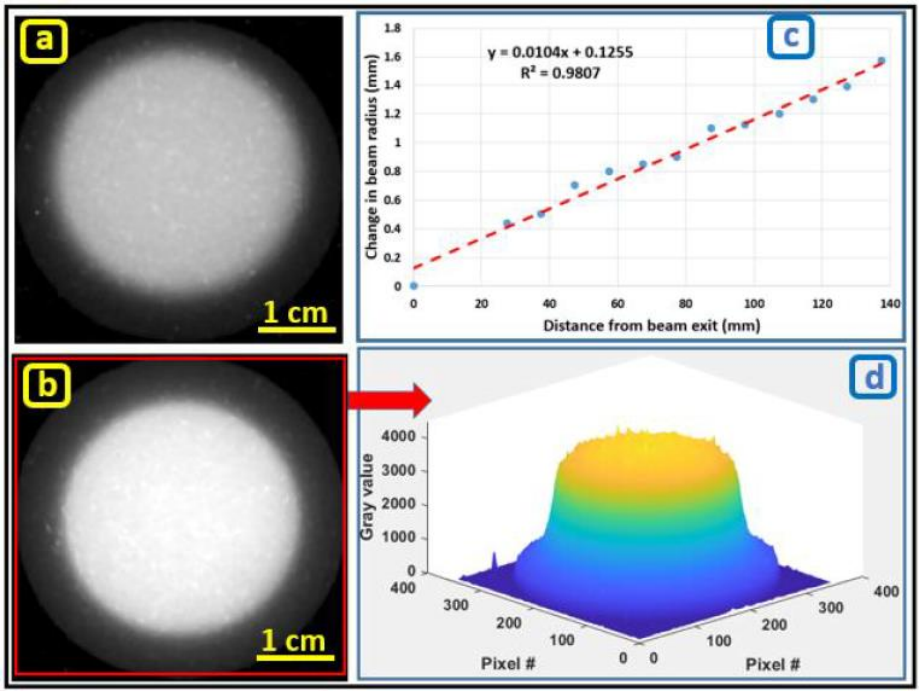

Figure 27: Open beam radiographs acquired at 12.74 cm (a) and at 2.74 cm (b) distances from the beam exit, plot (c) showing the change in the beam radius with respect to the distance from the beam exit, 3D beam profile of the radiograph obtained at 2.74 cm from the beam exit (d).

The data point seen at (0, 0) in figure 27(c) represents the zero radius change in the beam as the distance between the collimator exit and the scintillator is zero. The red dashed line in figure 27(c) was obtained by applying a linear fitting to the data. A beam divergence of ~0.6° was calculated by taking the arctangent of the slope (0.0104) of the fitted red dashed line. The 3D beam profile, seen in figure 27(d), plotted from the radiograph taken at 2.74 cm distance, shows that the beamline provides a relatively flat and uniform neutron beam.

The scattered neutrons with high angles, caused by the lithiated glass, at the beam exit produce radiographs whose brightness do not drop proportionally as the distance between beam exit and the scintillator increases. This effect is depicted in figure 28.

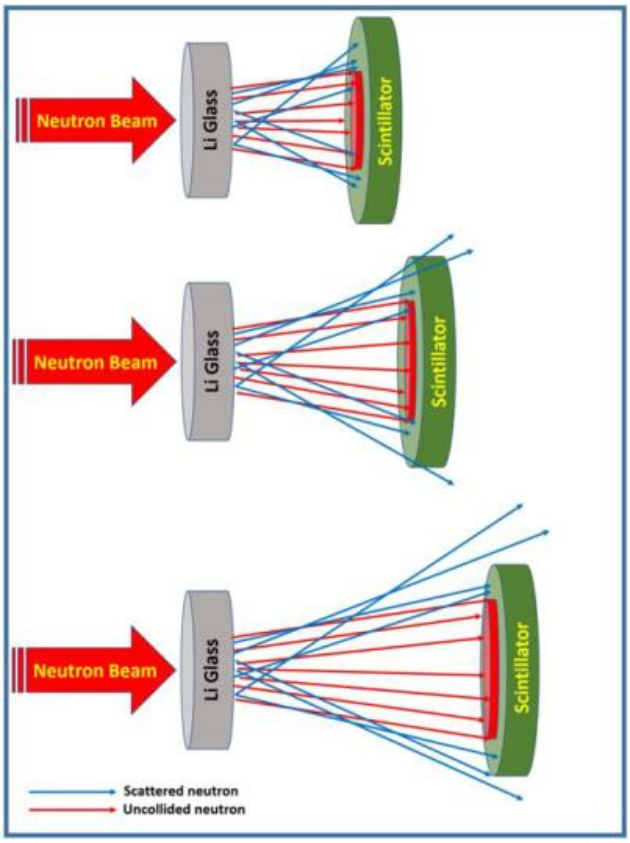

Figure 28: The effect of neutrons scattered with high angles from Li glass filter on radiograph's brightness.

The neutrons scattered with high angles are more likely hit the beam area on the scintillator when the distance between beam exit and the scintillator is short. However, as the distance increases, the likelihood of scattered neutrons reaching the beam area drops, and they start

hitting the scintillator outside of the beam area, and, when the distance is long enough, they do not hit the scintillator. This effect can be seen the on the radiographs by calculating the mean gray value both inside and outside the beam area. Figure 29 shows raw radiographs taken at 2.74 cm and 12.74 cm, as well as the mean gray values of respected regions.

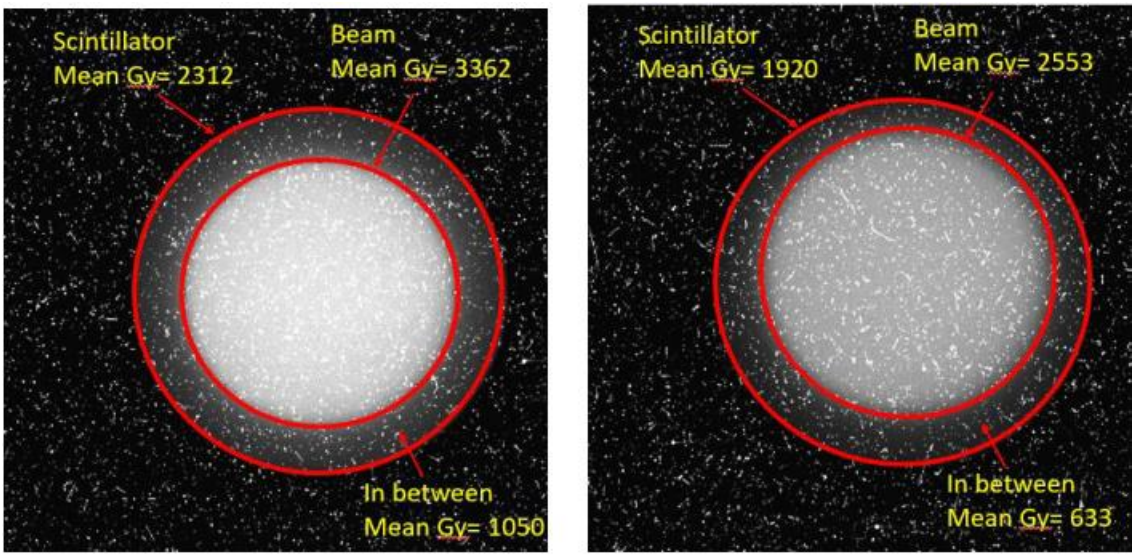

Figure 29: Raw radiographs obtained at 2.74 cm (left) and 12.74 cm (right) distance away from beam exit.

On radiographs, inner and outer red circles represent the beam and the scintillator boundaries, respectively. Going from 2.74 cm to 12.74 cm, the increase in the beam area is ~7.7 %; however, the decrease in the beam mean gray value is ~24 %. The mean gray value of the in-between region, the region between the beam and scintillator boundaries, is ~65 % higher on radiograph taken at 2.74 cm than the one taken 12.74 cm. That means at

long distances fewer scattered neutrons hit the scintillator, causing lower gray values. Additionally, the mean gray value of the scintillator region is ~20 % higher on radiograph obtained at 2.74 cm than the one acquired at 12.74 cm, meaning that the higher the distance between the beam exit and the scintillator the less likely the scattered neutrons will the scintillator.

3.9 Photon Statistics

The photon statistics that is the number of scintillation photons impinging on a pixel per unit time was explored using the radiograph taken at 2.74 cm away from the beam exit. The photon statistics are dependent on various factors, such as mean gray value, Analog-to-Digital Unit (ADU), preamplifier and EM gains of the camera, and the quantum efficiency (QE) of the camera for a specific wavelength of photon. The calculation steps of the photon statistics are depicted in figure 30.

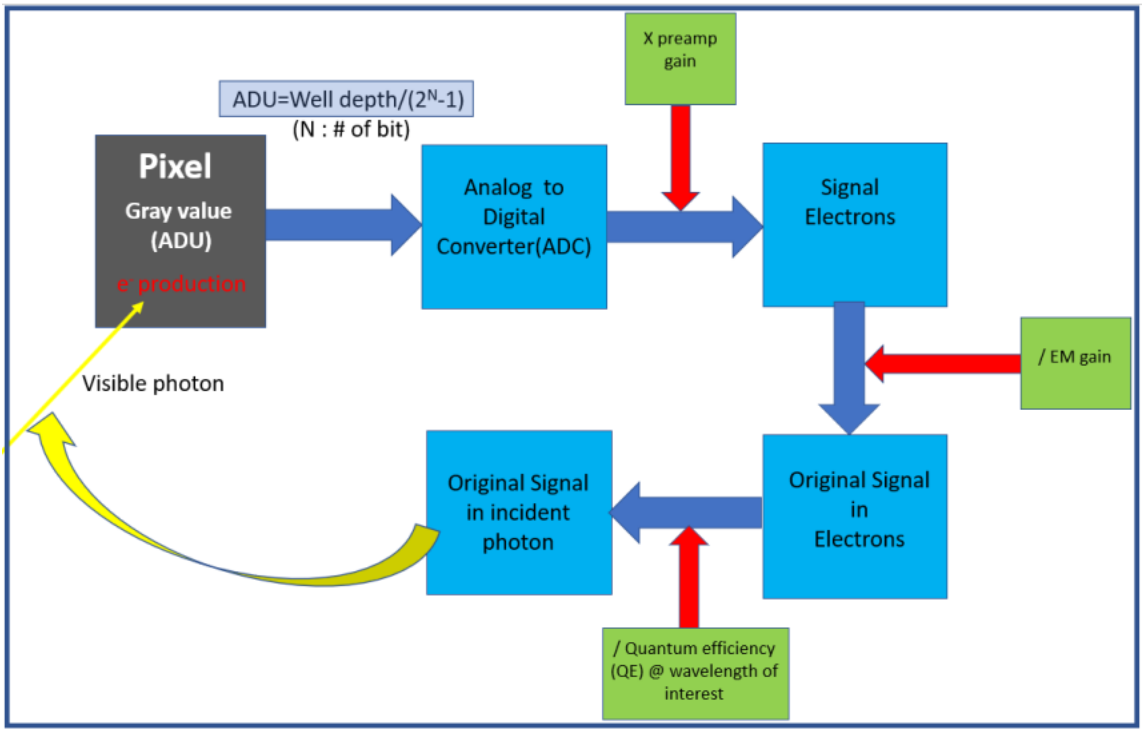

Figure 30: Calculation steps of photon statistics in EMCCD.

Calculations steps were followed, and the photons statistics was calculated using the parameters of gray value (3500), pixel depth (180000 e^-), bit depth (14), preamp (5) and EM (30) gains, and QE (95 % at ~550 nm) [57]. Calculations provided photon statistics of around 112 photon/sec. Since the scintillator emits a spectrum of wavelengths and a single value of QE was used in calculations, the photon statistics found here is a rough estimate of the true value.

Chapter 4. Characterization of Polyvinyl Toluene (PVT) Scintillators for Fast Neutron Imaging

4.1 Introduction

One of the most important components of a CCD-based fast neutron imaging setup is the neutron imager or detector. Therefore, it is crucial to investigate, characterize and determine a proper neutron imager to perform fast neutron imaging applications efficiently. In this study, Polyvinyl Toluene (PVT) based plastic scintillators doped with different fluors and having different dimensions were investigated and characterized in terms of relative light output and spatial resolution.

Fast neutrons deposit their energies into materials mainly via elastic scattering because the reaction cross-sections of all the other possible reactions such as radiative capture and inelastic scattering are relatively lower. This requires a neutron imager or detector to be designed in a way that allows the energy transfer from fast neutrons to be maximized through an elastic scattering reaction. When the reaction kinematics of elastic scattering are taken into consideration, fast neutron detectors that include Hydrogen are well known to yield the highest possible energy transfer since neutron has a similar mass as proton.

4.2 Experimental

4.2.1 Neutron Detector

In this study, Polyvinyl Toluene (PVT) based scintillators, five in total, with different dimensions and fluors were characterized in terms of relative light output and spatial resolution. PVT is a synthetic polymer whose molecular formula is C_6H_4-CH_3-CH_2-CH. Each scintillator tested has been doped with one of the two Iridium-complex fluors named Flrpic and X-Flrpic. While the Flrpic's molecular formula is $C_{28}H_{16}F_4IrN_3O_2$, X-Flrpic consists of a Flrpic with two Xylyls groups. These fluors offer high solubility and the ability to harvest triplet excitons, in addition to singlet excitons, as well as allow wavelength shifting to longer wavelengths, causing green light emission. The molecular structure of PVT, Flrpic and X-Flrpic are shown in Figure 31.

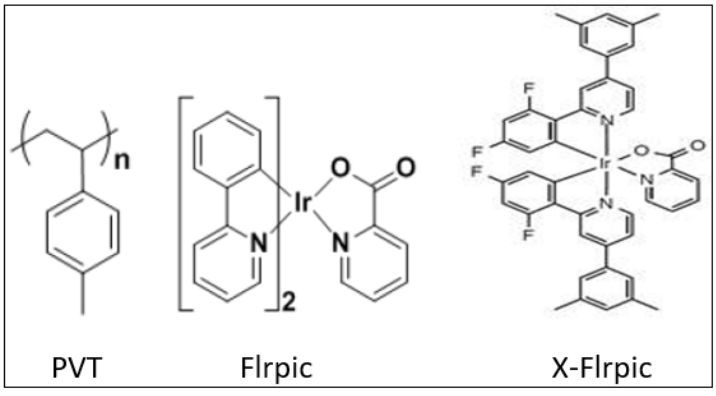

Figure 31: Molecular structure of PVT (base), Flrpic, and X-Flrpic (both are secondary fluors).

In two scintillators, hydrogen atoms in PVT structures have been replaced with deuterium atoms. These two scintillators are named “deuterated”, and they have different characteristics in terms of relative light output and spatial resolution because the stopping power is different than those not deuterated. Based on the reaction kinematics of the elastic scattering, a 2-MeV neutron undergoing a head-on collision with a relatively stationary proton would transfer all its kinetic energy to the proton while the same collision with a deuteron would result in transferring only around 1.78 MeV of its kinetic energy. Simulations performed using the Stopping and Range of Ions in Matter (SRIM) [59] yielded the range of a 2-MeV proton in PVT as 71.62 um, while a 1.78-MeV deuteron in deuterated PVT as 38.65 um. Stopping powers in PVT medium utilizing these ranges were calculated for protons and deuterons as 27.93 KeV/um and 46.11 KeV/um, respectively. Figure 32 shows the energy transfer per track length with respect to recoiled proton’s energy in PVT and deuteron’s energy in deuterated PVT.

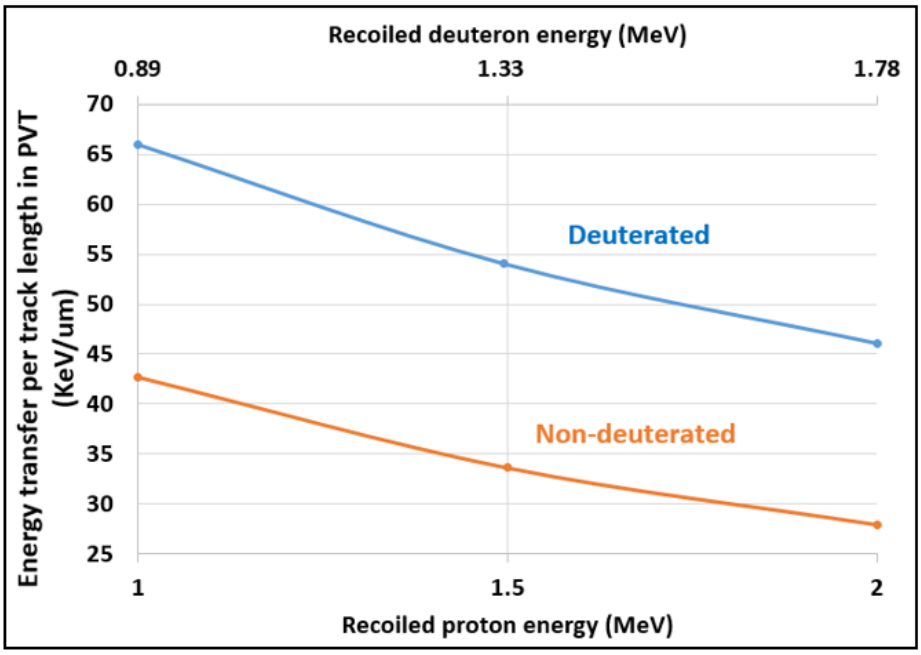

Figure 32: Energy transfer from recoiled proton and deuteron to the PVT and deuterated PVT.

These results reveal that a recoiled deuteron creates a brighter, yet shorter track in a deuterated PVT medium than that of a recoiled proton in non-deuterated PVT. Although the light output per neutron-deuteron interaction is lower, it has a shorter track length, suggesting that the deuterated PVT scintillator should perform better in terms of spatial resolution.

Scintillators were fabricated and provided by Lawrence Livermore National Laboratory (LLNL), and all were prepared with black backings and edge masking to reduce scintillation light scattering. Figure 33 provides the photographs of the scintillators

obtained under room light conditions, while the scintillators' dimensions and the fluors with which they are doped are summarized in table 9.

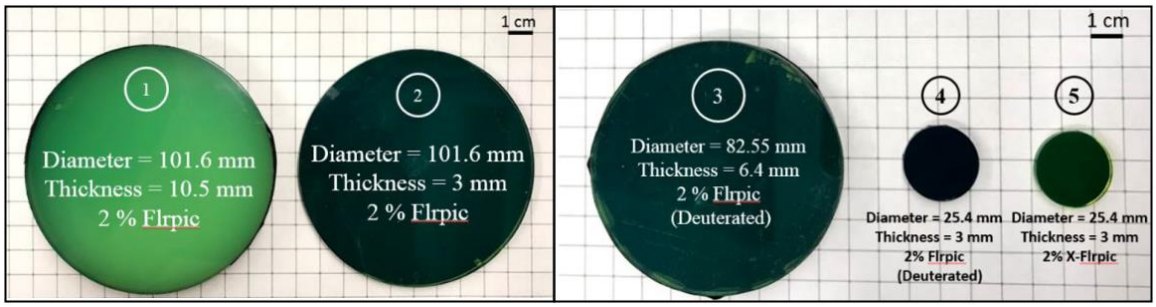

Figure 33: Scintillators investigated for their relative light output and spatial resolution performances with their dimensions and fluors.

Table 9: Dimensions and fluors of scintillators.

Scintillator I.D.	Thickness (mm)	Diameter (mm)	Fluor	Other
1	10.5	101.6	2% Flrpic	-
2	3	101.6	2% Flrpic	-
3	6.4	82.55	2% Flrpic	Deuterated
4	3	25.4	2% Flrpic	Deuterated
5	3	25.4	2% X-Flrpic	-

4.2.2 Neutron Activation in PVT

Neutron activation of chemical elements found in scintillators tested is one of the concerns that can rise the background counts which causes decreasing the Signal-to-Noise Ratio (SNR). Amongst isotopes of all elements that make up PVT and Flrpic, due to having a relatively high neutron capture cross-section (954 barn at 0.025 eV (thermal neutron) and 0.127 barn at 2 MeV), one of the Iridium isotopes, Ir-191, is the biggest contributor to the background count. Assuming a PVT scintillator, which contains 2% Flrpic, irradiated under thermal neutron (0.025 eV) flux of 10^5 $n \cdot cm^{-2} \cdot s^{-1}$ for 20 minutes, it would give $^{192}Ir^*$ activation of ~3.75 x 10^3 $decay \cdot cm^{-3} \cdot s^{-1}$. On the other hand, the same scintillator irradiated under the fast neutron (2 MeV) with the same flux would yield 2 orders of magnitude lower activation, which is ~ 6 $decay \cdot cm^{-3} \cdot s^{-1}$. The effect of the activated ^{192}Ir isotope can be ignored when 2-MeV neutrons are used since the reaction rate of the elastic scattering reaction is around 800 $decay \cdot cm^{-3} \cdot s^{-1}$ in PVT scintillator under the same fast neutron flux.

4.2.3 Neutron Source

This study was carried out at the Ohio State University Research Reactor (OSURR), which is a pool-type, light water moderated reactor with a licensed thermal power of 500 kWth utilizing uranium silicide (U_2Si_3) enriched to 19.5 % as fuel [60]. The OSURR hosts a neutron beam facility that supplies thermal-equivalent neutron flux and fast neutron flux of 4 x 10^6 $n \cdot cm^{-2} \cdot s^{-1}$ and 4.4 x 10^4 $n \cdot cm^{-2} \cdot s^{-1}$ at the imaging position, respectively, while the reactor operates at a power of 450 kW [61]. This beam facility was employed to acquire radiography images. To filter out the thermal neutrons in the beam, a 1.25-cm thick Li glass was utilized since the reaction of ^6Li (n, α) ^3H has a high thermal neutron capture reaction

cross-section of 940 barns. Because the reactor also produces gamma-rays to which scintillators are sensitive, a 5 cm-thick lead brick, which attenuates 2-MeV gamma-rays with ~92.6 %, was utilized to reduce the gamma-ray content in the beam.

4.2.4 Imaging Setup

Radiographs have been acquired using a lens-based imaging system consisting of an Electron-Multiplying (EM) Charged Coupled Device (CCD) camera, a light-tight apparatus, and a front surface mirror. The mirror is positioned inside the light-tight apparatus with an angle of 45° with respect to the incoming beam to prevent the camera from direct neutron radiation as well as to reflect scintillation lights onto the camera sensor. A depiction and photo of the experimental setup are given in figure 34.

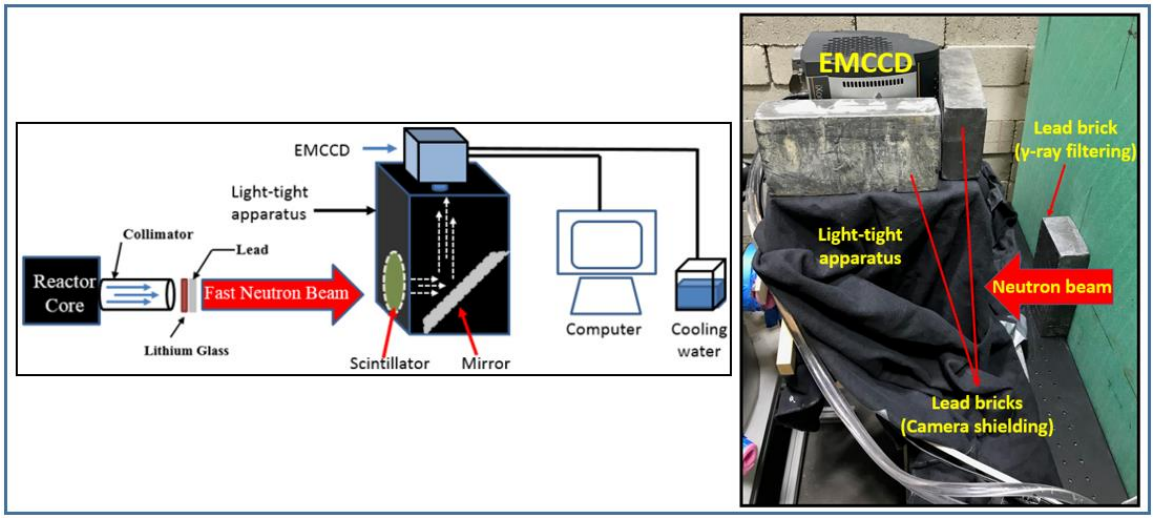

Figure 34: A depiction (Left) and photo (Right) of the experimental setup. The EMCCD (in the photo on the right) is partially shielded with lead bricks to minimize the direct hitting of gamma-rays to the camera sensor.

In a low light yield environment, the EMCCD camera enables acquiring excellent contrast due to its high light sensitivity feature. This is especially crucial for collecting relatively weak scintillation lights caused by neutron-proton elastic scattering reactions with low cross-sections for fast neutrons. The camera was kept cool at -69 °C with the help of ice & water mix circulation and the Peltier thermoelectric cooler feature throughout the image acquisition to minimize the thermal noise. The light-tight apparatus is made from anodized aluminum to minimize neutron activation, and the aluminum is milled to ~0.5 mm where the neutron beam meets the apparatus to further reduce the activation, and black paint was applied to its internal surface to reduce the scintillation light reflection. The light-tightness of the system was increased by covering the light-tight apparatus with a black cloth while

image acquisition took place. Scintillators were placed vertically with respect to the incoming beam within the light-tight apparatus.

4.2.5 Data Analysis

Scintillators were characterized in terms of two distinctive features: the relative light output and the spatial resolution. After acquiring radiography images, image post-processing was performed using the ImageJ software. First, the background correction was performed by subtracting the background image from the raw images. Second, the resulting images were processed with noise and median filters with a radius of 10 pixels and 3 pixels, respectively. Scintillators light output was obtained integrating the grayscale value of the same number of pixels in the illuminated region of each processed image. Since the grayscale value is directly proportional to the amount of light that the scintillator emits, it can be taken as a measure of the light output of the scintillator. Relative light outputs of scintillators for comparison, were calculated by dividing grayscale values by the highest grayscale value.

The spatial resolution of each of the scintillators was calculated employing Modulation Transfer Function (MTF) which was computed from the knife-edge profile radiograph acquired by placing a 15.24-cm-thick hydrogen-rich, neutron attenuator High-Density Polyethylene (HDPE-$(C_2H_4)_n$-Density=~0.95 $g \cdot cm^{-3}$) block in front of the beam. Spatial resolution is provided as lp/mm and μm at 10 % of the MTF.

4.3 Results

The scintillators labeled 1 and 2, each doped with 2% Flrpic fluor, were utilized to investigate the effect of scintillator thickness on spatial resolution and light output since they have different thicknesses. Scintillators 1 and 2 were irradiated for 10 minutes with 100 Electron-Multiplying (EM) gain. Figure 35 shows the post-processed radiographs used for the light output calculation and those employed for obtaining MTFs to determine spatial resolutions. MTF curves obtained with scintillators 1 and 2 are given in figure 36. The exposure time and EM gains were selected such that they both prevented saturation of pixels of the EMCCD camera when testing the thicker 10.5-mm scintillator and allowed sufficient scintillation light collection to perform reasonable comparison when utilizing the thinner 3-mm scintillator.

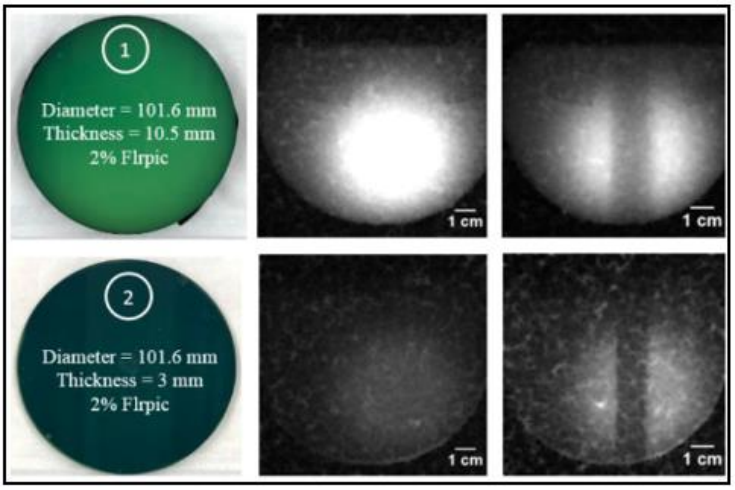

Figure 35: Photos of the scintillators tested (Left). Open beam radiographs (no object in the beam) employed for light output measurements (Middle). Knife-edge radiographs obtained with the HDPE block for determining spatial resolutions (Right).

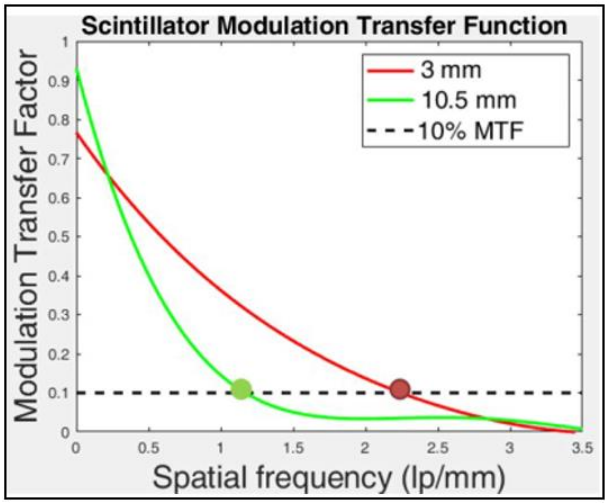

Figure 36: MTF curves generated by knife-edge radiographs of scintillators 1 (10.5-mm thick) and 2 (3-mm thick).

Relative light outputs and spatial resolutions of scintillators 1 and 2 are given in table 10. The 10.5-mm thick scintillator yielded ~2 times higher effective light output compared to the one with 3-mm thick, on the other hand, it performed poorer regarding spatial resolution, due to more neutron and scintillation light scattering.

Table 10: Relative light outputs and spatial resolutions of scintillators tested.

Scintillator No.	Thickness (mm)	Fluor	Normalized light output	Spatial Resolution (µm)
1	10.5	2% Flrpic	1	428
2	3	2% Flrpic	0.48	223

Radiographs of the scintillators labeled 3, 4, and 5 were acquired with the exposure times of 10-, 15-, and 15-minutes, respectively, with the same EM gain of 100. Figure 37 shows the knife-edge profile radiographs along with the white beam radiographs taken for the light output measurement. The white beam radiographs have been set in the same contrast level to be able to make the comparison of light output with a normal human eye perception.

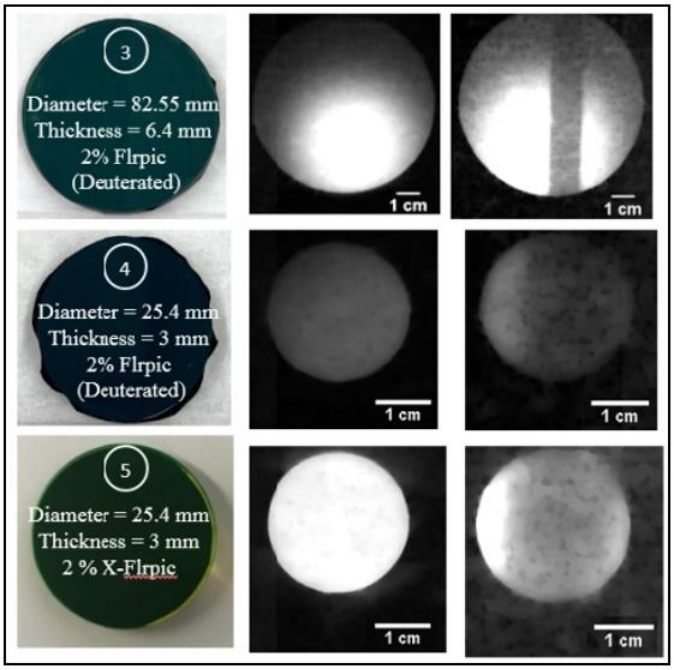

Figure 37: Photos of the scintillators tested (Left), White beam radiographs obtained for light output measurement (Middle), Knife-edge profile radiographs (Right)

Scintillator 3 (6.4-mm thick) yielded the highest light output, and it was utilized for normalizing light outputs of other scintillators. The MTF curves of the scintillators 3, 4, and 5 are given in figure 38, and relative light outputs and spatial resolutions are summarized in table 11.

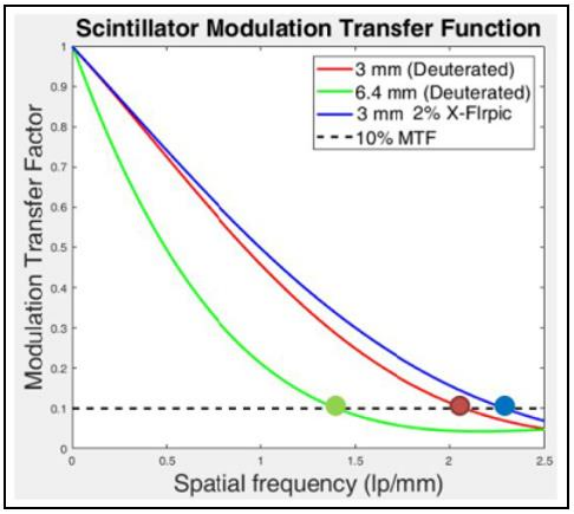

Figure 38: MTF curves, providing the spatial resolutions of the scintillators 3, 4, and 5.

Table 11: Relative light outputs and spatial resolutions of scintillators 3, 4, and 5.

Scintillator No.	Thickness (mm)	Fluor	Other	Normalized Light output	Spatial Resolution (µm)
3	6.4	2% Flrpic	Deuterated	1.0	357
4	3	2% Flrpic	Deuterated	0.38	240
5	3	2% X-Flrpic	-	0.88	219

The effect of scintillator thickness on light output and spatial resolution was revealed by comparing the results of the scintillators 3 and 4 since they both are deuterated and doped with 2 % Flrpic, but they have different thicknesses. The 6.4-mm thick deuterated scintillator provided ~ 2.6 times more light emission than the one 3-mm thick, however, it showed worse performance in terms of spatial resolution. The scintillator doped with 2 % X-Flrpic yielded around 2.3 times higher light output compared to that of the deuterated scintillator 4 doped with 2 % Flrpic although they have the same thickness of 3 mm, and it

also gave better spatial resolution. Scintillators labeled 3, 4, and 5 results allow determining the combination of fluor and thickness of a scintillator that yields the best spatial resolution and the highest light output. It is worth noting that while deuteration was originally thought to be a pathway to improving spatial resolution, since scattered deuterons have shorter track lengths than protons, they also produce less light in the short tracks due to exciton-exciton annihilation. The light yield reduction of about a factor of 2 degrades the performance, resulting in a worse MTF, even though the deuteron track length is shorter.

4.4 Conclusion

In this study, PVT based plastic scintillators fabricated in various dimensions and doped with different fluors have been investigated for fast neutron imaging. Relative light output and spatial resolution of the scintillators were calculated utilizing white beam and knife-edge radiographs, respectively, obtained employing a CCD-based image acquisition system. Results showed that between 10.5-mm and 3-mm thick scintillators, both doped with 2 %Flrpic, the 10.5-mm yields 2 times more lights due to higher scintillating materials with which neutrons interact; however, it provided worse spatial resolution because of more neutrons and scintillation lights scattering within the scintillator. Comparisons also revealed that replacing hydrogen with deuterium in PVT does not increase the performance in terms of spatial resolution, mainly due to light yield degradation.

Chapter 5. Quantifying Spatial Resolution in a Fast Neutron Radiography System

5.1 Introduction

Spatial resolution of a neutron imaging system is a multifaceted parameter that is effected by four major categories, including 1.) neutron source characteristics (spot size, collimation, Cadmium ratio), 2.) test targets (neutron capture vs scattering cross sections, target geometry and thickness), 3.) neutron detector (scintillator thickness, neutron capture and/or scattering cross section in the scintillator, pixel size of camera or flat panel array), and 4.) optical components (mirror, lens, pixel size, dark current of a CCD camera) when the system is based on lens-coupled readout. Many of the archived studies for the spatial resolution of neutron imaging systems have quantified the contributions of these factors but are lacking significant consideration of the effects of test target itself on the overall spatial resolution. The neutron detection mechanism in a lithium enriched thermal neutron imager occurs via neutron capture reaction in which ^{6}Li disintegrates into two charged particles i.e., alpha particle and triton [62] [63]. The resulting charged particles lose energy as they travel in the thin scintillator medium, similar to the recoiled proton originating from the neutron-proton elastic scattering reaction losing energy in the PVT medium. Relatively high spatial resolution obtained in thermal or cold neutron imaging is due to the use of a low energy neutron beam with minimum scattering effects and a thin scintillator. At higher neutron energies, however, the spatial resolution starts degrading because the energy deposition mechanism changes from capture to scattering, and the thickness of the scintillator detector material needs to be increased to compensate for the decreasing interaction cross-section.

In terms of the optimal detector thickness in the fast neutron imaging, one study utilizing fission neutrons obtained a spatial resolution of 200 μm with 3 mm thick poly-ethylene (PE) on which a 0.06 mm thick ZnS:Ag is coated [64]. Polyvinyl Toluene (PVT) scintillators ranging from 3 mm to 10 mm with different emitting dopants were evaluated for optimized resolution and light yield using a reactor based fast neutron beam [65] [66]. Thin Gadolinium (Gd) or Cadmium (Cd) foils are normally used as testing targets in thermal (or cold) neutron imaging for their high thermal neutron capture cross-section (~257,000 barns for ^{157}Gd and ~48,000 for Gd), in which case the neutron capture dominates the attenuation, and the neutron scattering is negligible. Sufficient target thickness is required to induce the detectable contrast in fast neutron imaging, but thick targets introduce an increased intrinsic scattering that complicates the knife edge methods for characterizing the system spatial resolution.

The main objective of this study is to explore the effect of thickness on spatial resolution for an imaging target with high scattering cross-section in fast neutron imaging. A collimated research reactor fast neutron beamline (divergence ~0.6°) and a Polyvinyl Toluene (PVT) based plastic scintillator are used in the study. For the test target, dense materials with high elastic scattering cross-section for fast neutrons, Tantalum (σ_{El}≈4.16 barns @ 2 MeV, ρ=16.65 g/cm3) and Tungsten (σ_{El}≈3.80 barns @ 2 MeV, ρ=19.3 g/cm^3) were selected. The acquired knife-edge radiograph was used to generate the modulation transfer function (MTF), which gives the spatial resolution of the overall imaging system [67] [68]. Additionally, this study investigates the impact of the interaction kinematics between neutrons and Hydrogen nuclei in the PVT detector material on spatial resolution.

5.2 Experimental

5.2.1 Beam Facility and Experimental Setup

MTF data were collected at the fast neutron beam facility of The Ohio State University Research Reactor (OSURR). A 2.54-cm thick Li glass was placed in the beam to remove thermal neutrons via the ^{6}Li (n, ^{4}He) ^{3}H thermal neutron capture reaction. Radiography data acquisition was performed employing a CCD-based imaging system, comprised of an Electron Multiplying (EM) Charged Coupled Device (CCD) camera cooled by water circulation to decrease thermal noise, and shielded with borated polyethylene sheets and lead bricks to lower the effect of neutrons and gamma rays on the CCD sensor, a light-tight apparatus, and a front surface mirror placed at 45° with respect to the incoming neutron beam, both to reflect scintillation lights onto the camera sensor and to prevent the camera being exposed directly in the neutron beam. A 1-cm thick high light yield (HiLY) Polyvinyl Toluene plastic scintillator, providing ~3X more light compared to a conventional PVT scintillator, doped with an Ir-complex fluor (FIracac), is shown in Figure 39(d). The scintillator, provided by Lawrence Livermore National Laboratory (LLNL), was used as a neutron detector [69] [70] [71]. The back and edges of this scintillator were blackened to minimize optical scatter. Additionally, a rotation stage was utilized to rotate foils, placed on a wooden holder attached to the rotation stage, to align the edge of the foil with the scintillator and the beam. A linear XYZ stage was employed to adjust the foil position with respect to the scintillator. Figure 39 provides a depiction of the experimental setup, as well as photographs of the rotation stage as the 6 mm thick Ta foil being set on the wooden holder and partial experimental setup.

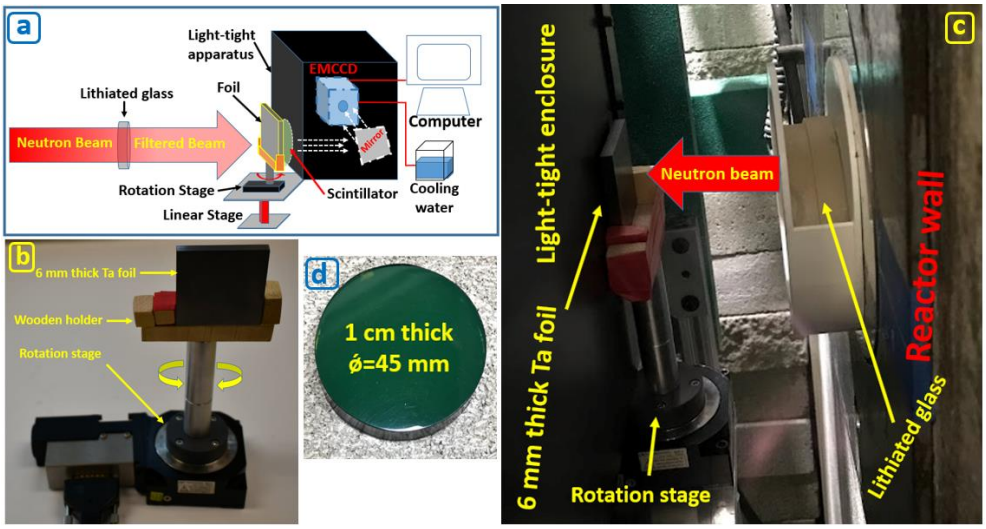

Figure 39: Schematic of the experimental set-up (a), the rotation stage with 6 mm thick Ta foil placed on a wooden holder (b), the sample mounting set up and rotation stage (c), and the HiLY scintillator used (d).

5.3 Results and Discussion

5.3.1 Factors Effecting Spatial Resolution

Before diving into the effect of test target on the system resolution, we analyze other major factors on the system resolution, including the collimation and the energy spectrum of the neutron beam, the ambient radiation field, neutron scattering within samples, type of neutron detector material and its thickness, optical paths of the camera and lens, and the post-processing of the images for noise removal. The EMCCD camera, employed in this study, has a pixel size of 16 x 16 μm^2, and a 50 mm fixed focal length lens was connected to the camera. This optical configuration provided an effective pixel size of 84 µm. Although shielding materials were placed around the camera, the imaging sensor within

the camera is not completely free from the ambient neutron and gamma radiations. These interactions, especially the direct interactions of neutrons in silicon, produce saturated pixels appearing as white spots and/or lines in the radiographs requiring post processing via digital filtering that would negatively impacts the achievable spatial resolution.

Fast neutrons deposit their energy into a medium mostly via elastic scattering. In this study, a PVT-based plastic scintillator whose chemical formula C_9H_{10} was utilized. Due to the conservation of energy and momentum, neutrons interacting elastically with protons transfer more energy into the scintillator medium than those interacting with Carbon nuclei. The trajectory and the range of the recoiled proton in the scintillator medium are dependent on the neutron beam energy spectrum, the interaction angle, energy of the recoiled proton, and the composition of the medium. Knowing the maximum range of the recoiled proton in the vertical direction can provide information regarding the lowest limit of spatial resolution due to neutron-proton scattering in the scintillator. Therefore, to obtain the trajectory and energy of the recoiled proton (in the laboratory frame), a simplified monoenergetic 2 MeV neutron is used in the calculations according to $E_p=E_n(Cos\theta)^2$ equation at different recoil angles from 0° to 85° with an increment of 5°. To acquire the ranges of the recoiled protons, Stopping and Range of Ions in Matter (SRIM) simulations were performed in the medium of PVT. Figure 40 provides vertical and horizontal ranges of protons recoiled with various angles, upon interacting with a neutron impinging on the scintillator surface perpendicularly.

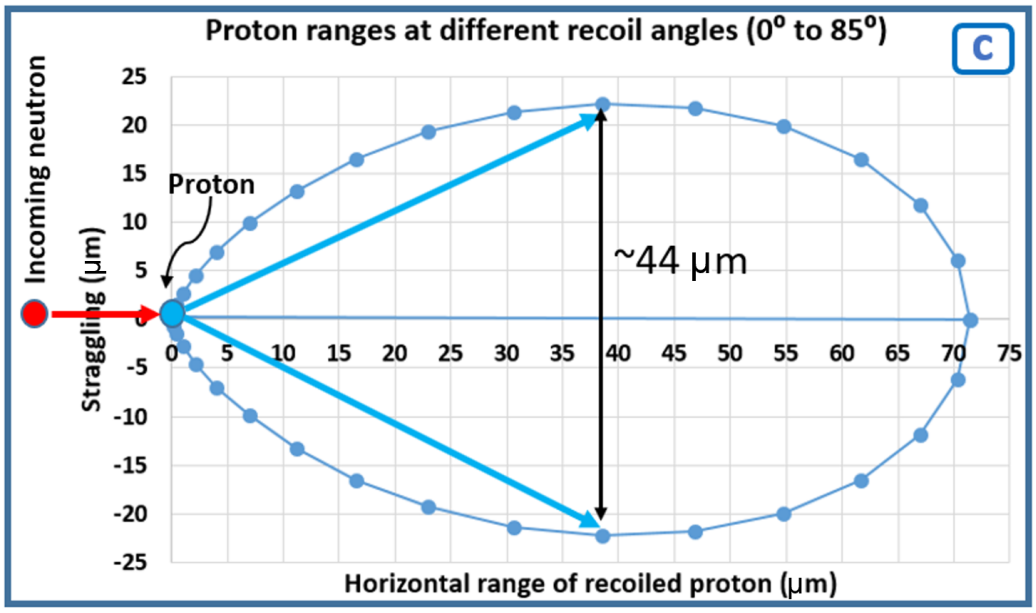

Figure 40: Ranges of protons recoiled from a 2 MeV neutron impinging perpendicularly on a PVT medium.

According to this calculation, when there is a knock-on collision, the recoil proton has a maximum horizontal range of 71.4 μm. Recoil protons at 30° have the maximum vertical range of ~22 μm, which yields ~44 μm maximum spread when considering protons may be recoiled in both directions. This result shows that ~44 μm is the lowest theoretical value for the achievable resolution that can be achieved with 2 MeV neutrons interacting with a PVT detector, assuming no optical scattering. The lowest theoretical achievable resolution value drops to ~31 μm when considering the beam's median energy of 1.6 MeV.

Figure 41 shows another scenario in which the angle between the direction of the incoming neutron and the scintillator surface normal is 30°. In this case, the oval shape rotates counterclockwise around the interaction point, producing a ~51 μm spread in recoil protons. The spread decreases to ~47 μm when utilizing 1.6 MeV neutrons. This shows

that neutrons penetrating at any angle other than normal to the scintillator surface can cause further degradation in spatial resolution.

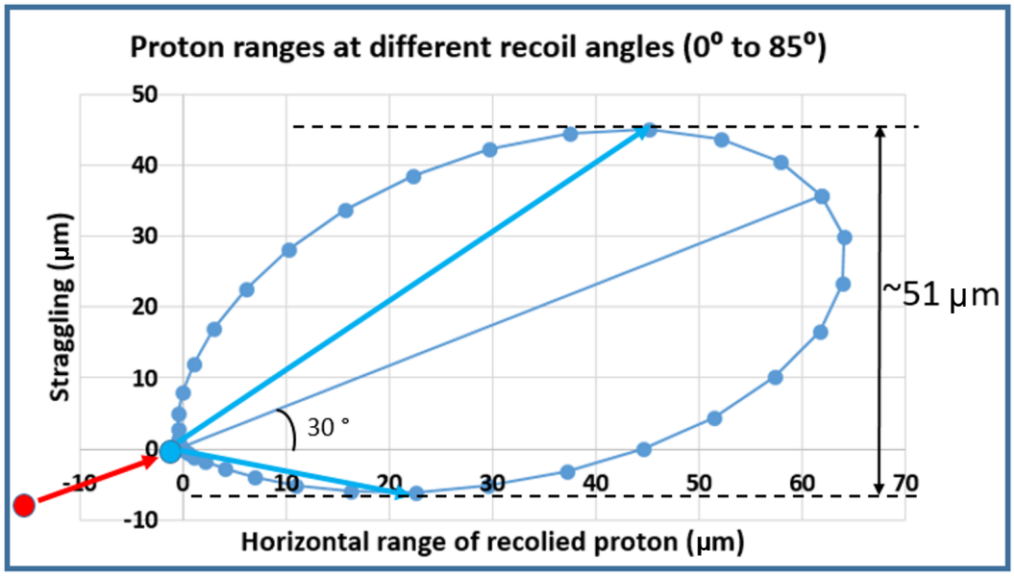

Figure 41: Ranges of protons recoiled from a 2 MeV neutron with a penetration angle of 30° between the direction of the incoming neutron and the scintillator surface normal.

Calculations and SRIM simulations show that the maximum vertical range spread is proportional to the energy of incoming neutrons. For the commonly employed 14 MeV D-T neutrons at normal incidence on the scintillator surface, the maximum vertical range is calculated to be ~1.28 mm, which is ~56 times higher than that is obtained with 2 MeV neutrons.

5.3.2 Edge Method Results and Discussion

To obtain the relation of MTF versus thickness of the test target, foils of 3-mm 99.99% Ta, a 6-mm 99.9% Ta and a 2.54 cm 99.95% W cube were used to acquire knife-edge radiographs. Radiographs of the edges of Ta foils and the W cube were acquired as they were placed on the wooden holder, which was connected to a rotation stage. To obtain the best alignment possible with the scintillator and the beam, the foils and the cube were stationed as parallel as possible to the scintillator, and then rotated in both clockwise and counterclockwise directions with an increment of as small as 0.1°, when the knife-edge radiographs were being collected. All radiographs were acquired with an exposure time of 120 seconds and EM gain of 20; the distance between the scintillator and the imaging target was kept at ~1 mm. Additionally, open-field and dark beam (As the beam shutter was closed, and the reactor on) images were also collected for each sample. The dark beam image was subtracted from both the open beam image and the radiograph taken with a sample. The resulting radiograph of a sample was divided by the resulting open-field beam image, then a 4-pixel median filter was applied to the final radiograph to remove electronic noise (salt and pepper noise). Furthermore, saturated pixels occasionally found, which are white spikes on the radiographs that are caused by direct hits (neutron captures and gamma rays) in the camera sensor, were removed using a median filter with varying pixel sizes depending on the severity of the saturation [72] [73]. After post-processing, edge spread functions of each set of radiographs were generated, and comparisons were made in each set to determine the best-aligned radiograph. Figure 42 provides three edge-radiographs of 5 cm thick Ta foil obtained at -1.0°, -2.0°, and -3.0°, and the edge spread functions of red rectangular regions.

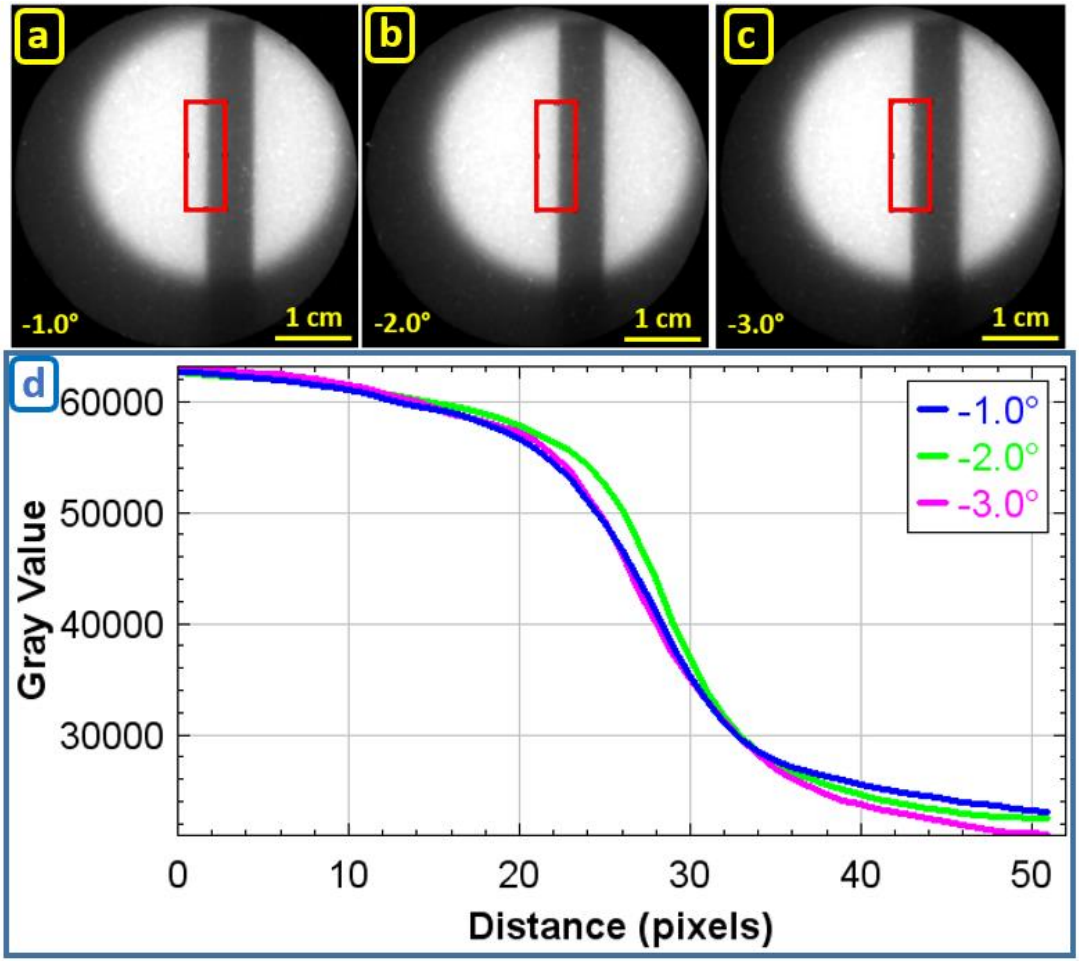

Figure 42: Knife-edge radiographs of 5 cm thick Ta foil taken at -1.0° (a), -2.0° (b), and -3.0° (c) , edge-spread functions of red rectangular regions (d).

The edge-spread functions in Figure 42(d) reveal that the radiograph taken at -2.0° has the best alignment, as it is otherwise impossible to differentiate with visual inspection. Figure 43 shows the photograph, the obtained knife-edge radiograph, and the edge-spread function corresponding to the red rectangular region on figure 43(b1), 43(b2), 43(b3), and 43(b4) of 3 mm, 6 mm, and 5 cm thick Ta foils and 2.54 cm thick W cube, respectively.

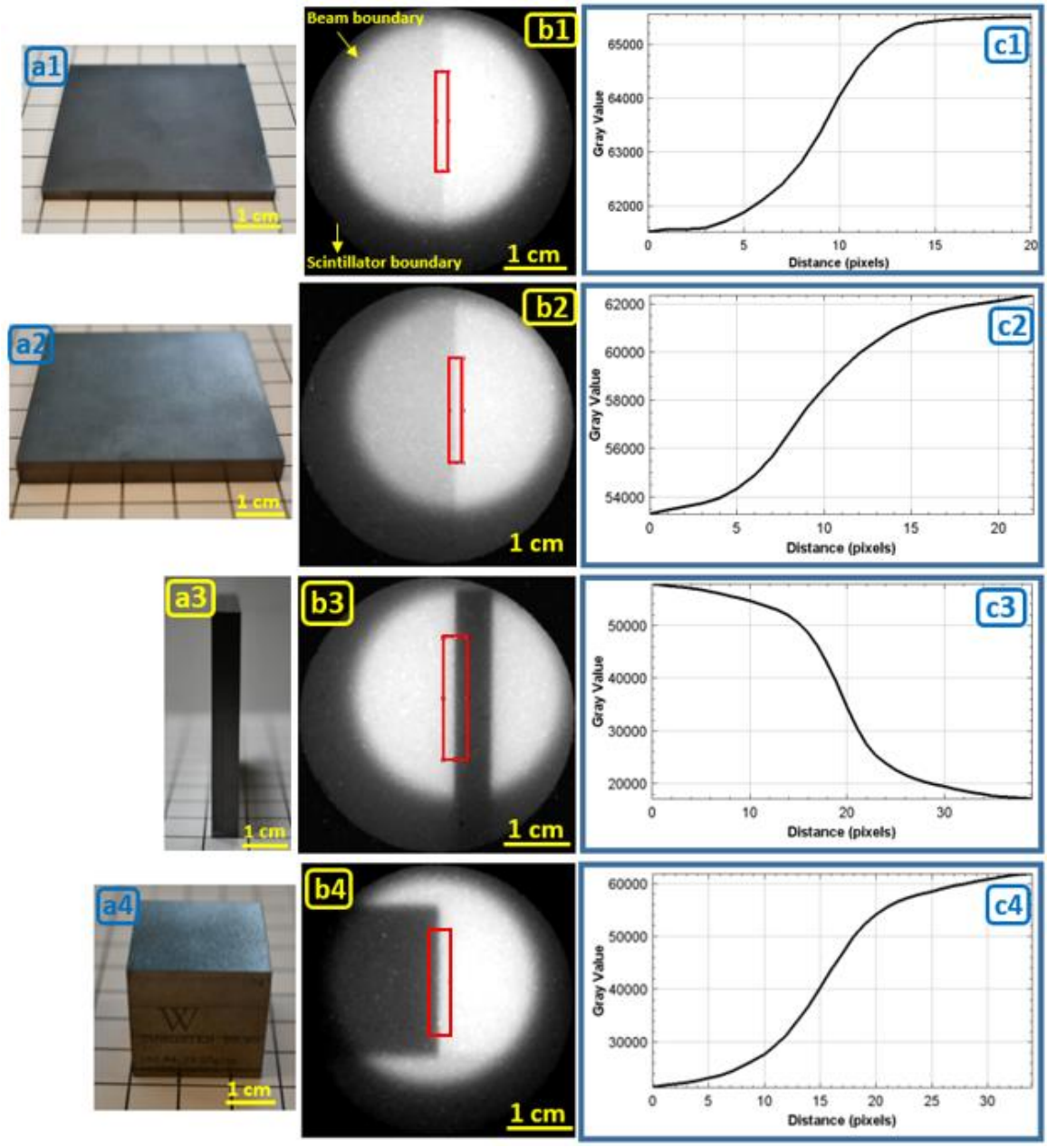

Figure 43: Photograph (a1), knife-edge radiograph (b1), and line profile crossing the red rectangular region on the knife-edge radiograph (c1) of 3 mm thick Ta foil / Photograph (a2), knife-edge radiograph (b2), and line profile crossing the red rectangular region on the knife-edge radiograph (c2) of 6 mm thick Ta foil / Photograph (a3), Knife-edge radiograph (b3), and line profile crossing the rectangular region on the knife-edge radiograph (c3) of 5 cm thick Ta foil / Photograph (a4), knife-edge radiograph (b4), and

line profile crossing the red rectangular region on the knife-edge radiograph (c4) of 2.54 cm thick W cube.

In radiograph (b1) in Figure 43, the left half of the beam is occluded by the 3 mm thick tantalum, blocking ~5% of the 1.6-MeV neutrons from reaching the scintillator. Beam and scintillator boundaries are also indicated by yellow arrows on the radiograph. The line profile, given in Figure 43(c1), of the region shown as red rectangular on the radiograph, provides information about how rapidly the gray value (proportional to the number of neutrons hitting the scintillator) changes at the edge of the Ta foil. The leveling off of the gray value at upper right and lower left sections in the plot represents the open beam, where there is no Ta foil covering the beam, and the beam covered by Ta foil, respectively. Figure 43(b2) shows the knife-edge radiograph taken with 6 mm thick Ta foil. Since the thickness of the Ta foil is doubled (compared to the data shown in Figure 43(a1) from the 3 mm foil), the region where Ta foil occupies on the radiograph is darker than that of the 3 mm radiograph. This can also be seen by comparing the lowest gray values on both line profiles.

The knife-edge radiograph of the 5 cm thick Ta was acquired by aligning the 6-mm thick Ta foil parallel to the beam, in other words, to image its side which is 5 cm long. The obtained radiograph is given in figure 43(b3). As expected, 5 cm yielded the highest contrast among all Ta foil thicknesses. The Knife-edge radiograph of the Tungsten cube is given in Figure 43(b4). Sufficient contrast was achieved due to the thickness of the cube.

Figure 44 shows the relation between the contrast (%) calculated via ((Maximum grayscale value-Minimum grayscale value) / (Maximum grayscale value + Minimum grayscale value)) X 100, obtained from the line profiles of Ta foils and W cube and the foil/cube thickness. A linear relation between the contrast the foil/cube thickness arises because the neutron absorption becomes more probable with increasing thickness.

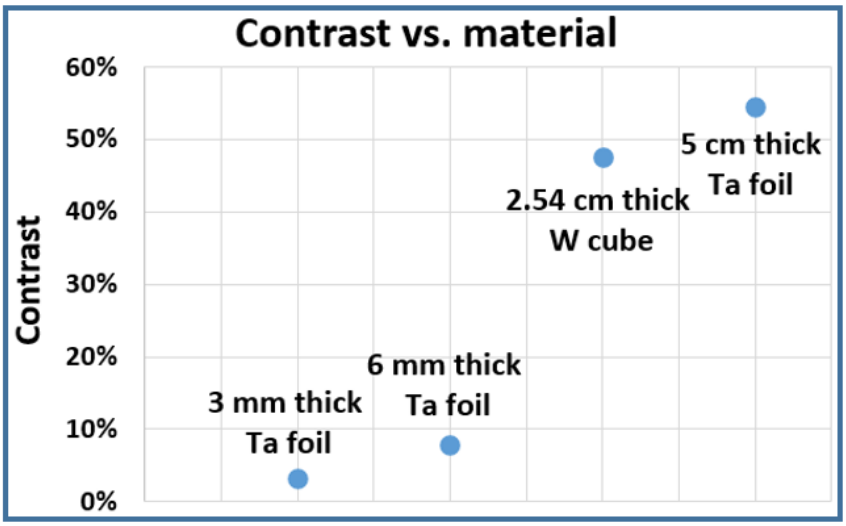

Figure 44: The difference of maximum and minimum grayscale values in the line profiles of radiographs with respect to foil/cube thickness.

Red rectangular regions on each knife-edge radiograph in Figure 43(b1), 43(b2), 43(b3), and 43(b4) were cropped and uploaded into a MATLAB script, which creates the line spread function by taking the derivative of the edge-spread function and generates the modulation transfer function by applying fast Fourier transform (FFT) to the line spread

function. The modulation transfer functions, shown in figure 45, deliver information regarding spatial resolutions of knife-edge radiographs.

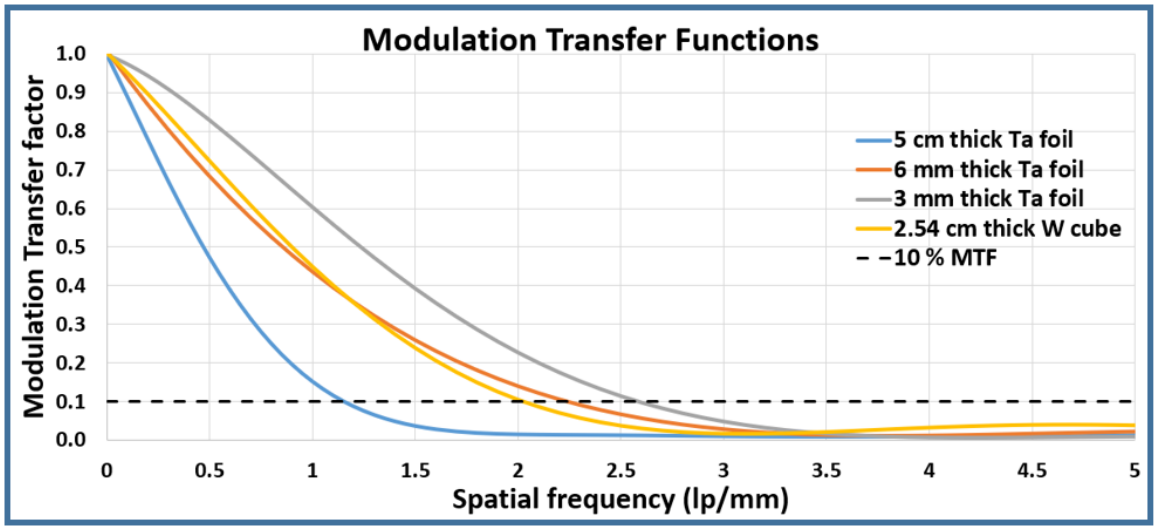

Figure 45: Modulation transfer functions of knife-edge radiographs obtained using Ta foils and W cube.

At 10% modulation transfer factor, spatial frequencies, in terms of line pair per mm, were found to be the highest and the lowest for 3 mm and 5 cm thick tantalum foils, respectively, while the spatial frequencies of 6 mm thick Ta foil and 2.54 cm thick W cube were intermediate. Spatial resolutions (SR) in units of micrometer for 10% MTF, were calculated using the equation, SR(μm)=(1/(2 x Spatial Frequency (lp/mm))) x (1000 μm /1mm), and the error in SRs, which include the calculated average standard deviation of ~2 % in pixel grayscale value and the error caused by the alignment and the beam divergence

and not easily calculable, was estimated as 10 %. The SRs, as well as their errors, are provided in figure 46.

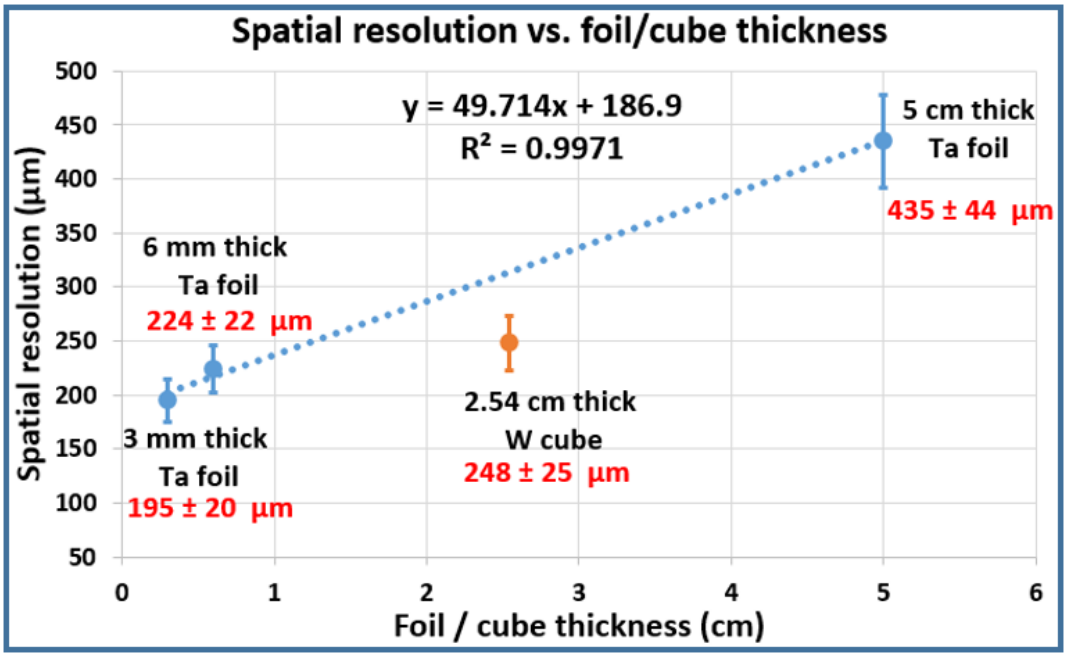

Figure 46: Spatial resolutions, with their errors, in µm, of Ta foils and W cube calculated from modulation transfer functions at 10 % MTF.

The spatial resolution degrades as the thickness of the imaging target increases. While the spatial resolution obtained with 3 mm thick Ta foil is the best, 5 cm thick Ta foil provides the worst spatial resolution, in the set. The poorest resolution for the thickest target is likely due to the effect of scattered neutrons from the imaging target even though it yields the highest contrast via neutron absorption. 6 mm thick Ta foil and 2.54 cm thick W cube may provide similar spatial resolutions when the 10 % error is considered.

There seems to be a linear relation between thickness and spatial resolution when three data points of Ta foils are considered. This linearity suggests that the 2.54 cm thick W cube would give better spatial resolution than the Ta foil with the same thickness. However, it can be seen in figure 47 that both W and Ta with thicknesses of 2.54 cm have very similar neutron scattering across the energies interested. Future work to collect data using Ta with thicknesses between 6 mm and 5 cm will be expected to reveal the accurate relation. The relation between neutron scattering and thickness can also be seen in Figure 47 which shows percentages of neutron absorption and scattering in the samples being used over a neutron energy range of 0.1 MeV to 2.0 MeV.

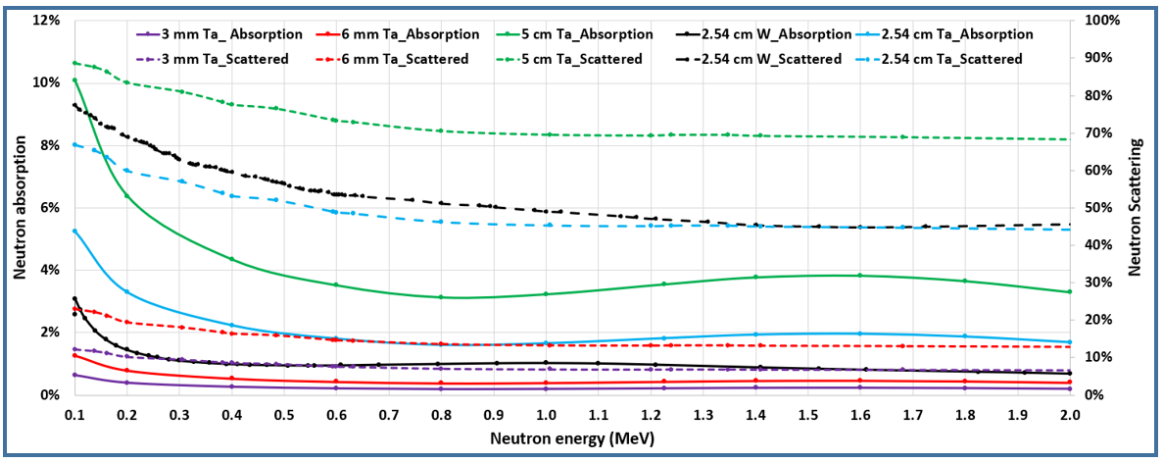

Figure 47: Neutron absorption and scattering in Ta foils and W cube spanning 0.1 – 2 MeV.

Neutron scattering is more prominent in all samples compared to absorption, and it increases with the thickness of the sample, which causes spatial resolution to deteriorate.

In Ta foils, it is easier to see in the 5 cm foil data, the ratio of scattering to absorption rises with increasing energy of neutron up to ~0.8 MeV (scattering/absorption ≈ 22.5 @ 0.8 MeV), however, it decreases after this point and reaches a local minimum at ~ 1.6 MeV (scattering/absorption ≈ 18).

5.3.3 Signal-to-Noise Ratio Investigation

White beam radiographs were collected using the new imaging station to explore the effect of the exposure time, the EM gain, and the median filter on Signal-to-Noise ratio. Table 12 summarizes the number of radiographs taken and the acquisition parameters.

Table 12: Radiographs obtained for SNR investigations, with exposure times and the EM gains.

3 EM	
Radiograph	Exposure (s)
1st	5
2nd	10
3rd	20
4th	30
5th	60
6th	90
7th	120
8th	180
9th	300
10th	600

10 EM	
Radiograph	Exposure (s)
1st	5
2nd	10
3rd	20
4th	30
5th	60
6th	90
7th	120
8th	180

20 EM	
Radiograph	Exposure (s)
1st	5
2nd	10
3rd	20
4th	30
5th	60
6th	90

30 EM	
Radiograph	Exposure (s)
1st	5
2nd	10
3rd	20
4th	30
5th	60

40 EM	
Radiograph	Exposure (s)
1st	5
2nd	10
3rd	20
4th	30
5th	60

50 EM	
Radiograph	Exposure (s)
1st	5
2nd	10
3rd	20
4th	30
5th	60

Some of the raw radiographs acquired were given in figure 48, with the acquisition parameters seen on each radiograph's top left. For each raw radiograph, the mean gray value of the area surrounded by the red circle was obtained, and the sample standard deviation of each mean value was calculated. Both mean gray values and sample standard deviation are provided in each radiograph's lower left.

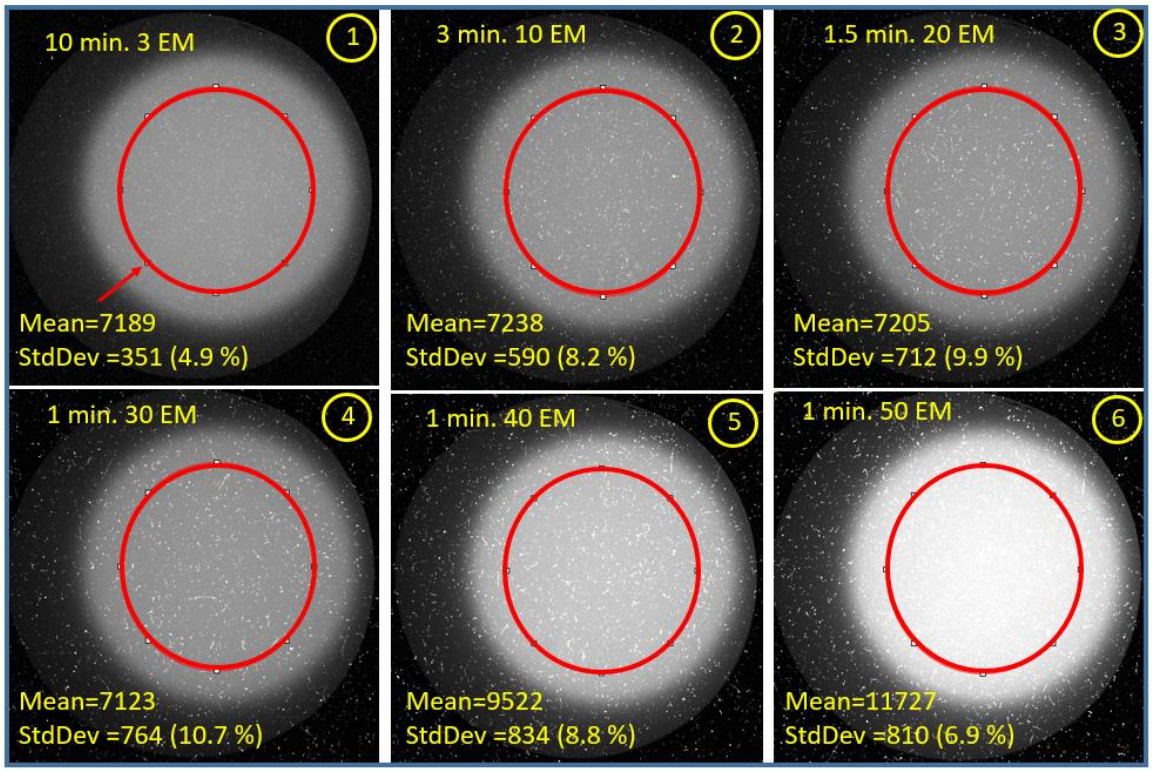

Figure 48: Raw radiographs obtained with various exposure times and EM gains, along with the calculated mean gray values, and population standard deviations.

Radiographs 1, 2, 3, and 4 provided similar mean gray value even though the exposure time decreases since the increasing EM gain yielded electron amplification that compensated the decreasing integration time. Radiographs 4 and 5 yielded higher mean gray values since higher EM gains, and between them, 5 provided the highest because the higher EM gain. Radiograph 1 yielded the lowest standard deviation (4.9 %) due to possibly the lowest amplification of the background noise. However, the second lowest standard deviation (6.9 %) was obtained with radiograph 6, with the likely reason of having

the highest mean gray value. SNRs of all the raw radiographs were calculated by dividing the mean gray value to standard deviation, and they are reported in figure 49.

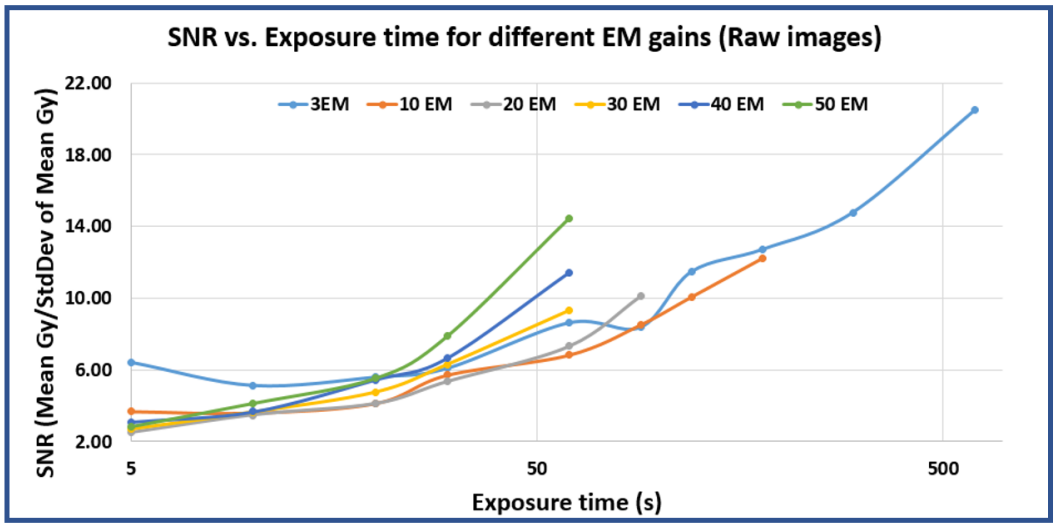

Figure 49: Signal-to-Noise ratios of radiographs.

Results show that SNR increases with increasing exposure time and EM gain. At exposure times between 5 and 30 seconds, it seems that the effect of EM gain on SNR is negligible. As the exposure time increases beyond 50 seconds, SNR changes more dramatically with increasing EM gain.

The radiographs seen in figure 48 were then applied 3-pixel median filter to remove noise, and the same procedure was followed as done for the radiographs given in figure 48 to calculate the mean gray values and the sample standard deviations. Figure 50 shows the

processed radiographs, with the mean gray values and their sample standard deviations of the areas in the red circles.

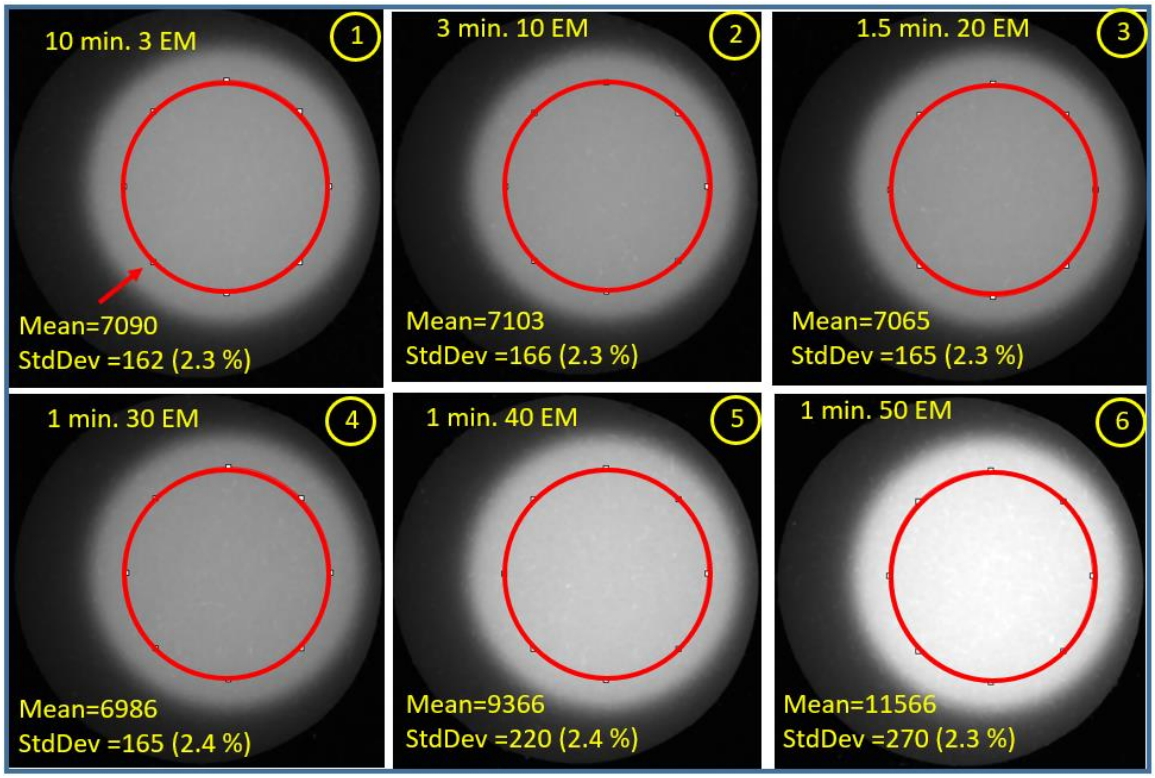

Figure 50: 3-pixel median filter applied radiographs, with the mean gray values and the sample standard deviations.

Applying median filter to radiographs kept the mean gray values similar to those of raw radiographs while reduced the sample standard deviations dramatically due to the smoother gray value distribution. In all six radiographs, median filter caused almost the same

standard deviation of 2.3%. SNRs of all processed radiographs with respect the exposure time for different EM gains are provided in figure 51.

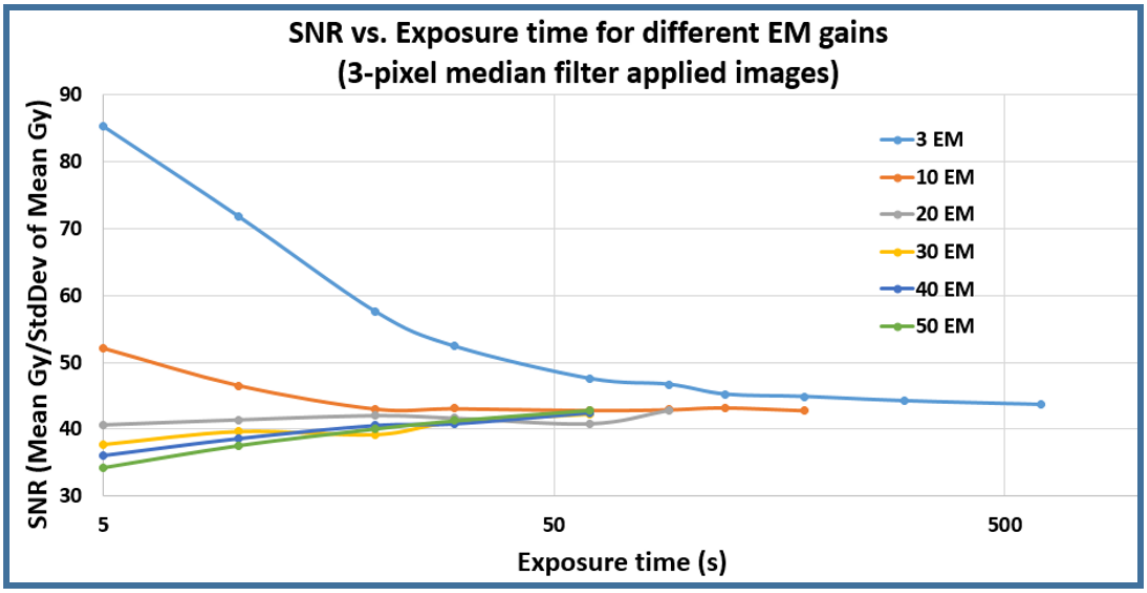

Figure 51: SNRs of the processed radiographs with respect to the exposure time for various EM gains.

When compared to the SNRs calculated from the raw images, applying median filter increased the SNR in all radiographs. For 3 EM and 10 EM, the SNR decreases rapidly with increasing exposure time while the SNRs calculated from the radiographs taken with 20 EM, 30 EM, 40 EM, and 50 EM seem to be almost independent of increasing exposure time. Independent of the EM gain, the SNRs converge to ~45 around 1 minute of exposure time.

5.4 Conclusion

In this study, the effect of imaging target thickness on the spatial resolution was investigated at a reactor-based fast neutron beam facility using the knife-edge method. Experiments were also conducted to determine the beam divergence, found to be a parallel beam with a divergence of ~0.6°. Knife-edge radiographs of 3 mm, 6 mm, and 5 cm Tantalum foils, and a 2.54 cm Tungsten cube were obtained, and MTF were generated. Unlike thermal or cold neutron imaging, where a thicker absorber does not drastically degrade the spatial resolution, the 10% MTF value, in μm, with tested targets are much higher (worse resolution) as a function of increasing thickness. Although the W cube is a different material than Ta foil, it provided a spatial resolution following the trend of the thickness-spatial resolution relation. SRIM simulations and calculations showed that 2 MeV neutrons, impinging on the PVT medium perpendicularly, set a limit (44 um) on the spatial resolution, and this limit increased when neutrons deviated from normal incidence. Signal-to-Noise Ratio investigation yielded that the applying median filter to radiographs increases SNR, and the SNR does not increase for exposure times beyond 1 minute, regardless of EM gain. This study may pave the way for future studies on standardizing fast neutron spatial resolution measurements and enabling quantification for fast neutron screen development.

Chapter 6. Fast Neutron Computed Tomography of Multi-Material Complex Objects

6.1 Introduction

Fast neutron computed tomography (nCT) was investigated using various imaging phantoms made of materials of different atomic number (Z). Some of the important objectives of this study are to demonstrate a high-throughput nCT data acquisition at a low power research reactor, and to show the capability of fast nCT in resolving minute features in low-z material while being shielded by high-Z materials. In this study, fast nCT was accomplished using two different imaging system.

6.2 Experimental

6.2.1 Neutron Beam Facility and Imaging Systems

The neutron source utilized in this work is the 500-kWth Ohio State University Research Reactor (OSURR)'s recently built fast neutron beam facility which supplies a well-collimated, high-flux neutron beam at the beam exit.

Image acquisition was performed using a lens-coupled imaging system, consisting of an Electron Multiplying (EM) CCD camera cooled down to -69 °C with the help water circulation and Thermoelectric Peltier feature to decrease thermal noise, a light-tight enclosure, and a front surface mirror. A high light-yield (HiLY), 1 cm thick PVT

scintillator, seen in figure 1, with edges and backside blackened to minimize background optical scatter and prevent degradation in spatial resolution was provided by LLNL and used as the neutron imager. The object assembly is placed onto an XYZ linear stage to fine tune the object alignment. Also, a rotational stage was employed to acquire radiographs of phantoms at different angles. During data acquisition, phantoms were positioned on an Ethafoam-400 (low density foam, 0.064 g/cm^3) holder to minimize scattered neutrons caused by the holder itself, which is important since part of the holder is in the beam. Figure 52 shows a photo and a schematic diagram of the image acquisition configuration.

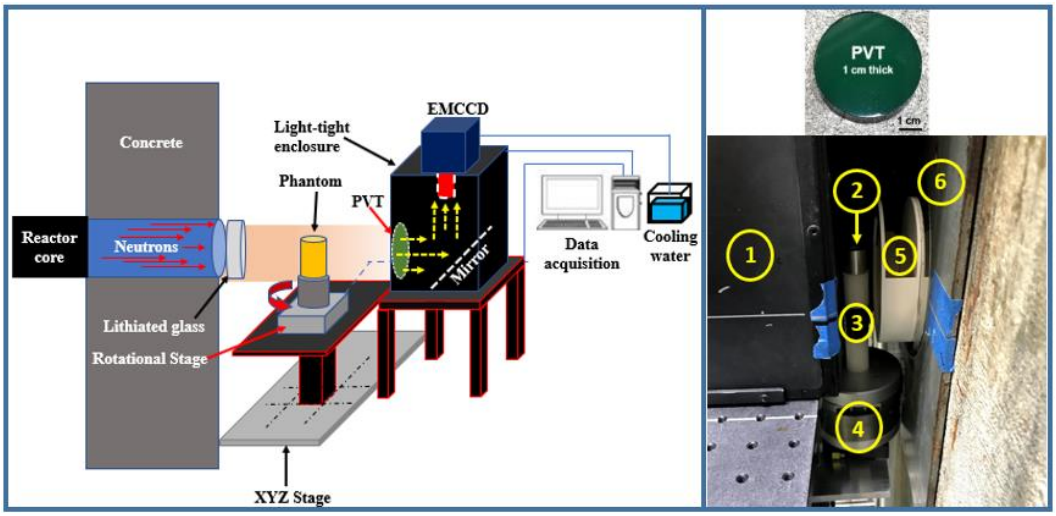

Figure 52: A schematic drawing of the image acquisition configuration (left) showing the neutrons coming through a collimator embedded in the reactor biological shielding wall and a photo of the image acquisition configuration (right) where neutrons are incident from the right side; 1- Light-tight enclosure, 2- Imaging phantom, 3- Ethafoam holder, 4- Rotation stage, 5- Lithiated glass filter, and 6- Reactor wall, and HiLY scintillator (top-

right). The body of the EMCCD is outside the light-tight box in this setup and collects scintillation lights reflected upward by the mirror.

The EMCCD camera utilized in this study was in a constant neutron and gamma-ray radiation field, and especially the backscattering of neutrons and gamma-rays from the beam stop was the main contributor to this field. Therefore, the EMCCD was shielded in an upgraded imaging station to minimize the radiation incidents on the CCD chip, which would yield fewer blooming and smear on the radiographs hence improve the improve the image quality. Fast nCT was also conducted using this new imaging station and new imaging phantoms. Figure 53 provides a depiction of the upgraded imaging system, a photo of the experiment setup, and the scintillator utilized.

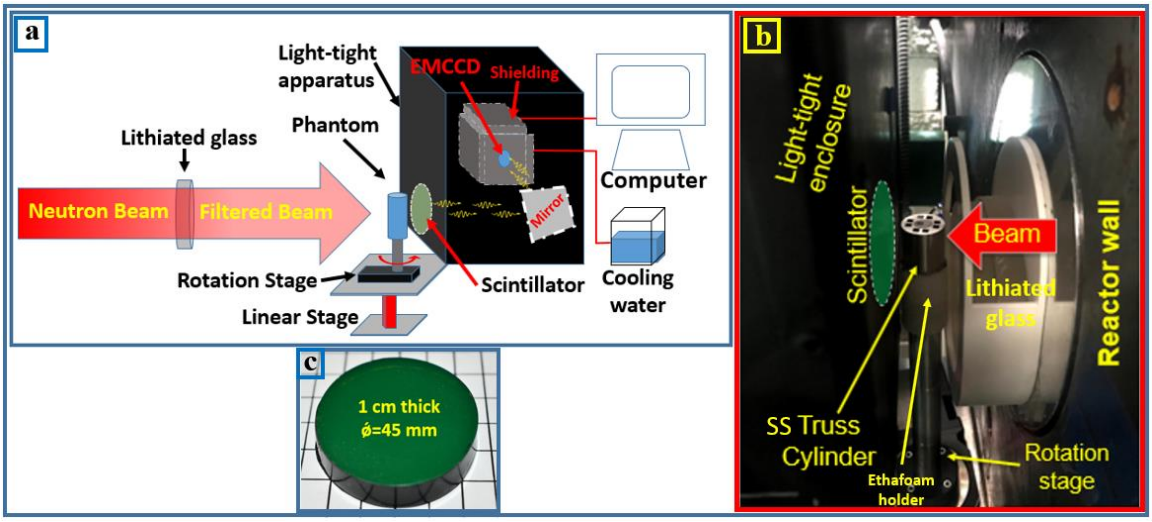

Figure 53: A Schematic (a) and photograph (b) of the experimental configuration, and 1 cm thick HiLY PVT scintillator employed (c). The EMCCD is enclosed inside the light-tight apparatus and collects scintillation lights reflected to the side way by the mirror.

6.2.2 Imaging Phantoms

The nCT study employed several multi-material objects: a ball phantom, a shielded phantom referred to here as the OSU phantom, and an additively manufactured Ti64 titanium alloy (90 % Titanium, 6 % Aluminum, and 4 % Vanadium) truss cylinder, all supplied by LLNL. The two cylindrical ball phantoms are made of High-Density Polyethylene (HDPE, density= ~0.95 g/cm^3) with a height and diameter of 2.2 cm to form the base. Both of these have three tungsten carbide (WC, density=15.63 g/cm^3) balls of either 2-mm or 5-mm diameter attached to their cylindrical surfaces and grooved ~3.5 mm diameter drilled holes along their rotation axis. The cylindrical OSU phantom, with diameter and height of 2.2 cm, is a coaxially-nested three-layered phantom, made of HDPE, tungsten, and aluminum, each with grooves. The aluminum cylinder has two

circumferential grooves cut into the inner face of the tube with differing depth. The tungsten cylinder also has two circumferential grooves with differing depths, but these are on the outer face of the cylinder. There are four different 1-cm diameter HDPE cylindrical inserts with different features on each. The “HDPE#1” insert has five horizontally-drilled holes, 0.200 cm, 0.150 cm, 0.100 cm, 0.050 cm, and 0.025 cm in diameter, with corresponding depths. The “HDPE#2” insert has two horizontally-drilled holes, 0.300 cm, and 0.050 cm in diameter, again with corresponding depths. The “HDPE#3” insert does not have any drilled holes, but instead has symmetric grooves around the Z (rotational) axis. The “HDPE#4” insert has one vertically-drilled through hole with a diameter of 0.300 cm, and another vertically-drilled hole with a diameter and 0.050 cm and a depth of 0.380 cm. The locations of the drilled and through holes on HDPE#1, HDPE#2, and HDPE#4 make them asymmetric around the rotational axis. The additively-manufactured truss cylinder has a diameter of 2 cm and a height of 4 cm. It has an embedded fine lattice structure, with features as small as 200 μm. Figure 54 shows the phantoms. Table 13 shows macroscopic cross-sections (Σ) of 2 MeV neutrons with elements/materials comprising the phantoms, as well as thicknesses of the elements/materials that attenuate the 2-MeV neutron flux to ~10 % of its original intensity.

Table 13: Macroscopic cross-sections (Xs) (Σ) of 2 MeV neutrons with elements/materials comprising the phantoms and the thicknesses that reduce the flux to 10 % of its original intensity.

Element / Material	Macroscopic Xs (Σ) @ 2 MeV (1/cm)	Thickness to attenuate the 2-MeV flux to 10 % (cm)
Aluminum	0.195	11.81
Titanium	0.226	10.19
Tungsten	0.446	5.16
HDPE	0.303	7.60
Tungsten Carbide	0.417	5.52

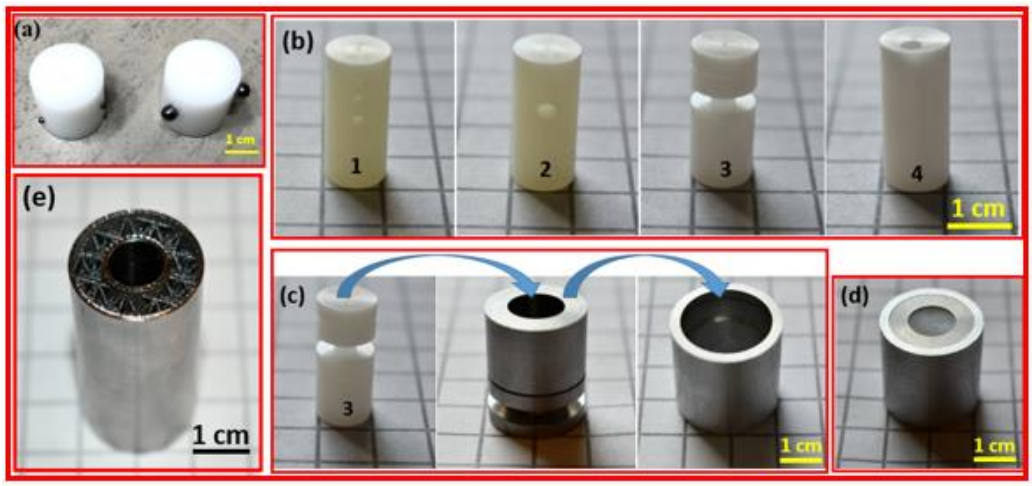

Figure 54: The two Ball phantoms shown in (a) have either a 2 mm tungsten carbide ball (left) or 5 mm tungsten carbide ball (right) attached to the HDPE surface. The four HDPE inserts of the OSU phantom are shown in (b). Three parts of the HDPE#3 with insert (left), W (middle), and Al (right) layers are shown in (c). A fully assembled OSU

phantom with Al, W layers, and HDPE#3 insert are shown in (d). The truss cylinder is shown in (e).

Additionally, two more multi-material phantoms were employed. The first phantom is a stainless steel (SS) truss cylinder with a diameter and height of 2.2 cm, with vertical rectangular through holes (W x D = 3 x 3 mm^2) as well as a vertical cylindrical drilled hole (Dia. =1 cm, H=1.1 cm). There are also two High-Density Polyethylene (HDPE) inserts. The first is a cylinder with four horizontal through holes with diameters of 0.5, 1, 2, and 3 mm, as well as a vertical rectangular through hole with dimensions of W x D x H = 3 mm x 3 mm x 1.1 cm. The second insert is a solid HDPE parallelepiped fitted to the through hole. Both inserts are transition fit inside the truss cylinder phantom. The second "MAS" phantom is a spherical shell (Diameter ~2.2 cm) made of lead-antimony (PbSb) alloy (94 % Pb and 6 % Sb) with intricate internal grooved structures. The phantom can be separated into two semi-spherical shells. A cylindrical HDPE insert, featuring four horizontal through holes with diameters of 0.5, 1, 2, and 3 mm, can be placed inside it. Figure 55 shows the phantoms and their respective HDPE inserts.

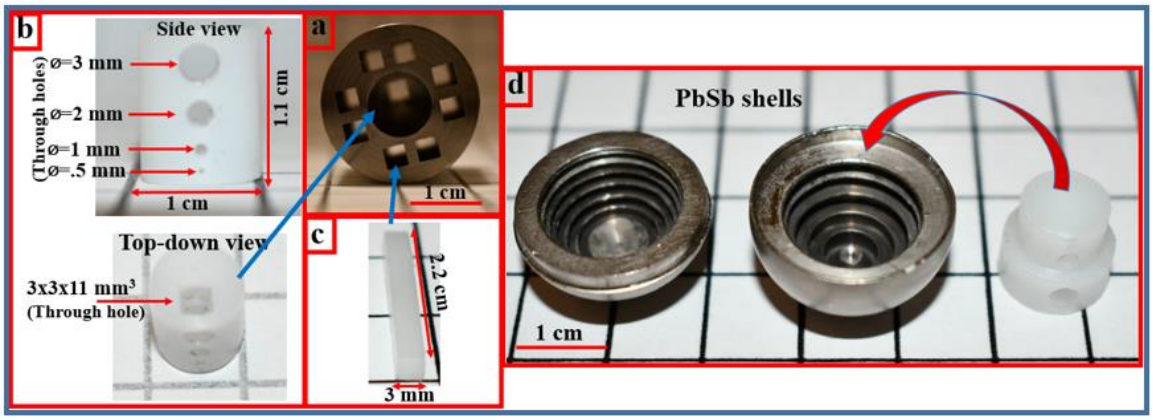

Figure 55: (a) SS truss cylinder phantom's top-down view (b) HDPE inserts - side and top-down of (b) cylindrical and (c) rectangular plug views. (d) The MAS phantom is composed of two hemispherical shells (left – middle) with interior grooves and an HDPE insert (right).

6.3 Results and Discussion

6.3.1 Ball Phantoms

Radiographs of each ball phantom were acquired with an exposure time of 40 seconds while the reactor was in operation at a power of 250 kW. The old imaging system was employed in this data acquisition. Table 14 provides the number of radiographs acquired, the rotation spans, and the nCT data acquisition time for each Ball phantom.

Table 14: Collected nCT data information for the Ball phantoms.

Tungsten Carbide Ball diameter	Rotation	Number of radiographs	Total acquisition time (min)
2 mm	Full (0-360°)	240	160
5 mm	Full (0-360°)	120	80

Although the HDPE component, which the base structure, of the ball phantoms is symmetric around the rotation axis, the WC balls attached to the cylindrical surface make the phantoms asymmetric. Therefore, radiographs of the ball phantoms were taken from 0° to 360°. The required times to collect all the radiographs used for reconstruction of the 3D volume of the 2 mm ball phantom and the 5 mm ball phantom were ~2.67 hours and ~1.33 hours, respectively. All radiographs were post-processed using a median filter of 3 pixels to remove "salt and pepper" or "impulse noise" noise, which causes black and white pixels and originating from the abrupt change in the image signal [74]. Then, each radiograph was reviewed for the presence of blooming effects and smear caused by the interaction of neutrons and gamma-rays with the Si-based imaging sensor in the camera [73]. Blooming occurs when excess electrons in a pixel cause saturation and start filling adjacent pixels. Smear features appear as white streaks on images caused by the camera reading out those saturated pixels. These features were carefully removed using a tuned median filter with different pixel values determined based on the level of saturation and the number of pixels affected by saturation. After post-processing, radiographs were uploaded into Octopus Reconstruction software to create reconstructed 3D volumes. Figure 56 shows one of the post-processed radiographs and the volume-rendered 3D images of each ball phantom.

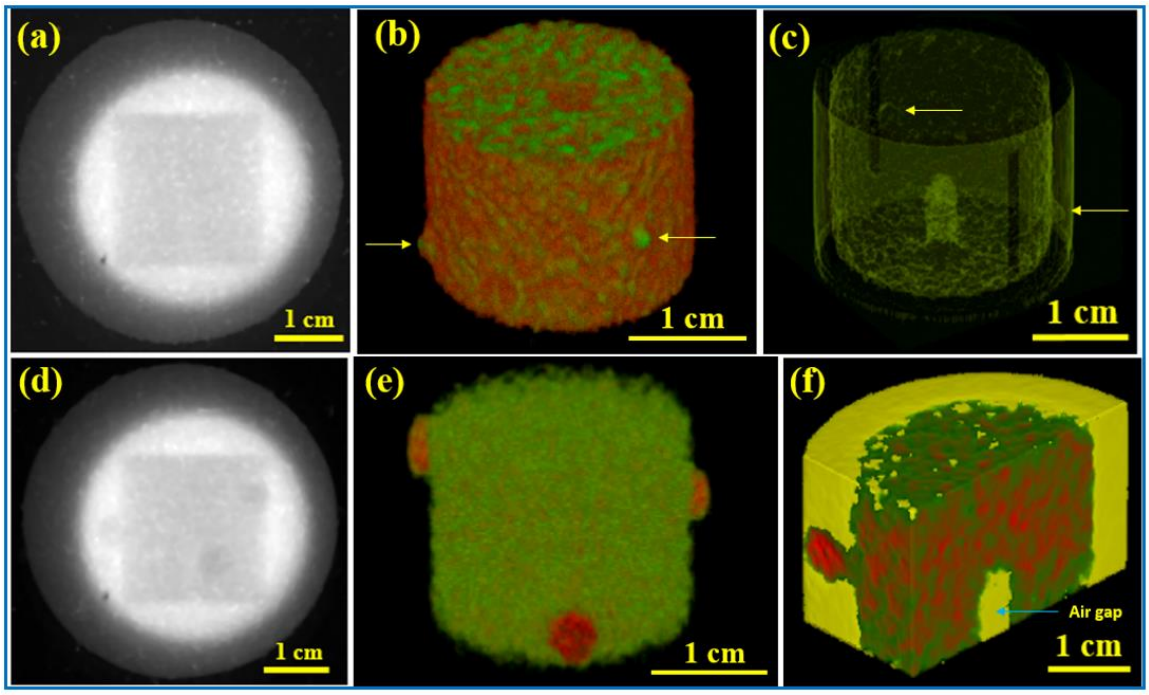

Figure 56: Radiographs (a), (d) and reconstructed 3D images (b) and (c), and (e) and (f) of 2 mm and 5 mm tungsten carbide (WC) ball phantom, respectively.

Results show that although the 2-mm tungsten carbide balls are not seen on the radiograph 56(a), they become discernable in the 3D reconstructed images 56(b) and 56(c), and are indicated by yellow arrows. Good contrast between 5-mm WC balls and HDPE is seen on the radiograph 56(d), and on the 3D images 56(e) and 56(f). On the 56(e) and 56(f) images, the HDPE, 5 mm WC balls, and air are false-colored as green, red, and yellow, respectively. In image 56(f), the red parts inside the green HDPE cylinder are artifacts caused by reconstruction. The volume rendered images 56(c) and 56(f) also reveal the grooved drilled central hole on both phantoms.

6.3.2 OSU phantom

Radiographs of the OSU phantom with each HDPE insert were acquired with varying exposure times and reactor powers while the EMCCD EM gain was kept low to obtain high dynamic range, as well as to prevent the amplification in the noise level. The exposure time and reactor power for each configuration are given in table 15. Table 16 provides the rotation span, the number of radiographs collected, and the total acquisition time for each OSU phantom configuration. The old imaging system was utilized to collect these nCT data sets.

Table 15: Image acquisition parameters for the OSU phantom configurations.

HDPE inserts	Exposure Time (s)	Reactor Power (%)
Config1	20	50
Config2	25	50
Config3	50	25
Config4	25	50

Table 16: Collected nCT data information of the OSU phantom.

HDPE inserts	Rotation	Number of radiographs	Total acquisition time (min)
Config1	Full (0°-360°)	360	120
Config2	Full (0°-360°)	240	100
Config3	Half (0°-180°)	180	150
Config4	Full (0°-360°)	240	100

Tomography data for “Config1”, “Config2”, and “Config4” as defined in table 16 was collected with 1.5° increments from 0° to 360°, while Config3 data were acquired with 1° increments from 0° to 180°. Although the number of radiographs collected for Config1, Config2, and Config4 is higher than that of Config3, the reactor power was doubled yielding a higher neutron flux impinging on the phantom and the scintillator. Due to the increased flux, the total data acquisition time dropped from 2.5 hours for Config3 to ~1.67 hours for Config2 and Config4. The same image post-processing and 3D reconstruction procedures were applied for radiographs of the OSU phantom as for the ball phantoms. Figures 57, 58, 59, and 61 provide a representative radiographs and 3D reconstructed images of Config1, Config2, Config3, and Config4, respectively.

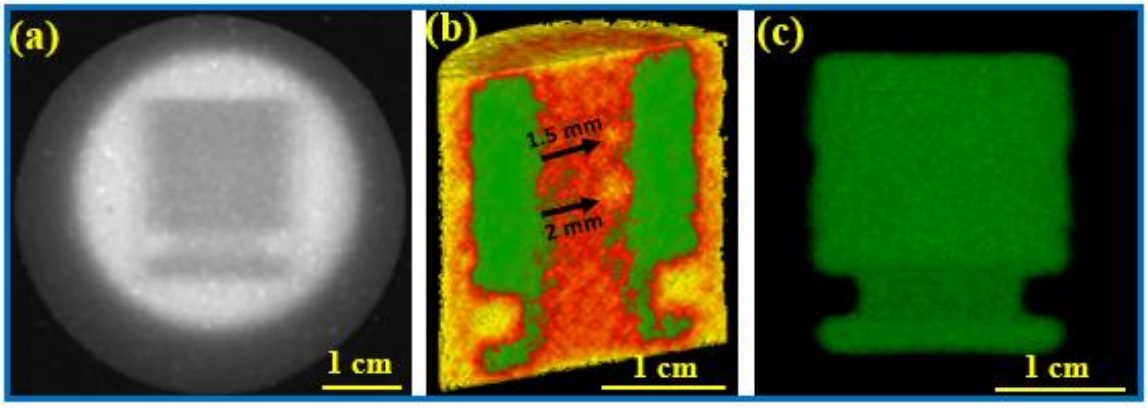

Figure 57: Radiograph (a), cross sectional view (b) and W layer (c) of 3D reconstructed image of Config1 of the OSU phantom.

On radiograph 57(a), it is not possible to see the drilled holes of HDPE#1. However, the cross-sectional view 57(b) from the reconstructed nCT data reveals 1.5 mm and 2mm drilled holes as yellow spots in the red (HDPE) region between green (tungsten) regions, as indicated with black arrows and labels “1.5 mm” and “2 mm” respectively.

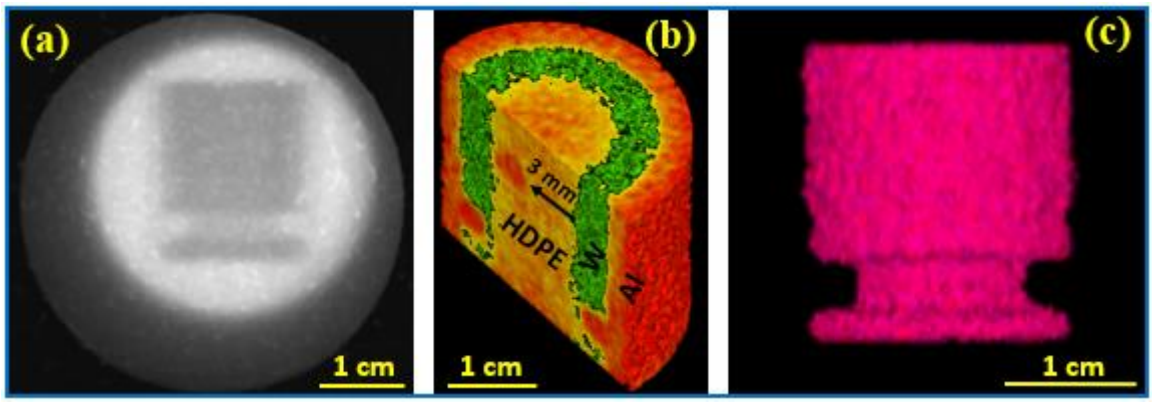

Figure 58: Radiograph (a), cross sectional view (b) and W layer (c) of 3D reconstructed image of Config2 of the OSU phantom.

On radiograph 58(a), the tungsten (W) layer is visible, while HDPE#2, hidden behind the W and Al layers, is not seen. However, the Al (red) and W (green) layers, HDPE#2 insert (yellow) and the drilled hole (red, indicated with black arrow and “3 mm” layer) are distinguishable in the cross section of the 3D reconstructed volume 58(b).

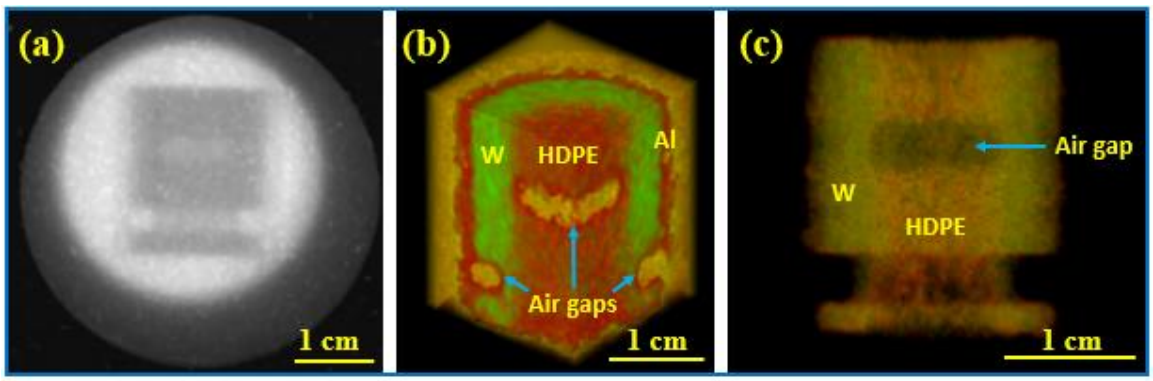

Figure 59: Radiograph (a), cross sectional view (b) and W layer (c) of 3D reconstructed image of Config3 of the OSU phantom.

In addition to the tungsten (W) layer being visible on the radiograph 59(a), the air gap created by the grooved structure in HDPE#3 is also discernable. The air gap (yellow), HDPE#3 (red), tungsten (green), and aluminum (red) layers are clearly visible on the cross-sectional view of the 3D reconstructed image 59(b). Another volume-rendered image 59(c) reveals the W layer, HDPE#3, and the air gap.

One of the experimentally-acquired radiographs employed to reconstruct the 3D image of Config3 was gray value-inverted as seen in figure 60(a), and a line profile, given in figure 60(b), of the yellow region, seen in figure 60(a), was created. On the line profile plot, the aluminum and tungsten layers, the HDPE#3 insert, and the internal air gaps can be revealed, while the small grooves in the tungsten and aluminum cannot be discernable mainly due to resolution-degrading factors such as scattered neutrons, gamma rays from the environment, optical scatter in the scintillator, and electronic noise in the camera.

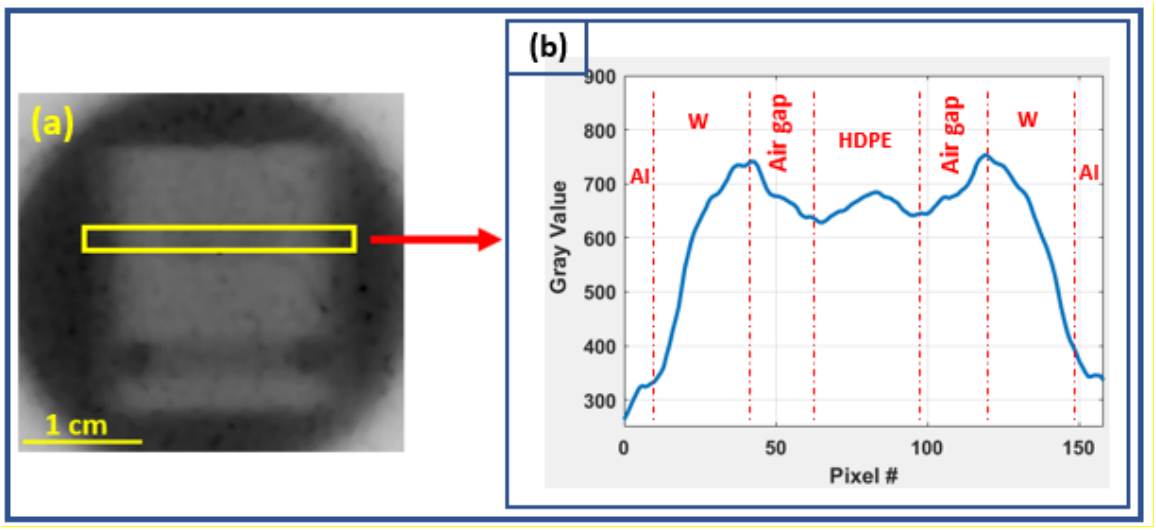

Figure 60: Experimentally obtained radiograph (a) and a line profile of the experimental radiograph (b), also showing the contrast differences between different compositions.

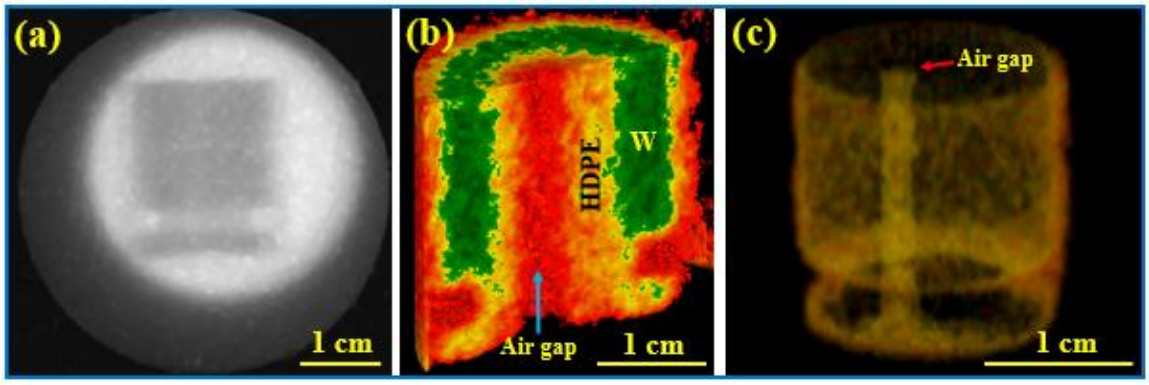

Figure 61: Radiograph (a), cross sectional view (b) and W layer (c) of 3D reconstructed image of Config4 of the OSU phantom.

On radiograph 61(a), the through-hole, which creates an air gap, in the HDPE#4 is almost undetectable. However, the cross-sectional view of the 3D reconstructed image 61(b) reveals the through-hole (red) (indicated by blue arrow) as well as HDPE#4 (yellow) and

the W layer (green). Image 61(c) clearly shows the through hole (shown by red arrow) and W layer.

Fast nCT data sets of the Config1 and Config2 of the OSU phantom were collected employing the new imaging station as well. Figures 62 and 63 provide results of Config1 and Config2, respectively.

In collecting nCT data of Config1, instead of one radiograph for each angle, two radiographs per angle were collected. The purpose of this procedure was to increase the signal-to-noise ratio by averaging two radiographs. The exposure time was 60 seconds while the EM gain of the camera was set to 20. Radiographs were collected through full 0° to 360° rotation. Figure 62 shows a radiograph obtained by averaging two radiographs taken at the same angle and then by applying a median filter of 3-pixel radius, and a 3D reconstructed image of Config1, as well as the line profile of a region, where the holes are in the HDPE are, on the 3D image.

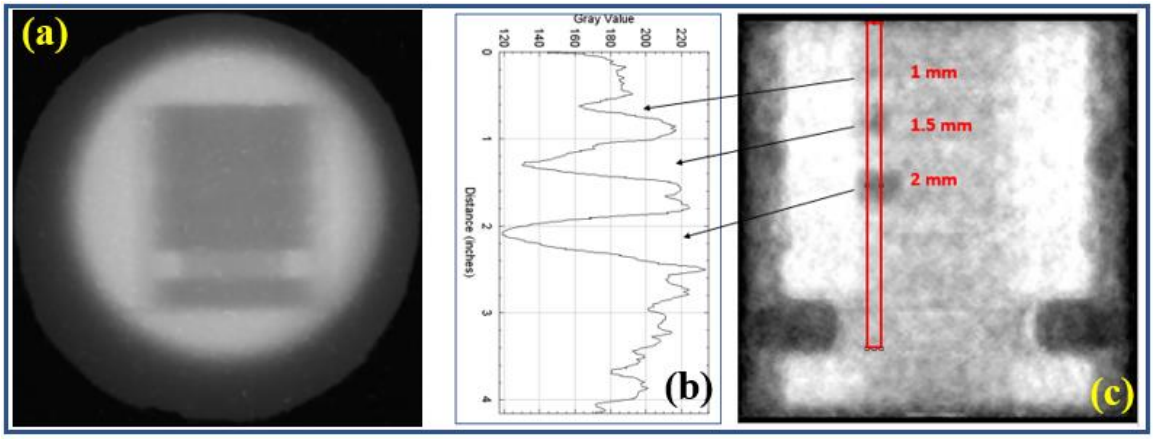

Figure 62: Post-processed radiograph (two radiographs were averaged and then median filter applied) (a) and a 3D reconstructed image (c) of Config1 of the OSU phantom, respectively. A line profile of the region shown by the red rectangle on 3 D reconstructed image (c).

The new imaging station and the procedure of averaging the radiographs yielded radiographs with better contrast as seen on radiograph 62(a) in which, in addition to the W layer, the Al shell is also clearly seen. Nevertheless, not enough contrast between the materials causes the HDPE insert still not to be visible. The air gaps' volumes created by the drilled holes in the HDPE insert may not be big enough to provide a sufficient neutron absorption difference between air and HDPE, which may be the reason why none of the holes is revealed on radiograph 62(a). However, 3D reconstructed image 62(c) is able to provide the information about the 1-, 1.5-, and 2-mm holes since it contains all the information in 720 radiographs, not just the information in 2 radiographs as in the case of image 62(a). Additionally, the HDPE insert is distinguishable in 62(c). The line profile

provides somewhat quantitative information about the contrasts between each individual hole and the HDPE insert, as well as the contrasts amongst the holes.

The nCT data of Config2 were collected with the same image acquisition parameters as the one of Config1, and again, two radiographs per degree from 0° - to 360° were collected, with a total number of radiographs of 720. Figure 63 provides a radiograph obtained by averaging two radiographs taken at the same degree and then by applying a median filter of 3-pixel radius and a 3D reconstructed image of Config2, respectively.

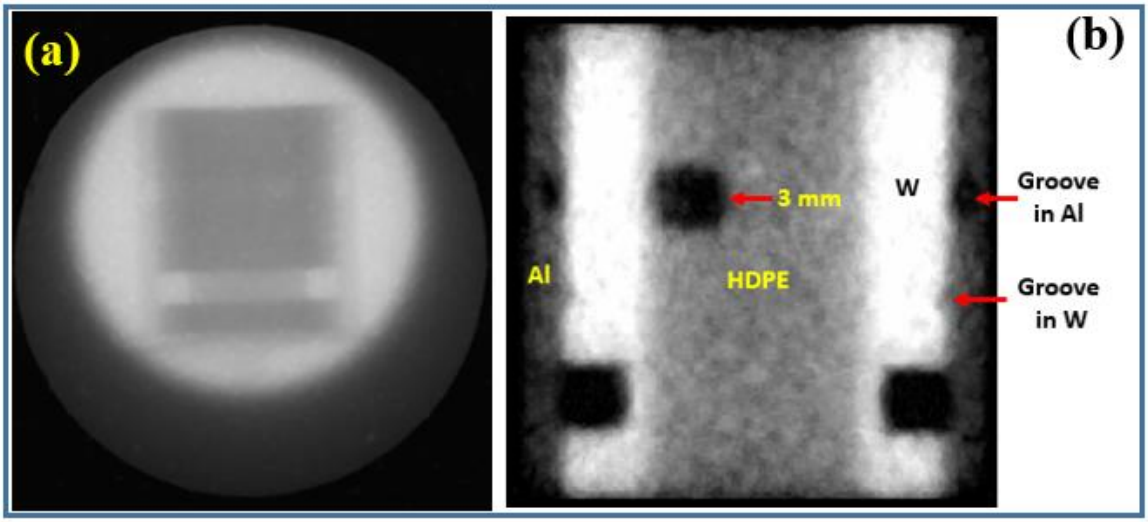

Figure 63: Post-processed radiograph (a) and a 3D reconstructed image (b) of Config2 of the OSU phantom.

Radiograph 58(a), acquired with the old imaging system and one radiograph per angle scheme, does not provide any information about the groove structure in the Al shell and the 3 mm hole in HDPE, however, they are distinguishable on radiograph 63(a). On 3D

reconstructed image, 63(b), each layer (Al, W, and HDPE), and groove features in Al and W were revealed. The reconstructed image also yielded a much sharper 3 mm hole compared to what the old system provided.

6.3.3 Ti64 Truss Cylinder

Radiographs of the truss cylinder were acquired with an exposure time of 25 seconds utilizing the old imaging system. The same post-processing and the 3D reconstruction scheme were applied as for the other phantoms. Figure 64 shows one of the radiographs obtained and 3D reconstructed images of the truss cylinder. Table 17 provides the rotation span, the number of radiographs collected, and the total acquisition time for this cylinder.

Table 17: Collected nCT data information of Truss cylinder.

Truss Cylinder	Rotation	Number of radiographs	Acquisition time (min)
2-cm dia.	Full (0°-360°)	360	150

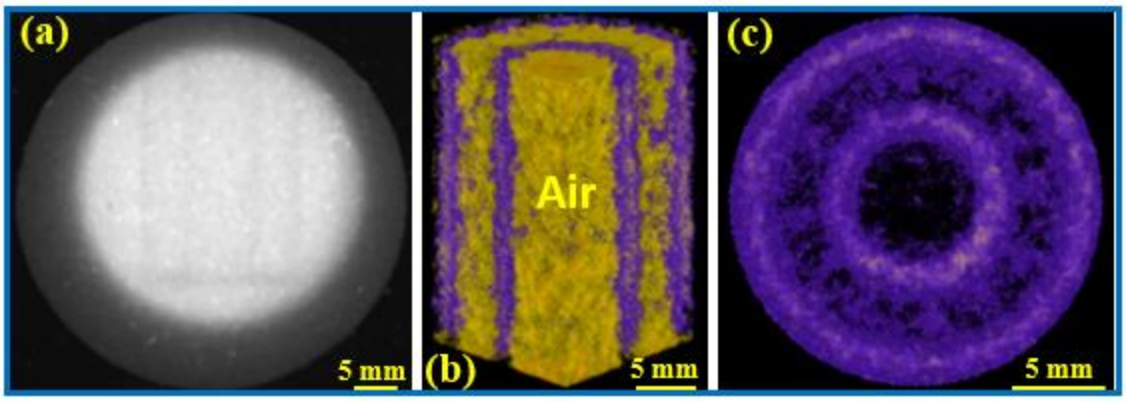

Figure 64: Radiograph (a), cross sectional view (b) and top-down view (c) of 3D reconstructed image of truss cylinder.

Radiograph 64(a) shows only the relatively-thick cylindrical structure, but not the fine structures located inside the truss cylinder. These two cylindrical structures can also be seen in the volume-rendered image 64(b) as purple lines, while the fine structures are still not resolved. However, in the yellow region (air) between the inner and outer cylinders, there are purple features, representing the fine titanium trusses, as compared to the void region inside the inner cylinder. On the other hand, a top-down view of the 3D reconstructed image 64(c) reveals a periodic repeating structure, which provides some limited information about the truss.

Another set of fast nCT data of truss cylinder phantom was collected using the new imaging station. To decrease the effective pixel size and hence increase the spatial resolution of the system, a 2X c-mount fixed focal length lens extender was integrated into the system. Figure 65 shows photos of the focal length extender, 50-mm fixed focal length lens to which the focal length extender is connected, and the lens/focal length extender system that

is attached to the EMCCD camera. With this apparatus having been added to the system, the effective pixel size dropped to ~65 μm from ~104 μm.

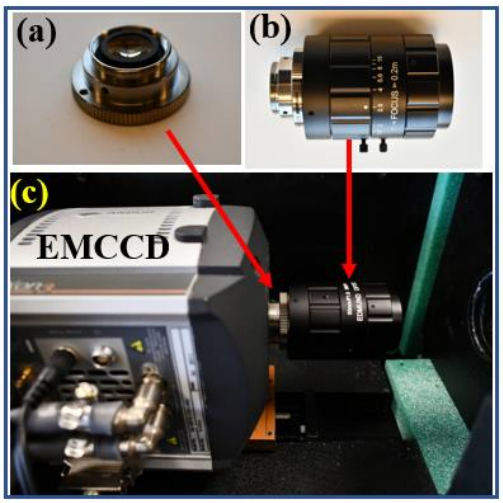

Figure 65: 2X fixed focal length extender (a), 50-mm fixed focal length lens with the focal length extender attached (b), and lens/focal length extender system connected to EMCCD camera.

The image acquisition parameters in this run were selected as; the exposure time per radiograph was 60 seconds, the EM gain was 20, and the total number of radiographs collected (one radiograph per degree, from 0° to 360° with 1° intervals) was 360. Figure 66 shows a post-processed (3-pixel median filter applied) radiograph and 3D reconstructed images of truss cylinder.

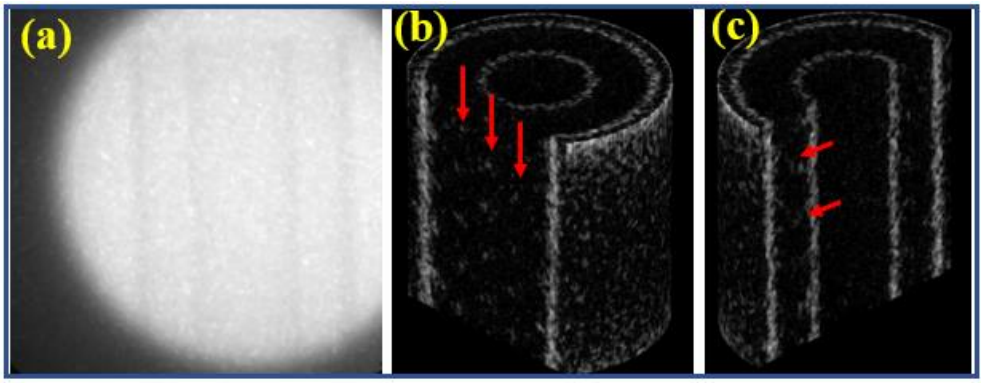

Figure 66: Post-processed radiograph (a), 3D reconstructed images (b and c) of truss cylinder.

The field of view (FOV) on radiograph 66(a) is smaller than that of radiograph 64(a) due to the decrease in the effective pixel size, which is why the beam cannot be imaged fully on radiograph 66(a). (Radiographs were not cropped and the pixel size on both radiographs 64(a) and 66(a) are 512x512). On radiograph 66(a), only inner and outer cylindrical structures of the truss cylinder are visible, and no information about the truss structure between these cylinders can be reached. However, 3D reconstruction reveals some sort of vertical repeating structures that can be attributed to the junctions, shown by red arrows seen in image 66(b), and very faint features, shown by red arrows seen in image 66(c), that can be ascribed to the connections between junctions. Overall, the new imaging station, with a smaller effective pixel size feature included, provided somewhat better nCT data as some internal truss structures can be revealed.

6.3.4 Voxel Resolution in Old Imaging System

To help determine the resolution limits in the old imaging system, two methods were applied and compared. First, the voxel size of the imaging system was determined through the effective pixel size of the radiographs. The effective pixel size was calculated by taking the known scintillator radius (45.5 mm) and dividing that value by the number of pixels that fit in that circle. In this case, in ImageJ, the number of pixels that fit in this circle was determined to be 347 ± 5, yielding an effective pixel size of 0.131 ± 0.002 mm. The final variable in determining voxel size is the slice thickness which was an output from Octopus and is 0.131mm as well. Therefore, the voxel size of this system is a cube with side lengths 0.131 ± 0.002 mm. Another resolution limit comes from the Nyquist angular sampling given by $(\pi/2) \times$ (Object thickness/Number of Projections). For example, the OSU phantom has a thickness of 22 mm. Therefore, the resolution limits for the different configurations depend on the number of projections. As shown in table 18, when the number of projections increases, the limit decreases. This limit is useful to determine how many images are needed to effectively render a volume via CT reconstruction. The spatial resolution of features in nCT images also degrades monotonically with the distance between the feature and the axis of rotation. The values given here are for the outer edge of the object.

Table 18: Nyquist angular resolution limit of OSU phantom with respect to number of radiographs.

HDPE inserts	Number of radiographs	Resolution Limit (mm)
Config1	360	0.0960
Config2	240	0.144
Config3	180	0.192
Config4	240	0.144

6.3.5 Stainless Steel (SS) Truss Cylinder

Two sets of radiographs of this phantom were collected employing the old imaging system; (Config# 1) radiographs of the truss cylinder alone, and (Config# 2) radiographs of the truss cylinder with the HDPE cylindrical and rectangular bar inserted. The exposure time per radiograph in the first and second sets were 15 and 14 seconds, respectively, while the reactor power was at 90%. The number of projections collected was 360 for each set, and the total nCT data acquisition times were 1.5 and 1.4 hours for the first and second sets, respectively. Figure 67 and 68 shows a sample radiograph and 3D rendered image of Config#1 and Confi#2, respectively.

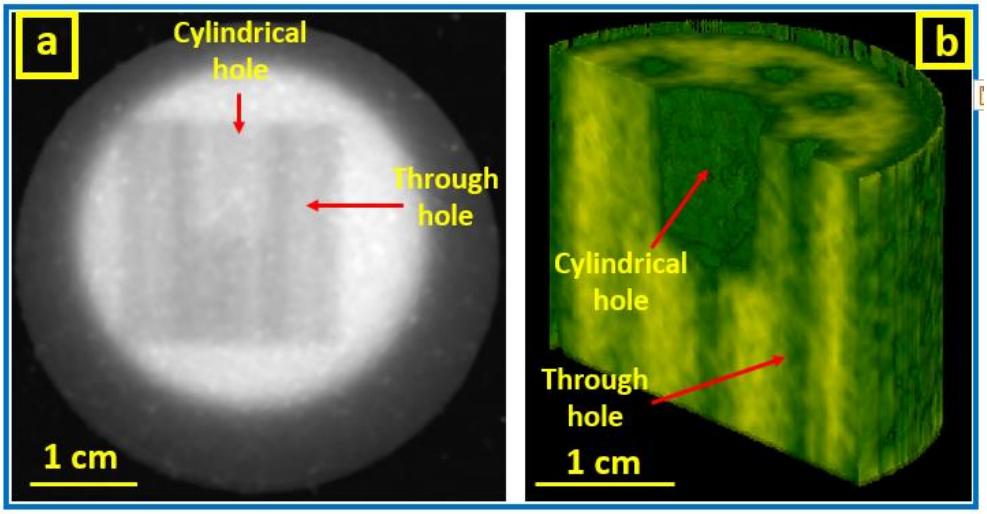

Figure 67: Radiograph of the truss cylinder (no inserts placed) (a), (b) Cross sectional view of the reconstructed 3D image.

On radiograph 67(a), the difference in neutron attenuation between the stainless steel and the air creates sufficient contrast to distinguish some internal features, such as through-holes. The false-colored cross-sectional view 67(b) of the reconstructed 3D image clearly shows internal stainless steel structure as yellow and air gaps (through and drilled holes) as green (shown by red arrows).

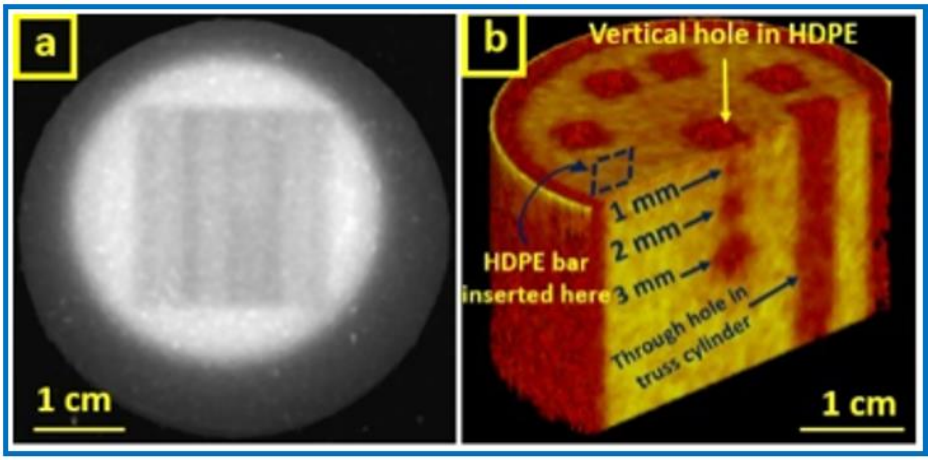

Figure 68: Radiograph of the truss cylinder (both inserts placed) (a), cross sectional view of the reconstructed 3D image (b).

Radiograph 68(a) shows neither the through-holes in the cylindrical HDPE insert nor the rectangular bar insert. However, the reconstructed 3D volume image 68(b) reveals the horizontal 1, 2, and 3 mm (indicated by blue arrows) and the vertical (shown by the yellow arrow) through-holes that are false colored as red, in the HDPE cylinder. The through-holes in the truss cylinder are also seen as red color. The rectangular bar inserted into the through-hole of the truss cylinder located at the spot indicated by the dashed parallelogram is not recognizable. One possible reason is the similarity in macroscopic cross-sections of stainless steel (0.241 cm^{-1}) and HDPE (0.303 cm^{-1}) at 2 MeV neutron energy.

Fast nCT data of two configurations of this phantom were also acquired using the new upgraded imaging station: Configuration 1 (Config-1) has both rectangular and cylindrical HDPE inserts on the sample center. Configuration 2 (Config-2) has the cylindrical feature on beam center while the rectangular feature is on one of the side through-holes. A 30

second exposure time per projection and EM gain of 30 were used when the reactor was operating at a power of 450 kW. 360 projections were obtained for each configuration. Projections were collected from 0 to 360 degree with 1-degree intervals, resulting in nCT data acquisition times of 180 minutes per configuration. A 3-pixel median filter was applied to all radiographs to remove salt-and-pepper noise, then post-processed radiographs were uploaded to a 3D reconstruction and visualization software code, Octopus, to create volume-rendered objects. Figures 69 and 70 show a photo, a sample radiograph, and reconstructions of the truss cylinder in Config-1 and Config-2, respectively.

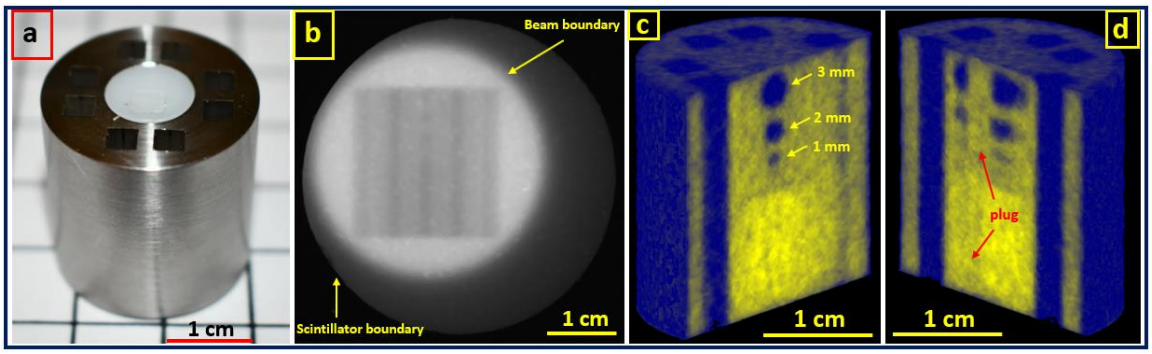

Figure 69: (a) A photograph, (b) a sample radiograph, and (c and d) cutaway side views of volume-rendered images of Config-1 of a SS truss cylinder phantom.

The sample radiograph shown in figure 69(b) provides information about the internal structure of the phantom as periodic vertical bright and dark regions. A simple radiograph cannot reveal the small voids inside the volume of the plastic insert nor give geometric

understanding of the features within the SS. Neither the cylindrical nor the rectangular HDPE insert can be seen in the radiograph. By contrast, in the volume-rendered image, figure 69(c), locations of the through holes in the volume can be seen, in addition to 1.0-, 2.0-, and 3.0-mm holes in cylindrical HDPE insert. However, the 0.5 mm hole is not resolved. The contrast between the lower and upper half of the SS structure helps define the cylindrical insert. In Figure 69(d), the rectangular plug can be distinguished as it splits through holes in the cylindrical insert. These features are resolved, even though poor contrast is created between the SS and the rectangular plug due to the plug's small thickness.

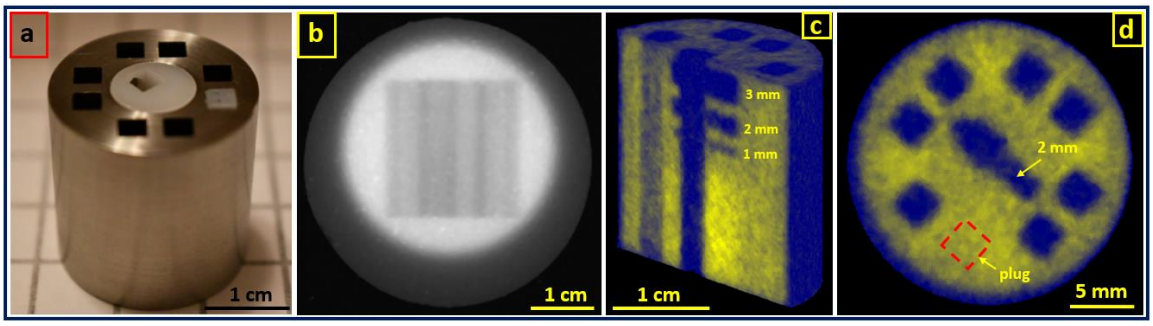

Figure 70: A photograph (a), a sample radiograph (b), cutaway side (c) and cutaway top-down (d) views of volume rendered images of Config-2 (cylindrical and rectangular plug HDPE inserts on the center and side, respectively) of the SS truss cylinder phantom.

Unlike Figure 69(b), a bright-dark periodicity is irregular in figure 70(b), suggesting an absorber, the rectangular plug, filling one of the through holes in SS structure. As before, the radiograph does not provide information about in which hole the plug is placed. No

information can be gathered about the cylindrical insert from this radiograph. However, a cutaway of the volume-rendered image, figure 70(c), reveals explicitly 1, 2, and 3 mm through holes in the cylindrical insert. The 0.5 mm hole is not resolved. Figure 70(d) is a top-down view that shows the 2 mm through-hole in the cylindrical insert and indicates in which hole the rectangular plug is inserted. The plug cannot clearly be distinguished as a different material from SS since the neutron attenuation is similar for HDPE (~ 8.8 %) and SS (~ 6.9 %) with thicknesses of 3 mm.

6.3.6 MAS (Grooved) Phantom

The "MAS" grooved phantom was attached to a plastic holder to provide a tilt of 21 degrees on the Ethafoam base. Two nCT data sets of the phantom were collected: one with the HDPE cylindrical insert placed inside and one without. The exposure time per projection was 60 seconds. An EM gain of 20 was chosen for the reactor power of 450 kW. Radiographs were collected at full 360-degree rotation with 1-degree intervals and the total nCT data acquisition time was 6 hours per configuration. Image processing, reconstruction, and visualization proceeded as previously described. A photo, a sample radiograph, and a volume rendered image of MAS with and without HDPE insert are shown in Figures 71 and 72, respectively.

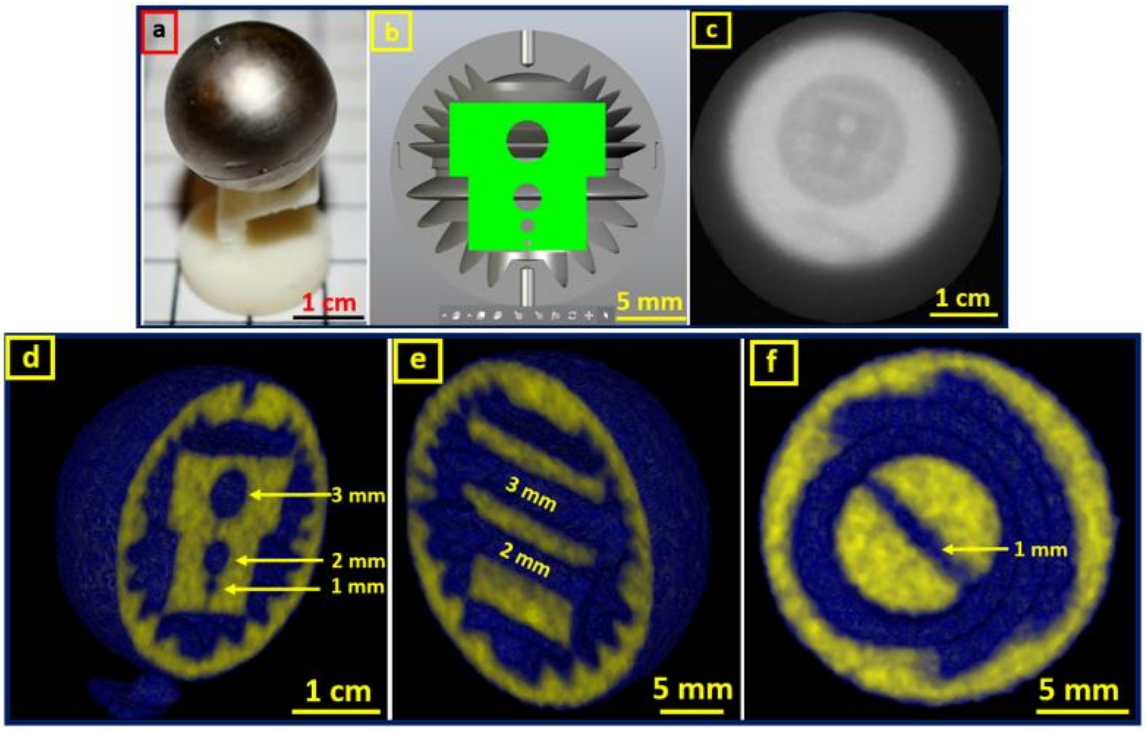

Figure 71: A photo of the MAS phantom assembled and connected to the plastic holder (a), a CAD drawing (b), a sample radiograph (c), cutaway side (d and e) and top-down (f) views of volume rendered images of MAS with HDPE insert.

A sample radiograph, figure 71(c), partially reveals the internal structure of MAS, showing the HDPE insert and its 2.0 and 3.0 mm through holes. However, neither the 1 mm nor the 0.5 mm holes are resolved. The internal grooved structure, the insert, and 1.0-, 2.0-, and 3.0-mm holes in the insert are evident in cutaway side views of volume-rendered images (figures 71(d) and 71(e)). The 0.5 mm hole in the insert is not clearly resolved, but the darker line below the 1 mm hole in figure 71(d) may be caused by the intermingling image of the air gap created by the hole, and the insert. Figure 71(f), a top-

down cutaway view of the volume-rendered image, provides a different perspective of the grooved structure as well as the 1.0 mm through-hole in the insert.

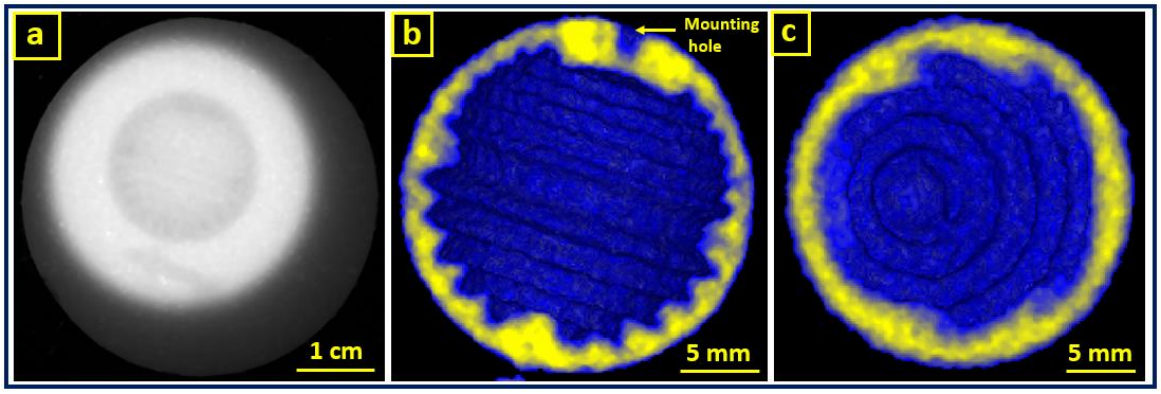

Figure 72: A sample radiograph (a), cutaway side (b) and top-down (c) views of the volume rendered images of MAS (without HDPE insert).

A sample radiograph, figure 72(a), yields better information on the groove structure compared to figure 71(c), as no insert is present. The radiograph also reveals that the hemisphere constituting the lower half of the phantom has more distinct grooves. Figure 72(b) provides the volume-rendered image in which the grooved structure on the internal surface creates a circular pattern. A top-down view of the volume-rendered image is given in figure 72(c), with same circular pattern. The phantom has two screw holes (1.4 mm) for mounting it to the holder. The hole on the top is resolved as shown in figure 72(b). Also in figure 72(b), two hemispheres create an internal canal-like feature where they meet, with a ~3 mm width.

6.3.7 Voxel Resolution in New Imaging System

The voxel resolution in reconstructed 3D images created from nCT data obtained using the new imaging station was also investigated. The pixel size of the EMCCD camera sensor is 16 μm, and a 50 mm fixed-focal-length lens, set to f/2.8, is connected to the EMCCD. The distance between the tip of the lens and the surface of the scintillator is ~ 32 cm. This configuration provides an effective pixel size of ~104 μm. The effective pixel size is predetermined by the sensor size, lens focal length, and the distance between the tip of the lens and the surface on which the camera is focused. During the reconstruction process, the third dimension, which determines the voxel size, is obtained as the slice thickness. The Octopus reconstruction software slices the image to provide the same slice thickness as the effective pixel size. Therefore, in this study, the voxel volume is ~104^3 μm^3.

6.3.8 Beam Hardening in MAS and SS Truss Cylinder Results

Figure 73 shows the 2 MeV neutron attenuation fraction in materials from which the imaging phantoms and the inserts are made, as a function of material thickness. While HDPE is the most effective in attenuating neutrons due to high hydrogen concentration, MAS (94 % Pb and 6 % Sb) is the least effective since it includes Pb. Pb has the highest atomic number among those elements in the imaging phantoms and the inserts. The difference in neutron attenuation in materials scales with increasing thickness. This explains why there is almost no contrast between the 0.3 cm thick HDPE plug and the SS truss structure, whereas there is contrast between the ~1 cm thick cylindrical HDPE and the SS truss structure.

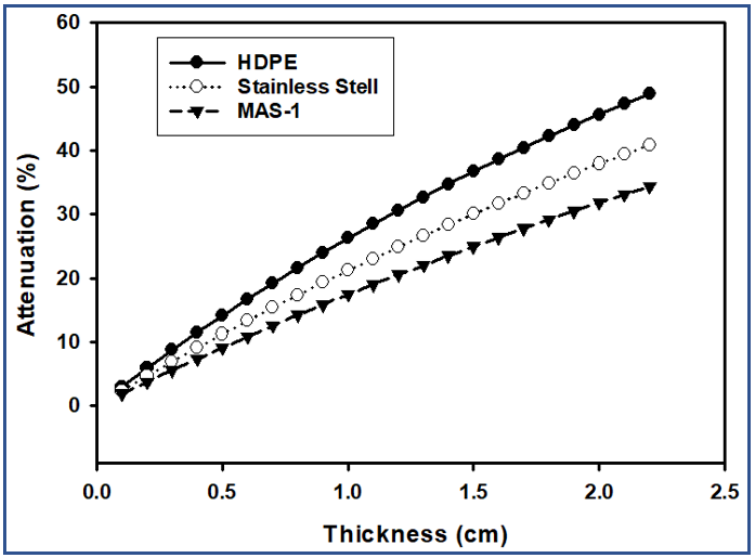

Figure 73: 2 MeV neutron attenuation in HDPE, SS, and MAS shell (94% Pb / 6% Sb) for various thicknesses.

Figure 74 provides the Macroscopic Cross Section (MAC)s of HDPE, SS, and MAS for neutron energies between 0.5 and 5 MeV, along with the MCNP-simulated fast neutron spectrum (0.1 - 5 MeV) from the OSURR. MACs converge as neutron energy increases, while the neutron spectrum features a rapid increase up to ~ 2 MeV and then a slow fall-off. Since MACs of the individual materials do not change dramatically with neutron energy, edge effects arising from beam hardening, as is typically seen with X-ray imaging, is negligible.

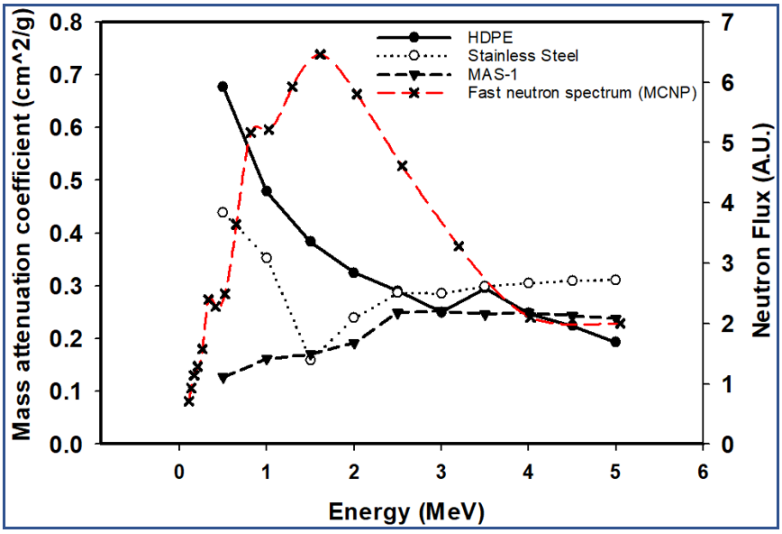

Figure 74: Mass attenuation coefficients of the imaging phantoms and HDPE insert for various neutron energies, and the MCNP-simulated fast neutron spectrum.

6.4 Conclusion

In this study, fast neutron computed tomography (nCT) was performed at OSURR's fast neutron beam facility using two different CCD-based neutron radiography acquisition systems. The EMCCD camera was not shielded against gamma-rays and neutrons in the first system, which caused highly saturated pixels on radiographs due to the direct energy deposition from those radiations onto the CCD chip, which eventually yielded radiographs with higher noise. In the second system, the EMCCD camera was shielded against the gamma-rays and neutrons using lead bricks and borated polyethylene, respectively. In both systems, image acquisition was performed automatically.

With using the old imaging system, radiographs of phantoms, which are ball phantom, OSU phantom, and Ti64 truss cylinder, made of various materials with different

thicknesses were collected and used to reconstruct 3D volumes. Total nCT data acquisition time varied from ~ 1.33 hours to 2.67 hours, depending on the complexity of the phantom and the reactor power. The total collected radiographic projections varied from 120 to 360. Reconstructed 3D images of phantoms revealed complex inner structures which could not be resolved in 2D radiography images. Cavities, concealed behind the high Z materials, with diameter of <2 mm could be visualized in the reconstructed 3D images.

With using the new imaging system, fast neutron computed tomography (nCT) was demonstrated with topographically complex phantoms which are MAS and SS truss cylinder phantoms. Additionally, nCT data of the OSU phantom's Config1 and Confi2, and Ti64 truss cylinder were also acquired for comparison purposes of the old and new imaging systems. 3D reconstructed images of the phantoms, which contain both high- and low-Z materials, were generated using 360 radiographs per 3D reconstructed image. The nCT acquisition time was as short as 3 hours. The phantoms' intricate internal structures, as well as features as small as 1 mm in diameter, were evident in in a low-Z material, HDPE, despite these structures being shielded by lead and stainless steel. The new imaging system yielded better nCT data which allowed to resolve even smaller features, which were not able to be distinguished with the old imaging system, in OSU and Ti64 truss cylinder phantoms, since the camera was shielded against gamma-rays and neutrons.

In both imaging systems, short acquisition times and high signal-to-noise ratios were enabled by an efficient automated imaging station, a thick high light yield plastic scintillator, as well as the high-flux fast neutron beam facility.

CONCLUSION AND FUTURE WORK

Growing demand for NDT around the world has necessitated efficient and reliable way of data acquisition systems. In digital neutron imaging systems, all components, neutron beam, neutron imager, and digital camera, need careful assessment, and depending on the energy of neutrons utilized in the applications, obtaining high-quality neutron radiographs can be challenging. While utilizing fast neutrons brings about some difficulties, they offer an opportunity to explore thicker and dense materials composed of high- and low-Z elements. Additionally, they allow samples to be released shortly after investigation as they cause fewer radionuclide creations. Accomplishments of this work can be summarized below

1- Polyvinyl Toluene (PVT) based plastic scintillators were characterized for fast neutron imaging. Various scintillators with different flours and dimensions were investigated in terms of relative light output and spatial resolution to determine the optimum combination of fluor and thickness fast neutron imaging applications.
2- The Ohio State Research Reactor (OSURR)' recently build a fast neutron beam facility was characterized. MCNP models of the beamline and beam stop were created and simulations were run to estimate the neutron energy spectrum, neutron & gamma-ray flux, and dose rate distributions. Cd ratio, gamma-ray content, and beam divergence of the beam were experimentally determined.
3- Fast neutron computed tomography (nCT) was performed using various additively manufactured phantoms in relatively short times employing a beam facility of a low-power research reactor. Some of the phantoms were made of layers of

elements, with low-z, such as HDPE plastic, and high-Z elements, such as Tungsten, while several phantoms had intricate truss structures. Minute features were revealed while being shielded behind thick, dense, and high-Z materials.

4- Factors affecting spatial resolution in a fast neutron imaging system were investigated. Ta foils and a W cube, with different thicknesses were utilized to determine the effect of the thickness of the imaging sample on the spatial resolution. It was also found that the neutron interaction kinematics in PVT is another important factor that should be taken into account.

BIBLIOGRAPHY

[1] S. J., "Non-Destructive post-irradiation examination results of the first modern fueled experiments in TREAT," *J. Nucl. Mater.*, vol. 541, p. 152442, 2020.

[2] S. B., "Detection systems for short-time stroboscopic neutron imaging and measurements on a rotating engine," *Nucl. Instrum. Methods Phys. Res. A: Accel. Spectrom. Detect. Assoc. Equip.*, vol. 542, pp. 1-3, 2005.

[3] K. D., "An on-line study of fuel cell behavior by thermal neutrons," *Nucl. Instrum. Methods Phys. Res. A: Accel. Spectrom. Detect. Assoc. Equip.*, vol. 542, pp. 52-60, 2005.

[4] W. J. M., "Neutron imaging reveals internal plant water dynamics," *Plant and Soil*, vol. 369, pp. 25-27, 2013.

[5] J. Banhart, "X-ray and neutron imaging – Complementary techniques for materials science and engineering," *International Journal of Materials Research*, 2010.

[6] K. H., "Neutron Radiography," *Research* , vol. 1, pp. 254-260, 1948.

[7] F. C., "The History of the First Neutron Radiographs in Berlin 1935-1944.," *Neutron Radiography.*

[8] T. J., "Neutron Radiography.," *British Journal of Applied Physics*, vol. 7, pp. 345-350, 1956.

[9] E. L. R. P. G. McFarland, "Multi-dimensional Neutroncomputed tomography Using Cooled Charge-coupled Devices.," *IEEE Trans. Nucl. Sci.*, vol. 38, pp. 612-621, 1991.

[10] R. Z. A. K. e. a. M. Cortesi, "Development of a cold-neutron imaging detector based on thick gaseous electron multiplier," *Review of Scientific Instruments* , vol. 84, 2013.

[11] N. E. M. C. R. H.-Z. Ilan Mor, "Development of a CCD based thermal neutron imaging detector for the Israeli Research Reactor IRR-1 at Soreq NRC," *Nuclear Inst. and Methods in Physics Research, A*, vol. 1012, p. 165632, 2021.

[12] F. K. E. S. I. E. M. Balasko, "A novel type epithermal neutron radiography detecting and imaging system," *Nuclear Instruments and Methods in Physics Research A*, vol. 424, pp. 263-269, 1999.

[13] A. C. Burkhard Schillinger, "Epithermal Neutron Radiography and Tomography on Large and Strongly Scattering Samples," *Materials Research Proceedings* , vol. 15, pp. 142-148, 2020.

[14] M. I. e. al, "High Spatial Resolution Fast-Neutron Imaging Detectors for Pulsed Fast-Neutron Transmission Spectroscopy," *JINST*, vol. 4, p. P05016, 2009.

[15] J. Chadwick, "Possible existence of a neutron.," *Electr. Eng.*, vol. 129, p. 312, 1932.

[16] J. S. &. S. W. M. Nico, "Fundamental Neutron Physics.," *Annu. Rev. Nucl. Part. Sci.*, vol. 55, pp. 27-69, 2005.

[17] P. J. T. B. N. &. N. D. B. Mohr, The 2018 CODATA Recommended Values of the Fundamental Physical Constants., National Institute of Standards and Technology, 2018.

[18] A. L. Nichols, . D. L. Aldama and V. M., Handbook of Nuclear Data for Safeguards: Database Extensions, Vienna: IAEA-INDC International Nuclear Data Committee , 2008.

[19] H. Berger, "Neutron Radiography: A State-of-the-Art Report," NTIAC, 1998.

[20] P. W. M.A. Lone, "Neutron yields from proton-induced spallation reactions in thick targets of lead," *Nuclear Instruments and Methods in Physics Research A* , vol. 362, pp. 499-505, 1995.

[21] S. N. Ahmed, Properties and sources of radiation in Physics and Engineering of Radiation Detection, 2015.

[22] D. G. Madland, "Theoretical descriptions of neutron emission in fission," in *International Atomic Energy Agency (IAEA) consultants meeting on nuclear emission in the fission process*, Vienna, 1990.

[23] É. M. Z. Máté Szieberth, "Determination of the Thermal Neutron Flux in the Core of the Reactor," BUDAPEST UNIVERSITY OF TECHNOLOGY AND ECONOMICS , Budapest, 2010.

[24] R. J. R. J. S. I. Prask HJ, "The NIST Cold Neutron Research Facility.," *J Res Natl Inst Stand Technol.*, vol. 98, pp. 1-13, 1993.

[25] J. C. Domanus, "Practical Neutron Radiography.," *Kluwer Academic Publishers*, 1992.

[26] D. C. Cutforth, "Neutron Source for Radiography and Gauiging," in *National Bureau of Standards and the American Society for Testing and Materials*, Gaithersburg, Maryland, 1975.

[27] G. M. MacGillivray, "Imaging with neutrons: the other penetrating radiation," in *SPIE, Penetrating Radiation Systems and Applications II*, 2000.

[28] D. L. A. M. V. A. L. Nichols, Handbook of Nuclear Data for Safeguards: Database Extensions, Vienna, Austria : IAEA, 2008.

[29] J. A. Grundl, "Fission-Neutron Spectra: Macroscopic and Integral Results," National Bureau of Standards, Washington, D. C., 2005.

[30] S. M. G. D. C. I. a. T. N. M. Carl R. Brune, "Neutron Source Capabilities at Ohio University," Ohio University, Athens, 2017.

[31] T. N. Massey and et al, "Study of the Be(p,n) and Be(d,n) Source Reactions," *Journal of Nuclear Science and Technology*, pp. 677-680, 2002.

[32] W. C. e. a. Chuirazzi, "Evaluation of polyvinyl toluene scintillators for fast neutron imaging," *Journal of Radioanalytical and Nuclear Chemistry*, vol. 318, pp. 543-551, 2018.

[33] S. F. Nowicki and et al, "The Los Alamos Neutron Science Center Spallation Neutron Sources," *Physics Procedia*, vol. 90, pp. 374-380, 2017.

[34] D. Abdessamad and et al, "Spallation Yield of Neutrons Produced in Tungsten and Bismuth Target Bombarded with 0.1 to 3 GeV Proton Beam," *Moscow University Physics Bulletin,* vol. 73, no. 6, pp. 612-617, 2018.

[35] E. J. Hall and H. H. Rossi, Californium-252 in Teaching and Research, Vienna: IAEA, 1974.

[36] . I. S. Anderson and et al, "Neutron Imaging and Applications," 2009.

[37] L. Green and et al, "The californium 252 fission neutron spectrum from 0.5 to 13 MeV.," *Nuclear science and engineering,* pp. 257-272, 2017.

[38] J. Csikai, Handbook of Fast Neutron Generators, Florida, USA: CRC Press, Inc., Boca Raton, 1987.

[39] B. Bayanov and et al, "Neutron producing target for accelerator based neutron capture therapy," *J. Phys.: Conf. Ser.,* vol. 41, p. 460, 2006.

[40] D. L. Chichester, "Production and Applications of Neutrons Using Particle Accelerators," Idaho National Laboratory , Idaho Falls, Idaho, 2009.

[41] I. ASTM, "Standard Test Method for Determining the L/D Ratio of Neutron Radiography Beams," ASTM standard-E 803-91, 2002.

[42] K. H. and R. H. Plaut, "Beam formation and characterization for neutron radiography," *Nondestructive testing and evaluation* , vol. 16, pp. 121-129, 2001.

[43] I. ASTM, "Standard Method For Determining Thermal Neutron Reaction And Fluence Rates By Radioactivation Techniques," ASTM standard E262-97.

[44] C. Kim and et al, "A Review of Inorganic Scintillation Crystals for Extreme Environments," *Crystals* , vol. 11, p. 669, 2021.

[45] N. Cherepy and et al, "Scintillators and Detectors for MeV X-ray and Neutron Imaging," in *SPIE Optical Engineering + Applications*, CA, 2020.

[46] K. Pritchard and et al, "6LiF:ZnS(Ag) Neutron Detector Performance Optimized Using Waveform Recordings and ROC Curves," *IEEE Trans Nucl Sci.,* 2021.

[47] D. Konishi and et al, "Response of GSO scintillator to thermal neutrons," *Nuclear Instruments and Methods in Physics Research A* , vol. 20 , p. 467—472, 1999.

[48] R. Zboray and et al, "Qualification and development of fast neutron imaging scintillator screens," *Nuclear Instruments and Methods in Physics Research Section A: Accelerators, Spectrometers, Detectors and Associated Equipment,* vol. 930, pp. 142-150, 2019.

[49] J. Radon, "On the Determination of Functions From Their Integral Values Along Certain Manifolds.," *IEEE Trans. Med. Imaging* , pp. 170-176, 1986.

[50] E. Lehman, "Non-invasive studies of objects from cultural heritage.," *Nuclear Instruments and Methods in Physics Research, Section A: Accelerators, Spectrometers, Detectors and Associated Equipment,* vol. 542, pp. 68-75, 2005.

[51] Neutron Methods for Archeology and Cultural Heritage, Springer, 2017.

[52] S. Robuschi and et al, "Corrosion of Steel in Concrete Seen through Neutron and X-Ray Tomography," *Neutron News,* 2021.

[53] P. Vontobel and et al, "Neutron tomography: Method and applications," *Physica B: Condensed Matter,* vol. 385, pp. 475-480, 2006.

[54] C. Stone, "6Li-doped silicate glass for thermal neutron shielding," *Nuclear Instruments and Methods in Physics Research A,* no. 349, pp. 515-520, 1994.

[55] IAEA, Database of Prompt Gamma Rays from Slow Neutron Capture for Elemental Analysis, Vienna: IAEA, 2007.

[56] T. Belgya, "High-resolution study of the 113Cd(n,γ) spectrum by statistical decay model with discrete levels and transitions," in *EPJ Web of Conferences*, 2017.

[57] "Andor," [Online]. Available: https://andor.oxinst.com/assets/uploads/products/andor/documents/andor-ixon-ultra-emccd-specifications.pdf. [Accessed 20 June 2022].

[58] Andor, [Online]. Available: https://andor.oxinst.com/learning/view/article/dynamic-range-emccds. [Accessed 15 June 2022].

[59] M. Z. J. B. J.F. Ziegler, SRIM-the stopping and range of ions in matter, Nucl. Instrum. Methods Phys. Res. B, 2010.

[60] "Revised Safety Analysis Report and Technical Specifications for The Ohio State University Research Reactor," U.S. Nuclear Regulatory Commission, Washington D.C., 1999.

[61] R. C. L. T. D. Lewandowski, "Noise evaluation of a digital neutron imaging device," *Nucl. Instruments Methods Phys. Res. Sect. A Accel. Spectrometers, Detect. Assoc. Equip. ,* vol. 674, pp. 46-50, 2012.

[62] N. T. T. N. M. K. M. K. J. K. M. M. H. likura, "Evaluations of the new LiF-scintillator and optional brightness enhancement films for neutron imaging," *Nuclear Instruments and Methods in Physics Research A,* vol. 651, pp. 100-104, 2011.

[63] Y. H. B. S. A. T. M. M. M. S. J. L. A. T. M. S. A.S Losko, "New perspective for neutron imaging through advanced event-mode data acquisition," Nature scientific reports, 2021.

[64] D. M. M. S. B. W. A. L. B. S. M. S. S. C. V. D. C. S. D. C. G. D. N. E. H. Lehmann, "Improvement in the spatial resolution for imaging with fast neutrons," *Nuclear Instruments and Methods in Physics Research A,* vol. 988, p. 164809, 2021.

[65] W. C. H. P. M. N. C. L. C. I. Oksuz, "Characterization of Polyvinyl Toluene (PVT) scintillators for fast neutron imaging," in *SPIE Hard X-ray, Gamma-Ray, and Neutron Detector Physics XX 10762*, 2018.

[66] W. Chuirazzi and e. al, "Evaluation of polyvinyl toluene scintillators for fast neutron imaging," *Journal of Radioanalytical and Nuclear Chemistry,* vol. 318, pp. 543-551, 2018.

[67] S. R. B. R. L. Cao, " The measurement of the presampled MTF of a high spatial resolution neutron imaging system," *Nuclear Instruments and Methods in Physics Research A,* vol. 582, pp. 621-628, 2007.

[68] K. Rossmann, "Measurement of the Modulation Transfer Function of Radiographic Systems Containing Fluorescent Screens," *Phys. Med. Biol.,* vol. 551, 1964.

[69] M. V. Z. M. B. A. K. J. H. P. K. N. J. C. L. R. C. I. Oksuz, "Characterization of a reactor-based fast neutron beam facility for fast neutron imaging," in *SPIE Hard X-Ray, Gamma-ray, and Neutron Detector Physics XXII 11494*, 2020.

[70] N. C. H. Q. P. V. G. Y. J. R. D. Sanner, "Phosphorescent heteroleptic iridium (III) cyclometallates: Improved syntheses of acetylacetonate complexes and quantum chemical studies of their excited state properties," *Polyhedron,* vol. 176, p. 114256, 2020.

[71] Z. M. S. S. H. D. S. P. K. S. O. I. O. M. B. L. R. C. S. P. R. D. S. G. S. B. H. G. G. J. H. R. S. J. M. C. M. P. T. N. J. Cherepy, "Scintillator and Detectors for MeV X-ray and Neutron Imaging," in *Proc. SPIE 11494, Hard X-Ray, Gamma-Ray, and Neutron Detector Physics XXII, 114940N*, 2021.

[72] C. H. M. M. O. M. J. Baggio, "Transient noise in a CCD camera sensor induced by neutron and gamma irradiation," in *6th European Conference on Radiation and Its Effects on Components and Systems*.

[73] F. B. A. Marbs, "Investigating the influence of ionizing radiation on standard CCD camera and a possible impact on photogrammetric measurements," *ISPRS Commission V Symposium 'Image Engineering and Vision Metrology',* vol. XXXVI, pp. 184-189.

[74] B. A, The essential guide to image processing, Elsevier Inc., 209.

Appendix A. MCNP input decks of Fast Neutron Beam Facility and Beam Stop Models

A.1 Input Deck of Beam Facility Model

```
The Ohio State University Research Reactor (OSURR)
c     Nuclear Reactor Laboratory (NRL)
c    Fast Neutron Beam Facility (FNBF)
c   Collimators and Beam shutter model
c       Beam is off position
c         Ibrahim Oksuz_2019
c ********************************************************
c ***************** Cell Cards ***************************
c ********************************************************
c
  101     9    -2.7      1   -2    4   -6                  imp:n=1 $Aluminum Tube
  121     9    -2.7     24  -23   34  -86                    imp:n=1
  122     6    -2.7     -1   11   91  -10                   imp:n=1 $metamic
  102     9    -2.7     -2    3   -4 #130                   imp:n=1 $Aluminum Cap
  130     8    -0.0012   3   -4  -11                       imp:n=1
  131     9    -2.7     10  -52   -1                      imp:n=1
  103     8    -0.0012  40  -56  102  -57                     imp:n=1 $air gap
  123     8    -0.0012 -59   40 -115  114                    imp:n=1 $Thin Window
  104     3    -3.35    22   -6    2  -14  15  -12  13        imp:n=1
  117     3    -3.35    34  -86   23  -14  15  -12  13         imp:n=1
  116     4    -1 3    -22  -12   13  -14  15    2           imp:n=1
  105     3    -3.35     7  -14    6  -34  -9   16           imp:n=1
  106     3    -3.35    -8   15    6  -34  -9   16           imp:n=1
  107     3    -3.35     9  -12    6  -34 -14   15           imp:n=1
  108     3    -3.35   -16   13    6  -34 -14   15           imp:n=1
  109     9    -2.7     -1   40   21  -62                   imp:n=1
  110     9    -2.7     -1   56  102  -57                    imp:n=1
  111     9    -2.7     -1   40   57   -6                   imp:n=1
  112     9    -2.7    -24   40   34  -35                    imp:n=1
c  115    9   -2.7      40  -24   36  -51                    imp:n=1
c
  400     1   -2.226    -1    4  -91   11                    imp:n=1 $Graphite
c
  120     2   -9.78    -53   52  -21                        imp:n=1  $Bismuth
  150     9   -2.7      -1   53   52  -21                   imp:n=1
c
  260     8   -0.0012    6  -34   -7    8  -9 16 #250 #500 #600 imp:n=1 $Air
```

```
c
 250    7  -11.84    -97    8   -7 #500 #600              imp:n=1
c
c ************ Metamic_Pb_Borated Poly ********************************
c ******************* set 1 ***********************************************
c
 201    9   -2.7     40    -1   62   -65                 imp:n=1
 202    5   -1.8     54   -55   65   -66                 imp:n=1
 203    9   -2.7     40   -54   65   -66                 imp:n=1
 204    9   -2.7     55    -1   65   -66                 imp:n=1
 205    9   -2.7     40    -1   66   -72                 imp:n=1
 206    6   -2.7     40    -1   72   -73                 imp:n=1
 207    7  -11.84    40    -1   73   -74                  imp:n=1
 208    7  -11.84    40    -1   74   -75                  imp:n=1
 209    6   -2.7     40    -1   75  -110                 imp:n=1
c ************************************************************************
c ******************* set 2 ***********************************************
c
 210    9   -2.7     40    -1  110   -76                 imp:n=1
 211    5   -1.8     54   -55   76   -77                 imp:n=1
 212    9   -2.7     40   -54   76   -77                 imp:n=1
 213    9   -2.7     55    -1   76   -77                 imp:n=1
 214    9   -2.7     40    -1   77   -78                 imp:n=1
 215    6   -2.7     40    -1   78   -79                 imp:n=1
 216    7  -11.84    40    -1   79   -92                  imp:n=1
 217    7  -11.84    40    -1   92   -93                  imp:n=1
 218    6   -2.7     40    -1   93   -94                 imp:n=1
c ************************************************************************
c ****************** set 3 ***********************************************
c
 219    9   -2.7     40    -1   94  -111                 imp:n=1
 220    5   -1.8     54   -55  111   -96                 imp:n=1
 221    9   -2.7     40   -54  111   -96                 imp:n=1
 222    9   -2.7     55    -1  111   -96                 imp:n=1
 223    9   -2.7     40    -1   96   -98                 imp:n=1
 224    6   -2.7     40    -1   98   -99                 imp:n=1
 225    7  -11.84    40    -1   99  -100                  imp:n=1
 226    7  -11.84    40    -1  100  -101                  imp:n=1
c ************************************************************************
c ****************** set 4 ***********************************************
c
 227    6   -2.7     40   -24   35   -37                 imp:n=1
 228    7  -11.84    40   -24   37   -38                  imp:n=1
 229    7  -11.84    40   -24   38   -39                  imp:n=1
 230    9   -2.7     40   -24   39  -112                 imp:n=1
 231    5   -1.8     54   -58  112   -41                 imp:n=1
```

```
 232    9  -2.7     40   -54  112   -41                imp:n=1
 233    9  -2.7     58   -24  112   -41                imp:n=1
 234    9  -2.7     40   -24   41   -45                imp:n=1
c ********************************************************************
c ***************** set 5 ********************************************
c
 235    6  -2.7     40   -24   45   -46                imp:n=1
 236    7 -11.84    40   -24   46  -113                 imp:n=1
 237    7 -11.84    40   -24  113   -36                imp:n=1
 238    8  -0.0012  40   -24   36  -114                 imp:n=1 $air gap
 239    9  -2.7    -24    59  114  -115                imp:n=1
 240    9  -2.7    -24    40  115   -86                imp:n=1
c ********************************************************************
c ***************** Inside aluminum tube *********************************
c
 313    8  -0.0012  21    -6  -40                     imp:n=1
 318    8  -0.0012  34   -86  -40                     imp:n=1
 314    8  -0.0012  40    -1  101  -102                 imp:n=1
 340    8  -0.0012   4   -10  -11                     imp:n=1
c
 500   10  -0.95    95    -5  -97                    imp:n=1
 600    8  -0.0012 -95   -97                         imp:n=1
c
 900    8  -0.0012 -999 (-3 :86 :12 :-13 :14 :-15 )        imp:n=1
 901    0          999                                 imp:n=0
c  ********************** Blank Line *********************************

c ********************************************************************
c  ********************* Surface Cards ********************************
c ********************************************************************
c
   1       cx    6.985          $I.D.
   2       cx    7.62           $O.D. 7.5184 after milling
   3       px    0
   4       px    0.125
   5       c/y  125.8  0  7.62          $poly inside beam shutter
   6       px   106.7999
   7       pz    19
   8       pz   -19
   9       py    19.1
  10       px    13.46
  11       cx     1.905
  12       py    80
  13       py   -80
  14       pz    80
  15       pz   -80
```

```
 16      py   -19.1
 21      px    23.77875
 22      px    36.83
 23      cx     8.89
 24      cx     8.5725
 34      px   157.3175
 35      px   157.635
 36      px   194.1475
 37      px   158.27
 38      px   160.81
 39      px   163.35
 40      cx     1.5875
 41      px   188.4325
 45      px   188.75
 46      px   189.385
 52      px    13.61875
 53      cx     6.35
 54      cx     2.54
 55      cx     6.6675
 56      cx     5.842
 57      px   106.4825
 58      cx     7.9375
 59      cx     7.4295
 62      px    23.9375
 65      px    24.255
 66      px    43.94
 72      px    44.2575
 73      px    44.8925
 74      px    47.4325
 75      px    49.9725
 76      px    50.925
 77      px    70.61
 78      px    70.9275
 79      px    71.5625
 86      px   197.64
 91      px    12.825
 92      px    74.1025
 93      px    76.6425
 94      px    77.2775
 95     c/y   125.8  0  1.905          $aparture in beam shutter poly
 96      px    97.28
 97     c/z   125.8  0 19
 98      px    97.5975
 99      px    98.2325
100      px   100.7725
101      px   103.3125
```

```
 102       px   103.63
 110       px    50.6075
 111       px    77.595
 112       px   163.6675
 113       px   191.925
 114       px   194.465
 115       px   197.3225
 999       so   500
c ********************** Blank Line
****************************************

c ************************************************************
c  ************** Data Cards ****************************
c ************************************************************
c
mode    n                              $neutrons
mphys  on
phys:n
nps  5e7
print  -160
c prdmp  2j 1
prdmp -1 J -1
c print
c ************************************************************
c ********************** Source Card ***********************
c **************Degenerate cylindrical source  ************
c
SDEF POS= -0.001 0 0  AXS=1 0 0 EXT=0 RAD=d1 PAR=1 ERG=d2 VEC=1 0 0
DIR=1
SI1   0  7.62
SP1 -21  1
c ************* Near  core spectrum ************************
SI2    H 0.0 1.00E-09 1.26E-09 1.58E-09 1.98E-09 2.49E-09 3.13E-09
          3.93E-09 4.93E-09 6.20E-09 7.78E-09 9.77E-09 1.23E-08
          1.54E-08 1.94E-08 2.43E-08 3.06E-08 3.84E-08 4.82E-08
          6.06E-08 7.61E-08 9.55E-08 1.20E-07 1.51E-07 1.89E-07
          2.38E-07 2.99E-07 3.75E-07 4.71E-07 5.92E-07 7.44E-07
          9.34E-07 1.17E-06 1.47E-06 1.85E-06 2.32E-06 2.92E-06
          3.67E-06 4.61E-06 5.79E-06 7.27E-06 9.13E-06 1.15E-05
          1.44E-05 1.81E-05 2.27E-05 2.85E-05 3.58E-05 4.50E-05
          5.66E-05 7.10E-05 8.92E-05 1.12E-04 1.41E-04 1.77E-04
          2.22E-04 2.79E-04 3.50E-04 4.40E-04 5.53E-04 6.94E-04
          8.72E-04 1.10E-03 1.38E-03 1.73E-03 2.17E-03 2.73E-03
          3.42E-03 4.30E-03 5.40E-03 6.79E-03 8.53E-03 1.07E-02
          1.35E-02 1.69E-02 2.12E-02 2.67E-02 3.35E-02 4.21E-02
          5.28E-02 6.63E-02 8.33E-02 1.05E-01 1.31E-01 1.65E-01
```

```
          2.07E-01 2.61E-01 3.27E-01 4.11E-01 5.16E-01 6.48E-01
          8.15E-01 1.02E+00 1.29E+00 1.61E+00 2.03E+00 2.55E+00
          3.20E+00 4.02E+00 5.05E+00 6.34E+00 7.96E+00 1.00E+01
c
SP2    D 0.0 2.13E-04 1.00E-04 3.93E-04 6.44E-04 4.13E-04 8.03E-04
          1.42E-03 2.55E-03 2.93E-03 5.68E-03 7.96E-03 1.29E-02
          1.76E-02 2.32E-02 3.23E-02 4.09E-02 4.76E-02 5.57E-02
          5.94E-02 5.88E-02 5.03E-02 3.48E-02 2.20E-02 1.44E-02
          1.02E-02 6.18E-03 5.02E-03 5.67E-03 4.23E-03 5.18E-03
          4.80E-03 4.36E-03 5.88E-03 3.28E-03 3.78E-03 3.96E-03
          4.00E-03 3.62E-03 3.53E-03 2.85E-03 4.23E-03 3.35E-03
          3.70E-03 4.14E-03 4.96E-03 4.11E-03 4.10E-03 4.23E-03
          4.78E-03 3.94E-03 3.72E-03 3.76E-03 4.65E-03 3.79E-03
          4.73E-03 4.55E-03 4.19E-03 4.38E-03 4.11E-03 4.76E-03
          3.55E-03 4.11E-03 3.98E-03 4.32E-03 5.10E-03 5.28E-03
          5.07E-03 4.68E-03 4.80E-03 4.56E-03 5.25E-03 6.16E-03
          5.75E-03 5.56E-03 5.65E-03 6.33E-03 7.35E-03 6.37E-03
          6.51E-03 7.56E-03 7.68E-03 9.07E-03 9.40E-03 9.01E-03
          8.62E-03 1.11E-02 1.05E-02 1.30E-02 1.17E-02 1.41E-02
          1.59E-02 1.58E-02 1.67E-02 1.75E-02 1.94E-02 1.66E-02
          1.17E-02 8.18E-03 5.48E-03 4.13E-03 2.18E-03 5.96E-04
c
c ******************************************************************
c ******************************** Tally Card ***********************
c
c ******************************** Mesh Tally ***********************
tmesh
rmesh11:n flux
c cora11  217      218
c corb11  -80  79i  80
c corc11  -80  79i  80
cora11  0  205i  205
corb11 -80 160i   80
corc11 -0.5       0.5
endmd
c mplot freq 10000000 plot ex 160 px 217.5 la 0 1 tal11.1 color on la 0 0
c      contour 1e-8 1 16 log
c mplot freq 2000000 plot ex 220 pz 0 la 0 1 tal11.1 color on la 0 0
c      contour 1e-8 1 16 log
c ************************************************************
c
c ************************** Material Card
************************************
c
c ******** Bismuth ****************************
m2    83209.70c         1
```

```
c ********************************************
c ***** Borated Aluminum **********************
m6    5010.70c         0.064
      13027.70c        0.936
c ********************************************
c ********* Water ******************************
m4    1001.70c        -0.11190
      8016.70c        -0.88810
c ********************************************
c ********** HDPE ******************************
m10   1001.70c         0.6667
      6000.70c         0.3333
c ********************************************
c ***** Barytes Concrete : 3.35 g/cc ***   *****
m3    1001.70c         0.11
      8016.70c         0.60
      20000.62c        0.04    $Ca
      16032.70c        0.10     $S
      19000.62c        0.04    $K
      56138.70c        0.11    $Ba
c ********************************************
c ********* Lead *******************************
m7    82207.70c          1
c ********************************************
c ******** Air ********************************
m8    7014.70c         -0.755268
      8016.70c         -0.231781
      18000.42c        -0.012827
      6000.70c         -0.000124
c ********************************************
c ****** SWX-277z-5 castable shielding 1.68 g/cc***
m5    1001.70c         -0.0473
      5010.70c         -0.0100
      5011.70c         -0.0400
      17035.70c        -0.1436
      17037.70c        -0.4309
      20000.62c        -0.3282
c ********************************************
c ******** Aluminum ****************************
m9    13027.70c        1
c ********************************************
c ******** Grphite *****************************
m1    6000.70c         1
c ********************************************
c ************************************************************
c  Other
```

A.2 Input Deck of Beam Stop Model

```
The Ohio State University Research Reactor (OSURR)
c     Nuclear Reactor Laboratory (NRL)
c    Fast Neutron Beam Facility (FNBF)
c            Beam stop
c         Ibrahim Oksuz_2019
c 75x75x75cm_5cm side lead_ 5%borated poly.with metamic.
c  Borated Polyethylene hd 5%
c ************************************************************
c                 Cell Cards
c ************************************************************
c ******************Recess (air) ***************************
001  3  -0.0012 -400 100 -101                  imp:n,p=1
002  3  -0.0012 -400 101 -102                  imp:n,p=1
003  3  -0.0012 -400 102 -135                  imp:n,p=1
004  3  -0.0012 -400 135 -103                  imp:n,p=1
c
c ************* Borated Polyethylene Slabs ***************
101  6 -2.7   100 -150 201 -202 300 -301 #001      imp:n,p=1 $ 1
131  4 -11.35 150 -101 201 -202 300 -301 #001      imp:n,p=1 $ 1
102  5 -2.7   101 -102 201 -202 300 -301 #002      imp:n,p=1 $ 2
132  2 -1.07  102 -135 201 -202 300 -301 #003      imp:n,p=1 $ 2
103  2 -1.07  135 -103 201 -202 300 -301 #004      imp:n,p=1 $ 3
104  2 -1.07  103 -104 201 -202 300 -301          imp:n,p=1 $ 4
105  2 -1.07  104 -105 201 -202 300 -301          imp:n,p=1 $ 5
106  2 -1.07  105 -107 201 -202 300 -301          imp:n,p=1 $ 6
107  2 -1.07  107 -108 201 -202 300 -301          imp:n,p=1 $ 7
108  2 -1.07  108 -109 201 -202 300 -301          imp:n,p=1 $ 8
109  2 -1.07  109 -110 201 -202 300 -301          imp:n,p=1 $ 9
110  2 -1.07  110 -111 201 -202 300 -301          imp:n,p=1 $ 10
111  2 -1.07  111 -112 201 -202 300 -301          imp:n,p=1 $ 11
112  2 -1.07  112 -113 201 -202 300 -301          imp:n,p=1 $ 12
113  2 -1.07  113 -114 201 -202 300 -301          imp:n,p=1 $ 13
114  2 -1.07  114 -115 201 -202 300 -301          imp:n,p=1 $ 14
115  2 -1.07  115 -116 201 -202 300 -301          imp:n,p=1 $ 15
116  2 -1.07  116 -117 201 -202 300 -301          imp:n,p=1 $ 1
117  2 -1.07  117 -118 201 -202 300 -301          imp:n,p=1 $ 2
118  2 -1.07  118 -125 201 -202 300 -301          imp:n,p=1 $ 3
119  2 -1.07  125 -126 201 -202 300 -301          imp:n,p=1 $ 3
120  2 -1.07  126 -127 201 -202 300 -301           imp:n,p=1
121  2 -1.07  127 -128 201 -202 300 -301           imp:n,p=1
122  2 -1.07  128 -129 201 -202 300 -301           imp:n,p=1
123  2 -1.07  129 -130 201 -202 300 -301           imp:n,p=1
124  2 -1.07  130 -131 201 -202 300 -301           imp:n,p=1
125  2 -1.07  131 -132 201 -202 300 -301           imp:n,p=1
```

```
126  2 -1.07  132 -120 201 -202 300 -301            imp:n,p=1
c ***********************************************************
c ***************** Lead Slabs ****************************
200  2 -1.07   201 -202  300 -301 120 -121 #305 #302 imp:n,p=1
201  2 -1.07   201 -202  300 -301 121 -122 #306      imp:n,p=1
202  2 -1.07   201 -202  300 -301 122 -600 #307      imp:n,p=1
203  4 -11.35  200 -203  503 -302 123 -124          imp:n,p=1
204  6 -2.7    200 -203  503 -302 124 -134          imp:n,p=1
206  4 -11.35  505 -500  504 -304 100 -123          imp:n,p=1
216  6 -2.7   -505  200  503 -302 100 -123          imp:n,p=1
207  4 -11.35  501 -204  504 -304 100 -123          imp:n,p=1
217  6 -2.7    204 -203  503 -302 100 -123          imp:n,p=1
208  4 -11.35  500 -501 -304  502 100 -123          imp:n,p=1
218  6 -2.7    505 -204  304 -302 100 -123          imp:n,p=1
209  4 -11.35  504 -303 -123  100 500 -501          imp:n,p=1
219  6 -2.7   -504  503 -123  100 505 -204          imp:n,p=1
210  4 -11.35 -700                                 imp:n,p=1
c ***********************************************************
c ************ Metamic (Borated Al) ************************
300 5 -2.7  500 -201 303 -502 100 -123              imp:n,p=1
301 5 -2.7 -501  202 303 -502 100 -123              imp:n,p=1
302 5 -2.7 -119 120 -133                          imp:n,p=1
303 5 -2.7  301 -502 100 -123 201 -202              imp:n,p=1
310 5 -2.7  600 -123 201 -202 300 -301 #307         imp:n,p=1
304 5 -2.7  201 -202 303 -300 100 -123              imp:n,p=1
c ***********************************************************
 305 4 -11.35 -133 119 -121 imp:n,p=1
 306 4 -11.35 -133 121 -122 imp:n,p=1
 307 4 -11.35 -133 122 -123 imp:n,p=1
c ************  Null space ********************************
600  0 -900 (-100:134:-503:302:-200:203)   #210     imp:n,p=1 $
601  0         900                          imp:n,p=0 $
c Blank Line

c ***********************************************************
c                    Surface Cards
c ***********************************************************
c
100 px 0.00
150 px 1.27
101 px 2.54
102 px 3.175
135 px 5.08
103 px 7.62
104 px 10.16
105 px 12.7
```

```
107 px 15.24
108 px 17.78
109 px 20.32
110 px 22.86
111 px 25.4
112 px 27.94
113 px 30.48
114 px 33.02
115 px 35.56
116 px 38.1
117 px 40.65
118 px 43.18
119 px 66.675
120 px 66.04
121 px 68.58
122 px 71.12
123 px 73.66
124 px 76.2
125 px 45.72
126 px 48.26
127 px 50.8
128 px 53.34
129 px 55.88
130 px 58.42
131 px 60.96
132 px 63.5
133 cx 10.16
134 px 78.74
c
200 py -38.01
201 py -34.925
202 py  34.925
203 py  38.09
204 py  36.82   $ Al and Pb
c
300 pz -34.925
301 pz  34.925
302 pz  38.09
303 pz -35.55
304 pz  36.82   $ Al and Pb
c
400 cx  5.08
c
500 py -35.55
501 py  35.55
502 pz  35.55
```

```
503 pz -38.01
504 pz -36.82 $ Al and Pb
505 py -36.82 $ Al and Pb
c
700 rcc 78.75 0 0 10 0 0 10.16
c
600 px 73.025
c Outside world boundary
900 so   200
c Blank Line

c ***********************************************************
c                        Data Cards
c ***********************************************************
c
mode N              $neutrons
nps 1E8
phys:N              $default p physics
c
c ***********************************************************
c                    Source
c ***********************************************************
c Disc Source x MeV photon
SDEF   POS=0 0 0 AXS=1 0 0 EXT=1 RAD=d1 PAR=1 ERG=3
     VEC=1 0 0 DIR=1
SI1   0 2          $ radial sampling range: 0 to Rmax (=1.6 cm)
SP1 -21 1          $ radial sampling weighting: r^1 for disk
c
c ***********************************************************
c                         Materials
c ***********************************************************
c
c   Borated Aluminum
m5   5010          0.064
    13027         0.936
c Aluminum 2.7 g/cc***
m6  13027    1
c
c   Borated Polyethylene hd 5%   1.07 g/cc***
m2   5010         -0.010
    5011         -0.040
    6012         -0.833
    1001         -0.117
c
c  ******** Air **********   0.001225 g/cm3 *** Mass fraction
m3   7014          -0.755268
```

```
     8016          -0.231781
     18000          -0.012827
     6012          -0.000124
c  Lead
m4  82207           1.00
c
c
c ***********************************************************
c                              Tally
c ***********************************************************
c
c Surface cross tallies on side and back
f21:n 122 $backside
f31:n 203 $side
f41:n 100 $backscatter
c Mesh Tally
tmesh
rmesh11:n flux
cora11 -61 129i 100
corb11 -60 99i 60
corc11 -0.5 0.5
endmd
c mplot freq 10000000 plot ex 65 pz 0 la 0 1 tal11.1 color on la 0 0
c      contour 5 95 10 & line color
c
c ***********************************************************
c  Other
c ***********************************************************
c
print -160
prdmp 2j 1
```